

AN ABSTRACT OF THE THESIS OF

Donald Francis Elger for the degree of Doctor of Philosophy in
Mechanical Engineering presented on April 28, 1986

Title: An Experimental and Analytical Study of the Internal Fluid
Dynamics of an Ink-Jet Printhead

Redacted for Privacy

Abstract approved: _____

✓ |

Ronald L. Adams

An experimental and analytical study of the internal fluid dynamics of a drop-on-demand (DOD) ink-jet printhead has been conducted. The central idea of the project was to develop a large scale model with air as the working fluid in order to obtain fluid dynamics data relevant to the interior of a printhead. The analytical results are: (i) a model of an ink-jet printhead, (ii) a method for scaling up a printhead for experimental study with air as the working fluid, and (iii) a physically based interpretation of an ink-jet printhead as a piston driven Helmholtz resonator. An application of the model for the design of a DOD printhead was conducted. The analysis also illuminated the need for experimental information to characterize the orifice or nozzle area of the printhead.

The experimental task was focused on obtaining parameters to characterize the fluid dynamics of monochromatic sinusoidal zero mean flow through two orifices in series, the "Stemme" nozzle. In particular the dimensionless dependent variables $R/\rho\sqrt{\omega\nu}$, $\delta/0.85d_1$, $v_0/\sqrt{\omega\nu}$, and v_2/v_0 were correlated with the dimensionless independent variables; d_2/d_1 , t_p/d_1 and $P'/\rho\omega\nu$ for the following ranges of parameters: $0.23 \leq d_2/d_1 \leq 0.94$, $0.4 \leq t_p/d_1 \leq 2.6$, and $660 \leq P'/\rho\omega\nu \leq 4120$; where ω is frequency, R is the resistance term which will characterize the nozzle damping, δ is the added mass term to characterize the nozzle mass attribute, d_1 and d_2 are the first and second orifice diameters, v_0 and v_2 are the velocity magnitudes out the first and

second orifices, P' is the acoustic pressure across the two orifices, and t_p is the orifice spacing. Data was also obtained to show that for certain combinations of parameters, the double orifice nozzle will rectify an oscillating velocity. For the rectified case, a sinusoidal fluid velocity incident on the first orifice will produce a rectified sine wave fluid velocity out the second orifice.

The experimental study required a considerable methods development effort. The most significant result of this was a method for the calibration of a hot wire anemometer probe for the measurement of a zero mean sinusoidal reversing flow.

An Experimental and Analytical Study of the Internal Fluid
Dynamics of an Ink-Jet Printhead

by

Donald Francis Elger

A THESIS

Submitted to

Oregon State University

in partial fulfillment of
the requirements for the
degree of

DOCTOR OF PHILOSOPHY

Completed April 28, 1986

Commencement June 1986

APPROVED:

Redacted for Privacy

Professor of Mechanical Engineering in charge of major

Redacted for Privacy

Head of Mechanical Engineering Department

Redacted for Privacy

Dean of Graduate School

Date thesis is presented April 28, 1986

Typed by Laurie Campbell and Peggy Offutt

ACKNOWLEDGEMENTS

The research presented in this thesis was certainly influenced by the support, thoughts, and philosophies of many people I have worked with and learned from over the course of my education. I would especially like to acknowledge the support of my friend and wife, Linda, and of my parents. Many of the technical approaches and methods were developed during conversations with Siggí Brynjólfsson. His help with the many difficult problems I faced was very appreciated.

I would like to thank my major professor, Ron Adams, for providing me with his research insights and for his time and efforts on this project.

Tektronix, Inc., provided the funding for the research and equipment.

TABLE OF CONTENTS

	<u>Page</u>
1.0 INTRODUCTION.....	1
1.1 The Ink-Jet Printhead.....	1
1.2 Scope of the Analysis.....	4
1.3 Thesis Organization.....	4
2.0 THE INK-JET PRINthead AND THE HELMHOLTZ RESONATOR: AN ANALYTICAL STUDY.....	6
2.1 Introduction.....	6
2.2 Scope.....	11
2.3 Dimensional Analysis.....	11
2.4 Analysis.....	15
2.4.1 The horn region.....	15
2.4.2 Piezoelectric driver.....	19
2.4.3 Fluid/structure interactions.....	19
2.4.4 The orifice region.....	24
2.4.5 Viscous effects in the horn region.....	28
2.5 A System Model.....	30
2.5.1 The piston driven Helmholtz resonator.....	30
2.5.2 Application to ink-jet printheads.....	35
2.5.3 A simple analogy.....	37
2.5.4 Design of an ink-jet printhead.....	37
2.6 Conclusions.....	47
3.0 DYNAMIC CALIBRATION OF A CONSTANT TEMPERATURE HOT WIRE ANEMOMETER IN A ZERO MEAN OSCILLATING FLOW.....	49
3.1 Introduction.....	49
3.2 Analysis and Design of the Test Section.....	51
3.2.1 Design for incompressible flow.....	51
3.2.2 Orifice design.....	55
3.2.3 An experimental check.....	59
3.3 Experimental Apparatus and Procedures.....	62
3.4 Experimental Data.....	64
3.5 Discussion.....	70
3.6 Conclusions.....	72
4.0 A STUDY OF OSCILLATING FLUID FLOW THROUGH TWO ORIFICES IN SERIES.....	74
4.1 Introduction.....	74
4.2 Dimensional Analysis.....	81
4.3 Problem Formulation.....	81
4.4 Experiment Apparatus.....	84

	<u>Page</u>
4.5 Experimental Methods.....	89
4.5.1 Calibration.....	89
4.5.2 Impedance measurement.....	89
4.5.3 Use of the hot wire anemometer.....	91
4.6 Experimental Results and Discussion.....	98
4.7 Conclusions.....	106
5.0 SUMMARY AND CONCLUSIONS.....	108
BIBLIOGRAPHY.....	112
APPENDIX.....	116
A. Flow Visualization Study.....	117

LIST OF FIGURES

<u>Figure</u>		<u>Page</u>
1.1	Printhead and drum arrangement.....	2
1.2	(a) Cross section view of an ink-jet printhead, (b) cross section view of the simplified ink-jet printhead..	3
1.3	Input voltage signal to the printhead: (a) for a single drop, (b) for three drops.....	3a
2.1	A simplified cross sectional view of the DOD ink-jet printhead.....	7
2.2	Input voltage signal to produce (a) one ink drop and (b) three ink drops.....	8
2.3	The geometry for analyzing a two dimensional velocity boundary condition in a closed rigid wall tube.....	17
2.4	A lumped plate model subjected to a monochromatic pressure field for transmission coefficient calculation	21
2.5	Geometry for orifice impedance definition.....	25
2.6	Orifice impedance, resistance, and reactance as a function of the orifice velocity magnitude, v_0	27
2.7	Axial velocity profiles in a long tube as a function of shear wave number, S	31
2.8	A piston driven Helmholtz resonator subjected to mono- chromatic input.....	32
2.9	Geometry for drop development.....	36
2.10	Mechanical analogy of an ink-jet printhead.....	38
2.11	The design fluid volumetric displacement, $y(t)$, out the orifice.....	41
2.12	Example performance curves for parametric study cases...	45
2.13	Performance curves for the final design.....	46
3.1	(a) Velocity field to be measured, $v(t)/ v(t) = \sin(\omega t)$ (b) corresponding hot wire anemometer bridge voltage for three values of velocity amplitude.....	50
3.2	Test section.....	52

<u>Figure</u>		<u>Page</u>
3.3	Typical design curves of assess compressibility effects	54
3.4	Orifice geometry.....	57
3.5	Magnitude and argument of the compressibility factor, γ , as a function of shear wave number, S_o	60
3.6	Axial velocity profiles as a function of radius for four values of shear wave number, S_o	61
3.7	Typical waveforms at 45 hz ($S_o = 16.7$); these curves correspond to known orifice velocities, $v_c =$ (a) 0.29 m/s, (b) 0.63 m/s, (c) 2.24 m/s, and (d) 4.57 m/s.....	65
3.8	Maximum bridge voltage as a function of v_c	67
3.9	Minimum bridge voltage as a function of v_c	68
3.10	Phase lag of bridge voltage behind flow velocity as a function of v_c	69
3.11	Theoretical and measured radial velocity profiles across orifice.....	71
4.1	Oscillating flow through two orifices in series.....	75
4.2	A simplified ink-jet printhead.....	76
4.3	Input voltage signal to produce (a) one ink drop and (b) three ink drops.....	77
4.4	Geometry for orifice impedance definition.....	79
4.5	Double orifice goemetry showing important variables.....	82
4.6	Simplified cross sectional view of test section.....	85
4.7	(a) Double orifice assembly in cross section and (b) piston/driver assembly in cross section.....	86
4.8	Typical oscilloscope curves of $P'(t)$, $s(t)$, and $U(t)$ for the test section with a single orifice.....	92
4.9	Comparison of measured orifice parameters, R and δ , with the data compiled by Panton and Goldman [28].....	93
4.10	Experimental uncertainty for the data presented in Fig. 4.9.....	94

<u>Figure</u>		<u>Page</u>
4.11	Comparison of orifice velocity, $v_o(t)$, as measured by a hot wire anemometer and a standing wave method (a) $ v_o $ and (b) phase lag of $v_o(t)$ behind $P'(t)$	97
4.12	Typical oscilloscope waveforms for $s(t)$, $P'(t)$, $P'_2(t)$, and $U(t)$ for the test section with a double orifice geometry: (a) run D4, (b) run D2, and (c) run D3.....	100
4.13	Correlation equations for (a) $R/\rho\sqrt{\omega v}$, (b) d_2/d_1 , (c) $v_o/\sqrt{\omega v}$, and (d) v_2/v_o	103
4.14	Comparison of the measured data with the predictions of the correlation equations for (a) $v_o/\sqrt{\omega v}$ and (b) v_2/v_o ..	105
A.1	Flow visualization geometry.....	118
A.2	Sketch of typical streamlines during fluid outflow portion of cycle.....	118
A.3	Typical streamline photographs.....	119

LIST OF TABLES

<u>Table</u>		<u>Page</u>
2.1	Significant variables.....	12
2.2	Dimensionless groups.....	13
2.3	Mechanical, electrical, and acoustic analogies.....	39
4.1	Dimensionless groups.....	83
4.2	Experimental data.....	99
4.3	Regression coefficients.....	102

NOMENCLATURE

CHAPTER 2

A	= horn area
A_o	= orifice area
c	= equilibrium wave speed in fluid
c_s	= structure compression wave speed
d_o	= orifice diameter
D	= horn diameter
e	= horn wall thickness
E	= Young's modulus
i	= $\sqrt{-1}$
J_n	= Bessel function of first kind and order n
k	= wave number = ω/c
k_c	= thermal conductivity
k_h	= stiffness due to fluid in horn
k_s	= stiffness due to surface tension
L	= horn length
P	= equilibrium pressure
P'	= $ P'(x,t) $
$P(x,t)$	= complex instantaneous pressure
$P'(x,t)$	= $P(x,t) - P =$ acoustic pressure
r	= radial distance
r_d	= ink drop radius
R	= resistance
R	= horn radius
R_s	= resistance modified for surface tension effects
s	= $ s(t) $
$s(t)$	= complex piston position
S	= shear wave number = $\frac{D}{2} \sqrt{\frac{\omega}{\nu}}$
S_o	= shear wave number = $\frac{d_o}{2} \sqrt{\frac{\omega}{\nu}}$

t_o	= orifice thickness
t_p	= orifice plate thickness
$v_o(t)$	= complex instantaneous fluid velocity in orifice
v_o	= $ v_o(t) $
V	= $ V(x,t) $
$V(x,t)$	= fluid velocity in horn chamber
x	= longitudinal distance
\vec{x}	= position vector
$x(t)$	= piston volumetric displacement
X	= reactance
$y(t)$	= orifice fluid volumetric displacement
z	= fluid characteristic impedance = $\rho c/A$
z_o	= orifice impedance
α	= transmission coefficient
β	= fluid bulk modulus of compressibility
γ	= compressibility factor
δ	= length correction to account for added mass
δ_s	= δ modified to account for surface tension effects
ζ	= damping factor
μ	= fluid viscosity
ν	= fluid kinematic viscosity
ν_s	= Poisson's ratio
ρ	= fluid equilibrium density
$\rho(x,t)$	= fluid instantaneous density
$\rho'(x,t)$	= $\rho(x,t) - \rho$
ρ_s	= structure density
ϕ	= velocity potential
τ	= surface tension
ω	= frequency (rad/s)
ω_c	= cutoff frequency
ω_h	= Helmholtz natural frequency
ω_n	= natural frequency of the horn chamber for $kLz_o/Z \gg 1$
ω_o	= natural frequency for a printhead modeled as a single degree of freedom system; including surface tension
ω_{pc}	= coincidence frequency

NOMENCLATURE

CHAPTER 3

A	= tube area
A_o	= orifice area
c	= equilibrium wave speed in air
d_o	= orifice diameter
D	= horn diameter
i	= $\sqrt{-1}$
J_n	= Bessel function of first kind and order n
k	= wave number = ω/c
L	= tube length
P	= equilibrium pressure
P'	= $ P'(x,t) $
$P(x,t)$	= complex instantaneous pressure
$P'(x,t)$	= $P(x,t) - P$ = acoustic pressure
r	= radial distance
r_o	= orifice radius
s	= $ s(t) $
$s(t)$	= complex piston position
$\dot{s}(t)$	= complex piston velocity
S	= shear wave number = $\frac{D}{2} \sqrt{\frac{\omega}{\nu}}$
S_o	= shear wave number = $\frac{d_o}{2} \sqrt{\frac{\omega}{\nu}}$
t	= time
t_o	= orifice thickness
$U(t)$	= bridge voltage
v_c	= $ v_o(r=0, x=d_o/2, t) $ = velocity magnitude at the center of the orifice
v_o	= $ v_o(t) $
$v_o(r,x,t)$	= complex instantaneous fluid velocity in the orifice
$v_o(t)$	= radially averaged value of $v_o(r,x,t)$
V	= $ V(x,t) $

$V(x,t)$	= complex instantaneous fluid velocity in cylinder
x	= longitudinal distance
z_0	= orifice impedance \equiv complex ratio of monochromatic acoustic pressure across orifice to volume velocity through orifice
Z	= fluid characteristic impedance = $\rho c/A$
α	= compressibility factor
β	= fluid bulk modulus of compressibility
γ	= v_c/v_0
Γ	= reflection coefficient
Γ'	= propagation constant
ϵ	= compressibility error
μ	= viscosity
ν	= kinematic viscosity
ρ	= equilibrium density
ρ'	= $ \rho(x,t) $
$\rho(x,t)$	= instantaneous density
$\rho'(x,t)$	= $\rho(x,t) - \rho$
ϕ	= velocity potential
ω	= frequency (rad/s)
ω_c	= tube cutoff frequency

NOMENCLATURE

CHAPTER 4

A	= test section cross sectional area
A_0	= orifice area
c	= equilibrium wave speed in fluid
d_1	= orifice 1 diameter
d_2	= orifice 2 diameter
i	= $\sqrt{-1}$
k	= wave number = ω/c
L	= tube length
P	= equilibrium pressure
P'	= $ P'(x,t) $
P'_2	= $ P'_2(x,t) $
$P(x,t)$	= complex instantaneous pressure
$P'(x,t)$	= $P(x,t) - P$ = acoustic pressure in horn chamber
$P'_2(x,t)$	= acoustic pressure in the plate gap region
R	= resistance or real part of $z_0 A_0$
s	= $ s(t) $
$s(t)$	= complex piston position
$\dot{s}(t)$	= complex piston velocity
S	= shear wave number = $\frac{D}{2} \sqrt{\frac{\omega}{\nu}}$
t_p	= orifice plate spacing
t_1	= orifice 1 thickness
t_2	= orifice 2 thickness
U(t)	= bridge voltage from hot wire anemometer system
$v_0(r,x,t)$	= complex instantaneous fluid velocity in the orifice
$v_0(t)$	= radially averaged value of $v_0(r,x,t)$
v_0	= $ v_0(t) $ = orifice velocity magnitude
x	= longitudinal distance
X	= reactance or imaginary part of $z_0 A_0$
z_0	= orifice impedance
ν	= kinematic viscosity

ρ = equilibrium density

ω = frequency (rad/s)

AN EXPERIMENTAL AND ANALYTICAL STUDY OF THE INTERNAL FLUID
DYNAMICS OF AN INK-JET PRINthead

CHAPTER 1

INTRODUCTION

The rapid growth of computers for home, business, and industrial applications has led to a need for improved computer interfaced printers. One of the new technologies, the ink-jet printer, is the subject of this thesis. This printer creates images on paper by emitting tiny drops of ink to form letters, graphics, and pictures. The ink-jet printer has advantages of quiet operation, multicolor printing capability and better print resolution as compared to the conventional impact printer.

1.1 The Ink-Jet Printhead

An ink-jet printer of the type studied forms color images by generating a pattern of magenta, cyan, yellow, and black ink dots. Positioning is controlled by moving four printheads horizontally on rails and moving the paper vertically on a print drum, Fig. 1.1. A printhead will emit a single drop of ink in response to a voltage signal, allowing digital pattern control.

There are a number of types of ink-jet printheads in commercial use. The type under study for this work is shown in cross section on Fig. 1.2a. The fluid is a water based ink and the structure is steel. An input voltage, Fig. 1.3a, applied to the PZT biomorph,¹ leads to the ejection of a single drop of ink out the plate 2 orifice. After ejection, the drop is accelerated by air blown through the air line and passes through the plate 3 orifice and onto the paper. Ink refills from a reservoir which feeds ink between plates 1 and 2. A typical voltage signal to create three drops is shown in

¹The PZT biomorph is a piezoelectric crystal bonded to a steel plate. A voltage applied across the piezoelectric crystal produces a deformation of the plate.

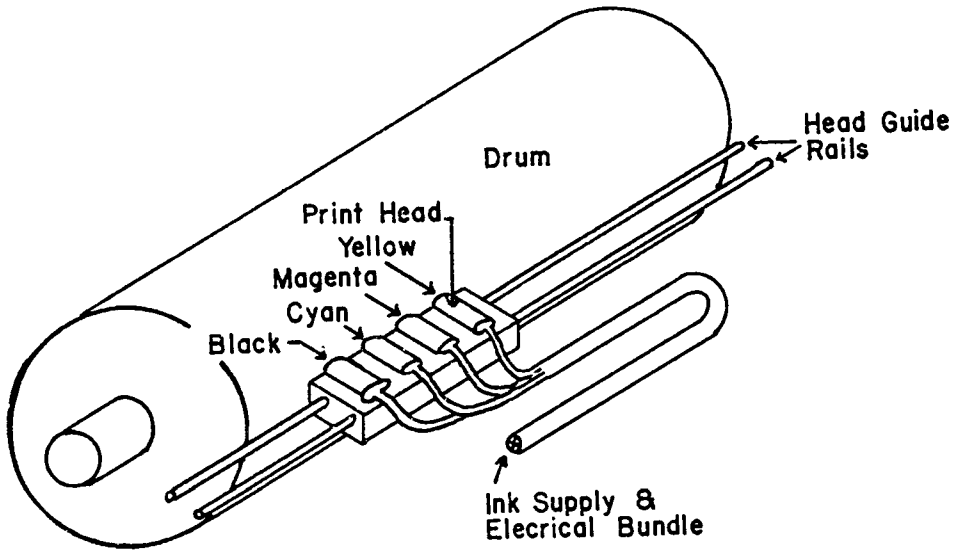
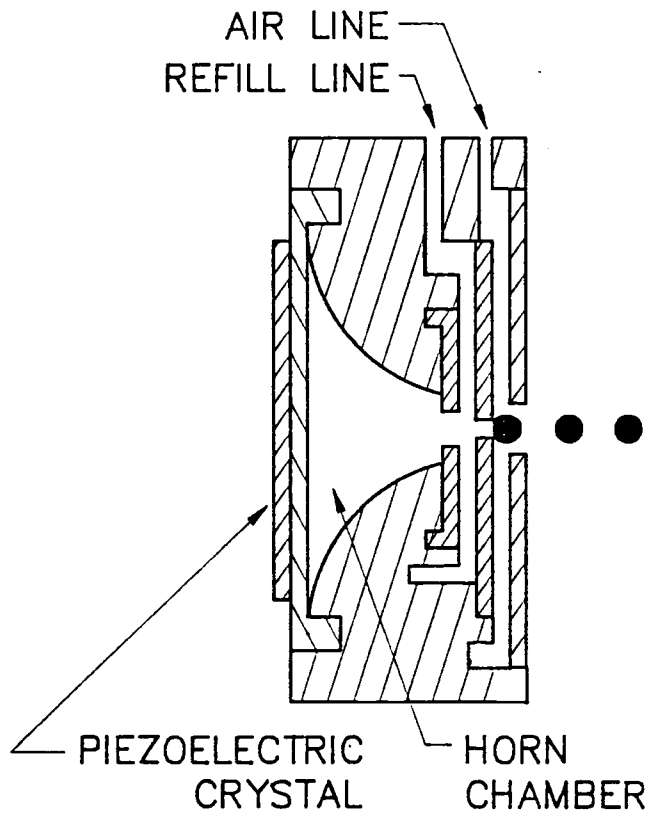
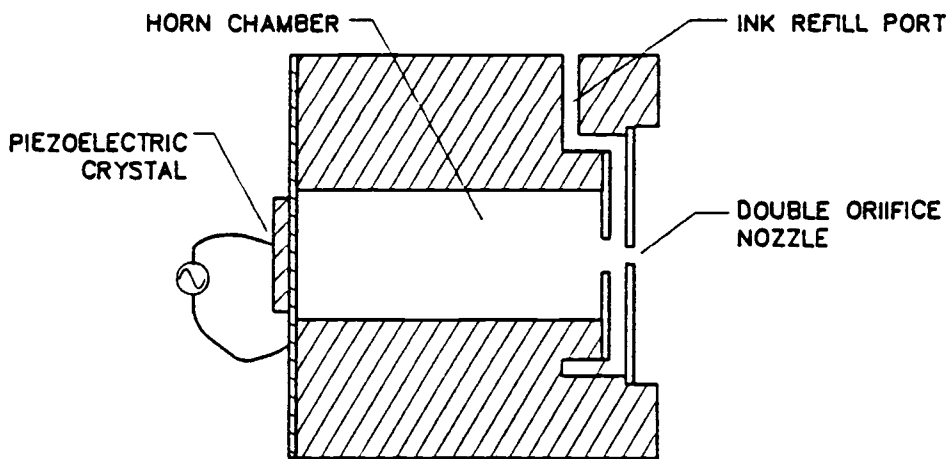


Fig. 1.1. Print head and drum arrangement



(a)



(b)

Fig. 1.2. (a) Cross section view of an ink-jet printhead,
 (b) cross section view of the simplified printhead

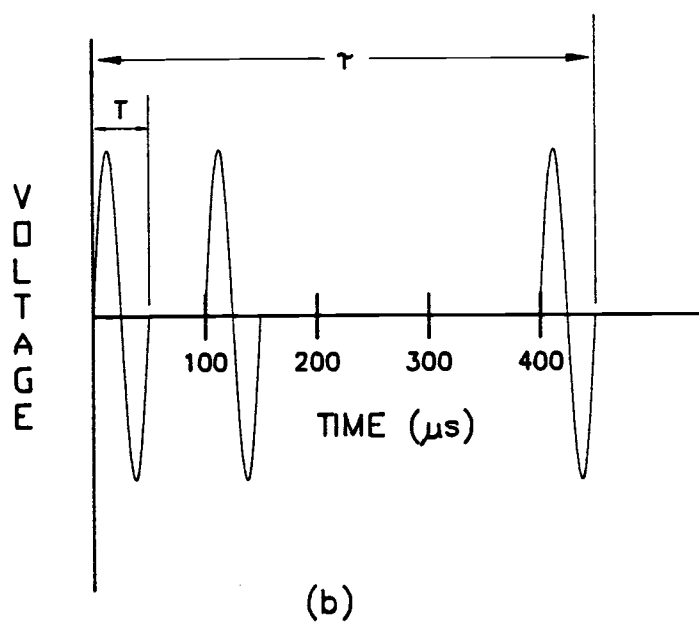
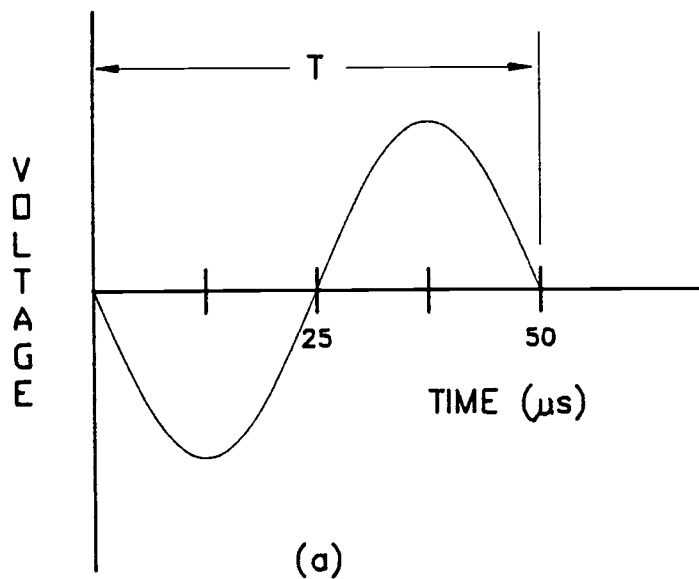


Fig. 1.3. Input voltage signal to the printhead:
(a) for a single drop
(b) for three drops

Fig. 1.3b. Because of the on/off nature of printing, the time between pulses is not uniform.

The distinguishing features of the Fig. 1.2a printhead as compared to other designs are the double orifice nozzle formed by plates 1 and 2 and the use of air to accelerate the drop after it is ejected. The double orifice nozzle was first proposed by Stemme and Larsson [35,46]. The air assist was developed by Matshusta Corporation [47].

1.2 Scope of the Analysis

The printhead interior fluid dynamics were chosen as the area for study. PZT biomorph dynamics and drop development were not considered. The primary effort was experimental and directed towards gaining understanding of the fluid mechanics in the double orifice region. Printhead geometry was simplified by considering a cylindrical cross section, Fig. 1.2b.

The problem to be solved was as follows. Determine the relationships among the variables influencing the internal fluid mechanics within the printhead and the double orifice region. Provide information such that a designer could use it for simplifying and/or improving the existing design.

A comment: The problem statement above is open ended and very general. A great deal of effort was directed towards establishing more specific objectives. The formulation of these objectives is presented in the body of the thesis.

1.3 Thesis Organization

The thesis, written in "manuscript format," is comprised of three stand alone journal articles, Chapters 2-4, respectively, and a conclusions section, Chapter 5. The topics addressed in the thesis body are as follows.

The objectives of Chapter 2 are: (i) to present an analytical model of an ink-jet printhead and show how this model may be used by a designer, (ii) to develop a method of scaling up a printhead for

experimental study with air as the working fluid, and (iii) to establish what is important to be measured experimentally.

Another way to describe the objective of Chapter 2 is as follows. The experimental model consisted of a 20-in. long aluminum cylinder with a monochromatically vibrating piston at one end and two orifices in series at the other. The usual comment was: "What does this have to do with an ink-jet printer?" In function and appearance, the test section has little relationship to an ink-jet printhead. However, when the underlying form, i.e. the physics of the fluid flow, are studied; the relationships are very strong. Chapter 2 was written to establish these relationships.

No existing method was found to measure velocities of the oscillating reversing fluid in the double orifice region. Chapter 3 describes a method of calibrating a hot wire anemometer for making such measurements. The key to the success of this venture was the design of a test section to produce a sinusoidal reversing flow of known magnitude. The physics used for this design are exactly the same as those presented in Chapter 2.

One of the Chapter 2 conclusions was that the most important experimental objective is to characterize the nozzle area fluid dynamics. In Chapter 4 an experimental study with an objective of characterizing the fluid dynamics of oscillating zero mean flow through two orifices in series is presented. The topics addressed include dimensional analysis, development of measurement methods and establishment of what parameters are important to measure. Fluid velocity and pressure data for oscillating flow through a double orifice geometry is presented in a format useful to the designer of an ink-jet printhead.

Chapter 2

THE INK-JET PRINthead AND THE HELMHOLTZ RESONATOR:

AN ANALYTICAL STUDY

2.1 Introduction

This chapter presents an analysis of the fluid mechanics in the interior of an ink-jet printhead. The analysis is directed towards understanding the internal fluid mechanics of a simplified drop-on-demand (DOD) ink-jet printhead. In particular, ink refill was not included and drop development was treated in a simplified fashion. Analysis is presented to show that the simplified ink-jet printhead can be viewed as a piston driven Helmholtz resonator.

The results of this analysis are: (i) a model of an ink-jet printhead and of a piston driven Helmholtz resonator, (ii) a physically based interpretation of an ink-jet printhead as a piston driven Helmholtz resonator, (iii) an example design of a printhead, and (iv) a method for scaling up a printhead for experimental study with air as the working fluid.

This analysis was originally performed in support of an experimental study (Chapters 3 and 4). The idea behind the experimental work was to develop a large scale printhead model with air as the working fluid so that data on the internal fluid mechanics could be obtained. In performing the analysis, it was evident that the results could also be quite useful to the ink-jet printhead designer. Thus, this chapter was written with parallel objectives of providing information useful for the designer and defining what is significant for an experimental study.

An ink-jet printhead with a generic configuration was considered, Fig. 2.1. The ink, which is located in the horn region is water based and the structure is steel. A voltage signal, Fig. 2.2a, applied to the piezoelectric crystal leads to a crystal deformation in the x direction. This causes ink to flow down the horn chamber and out the orifice where a single drop of ink is ejected. The horn refill port, not shown on Fig. 2.1, supplies makeup ink during the

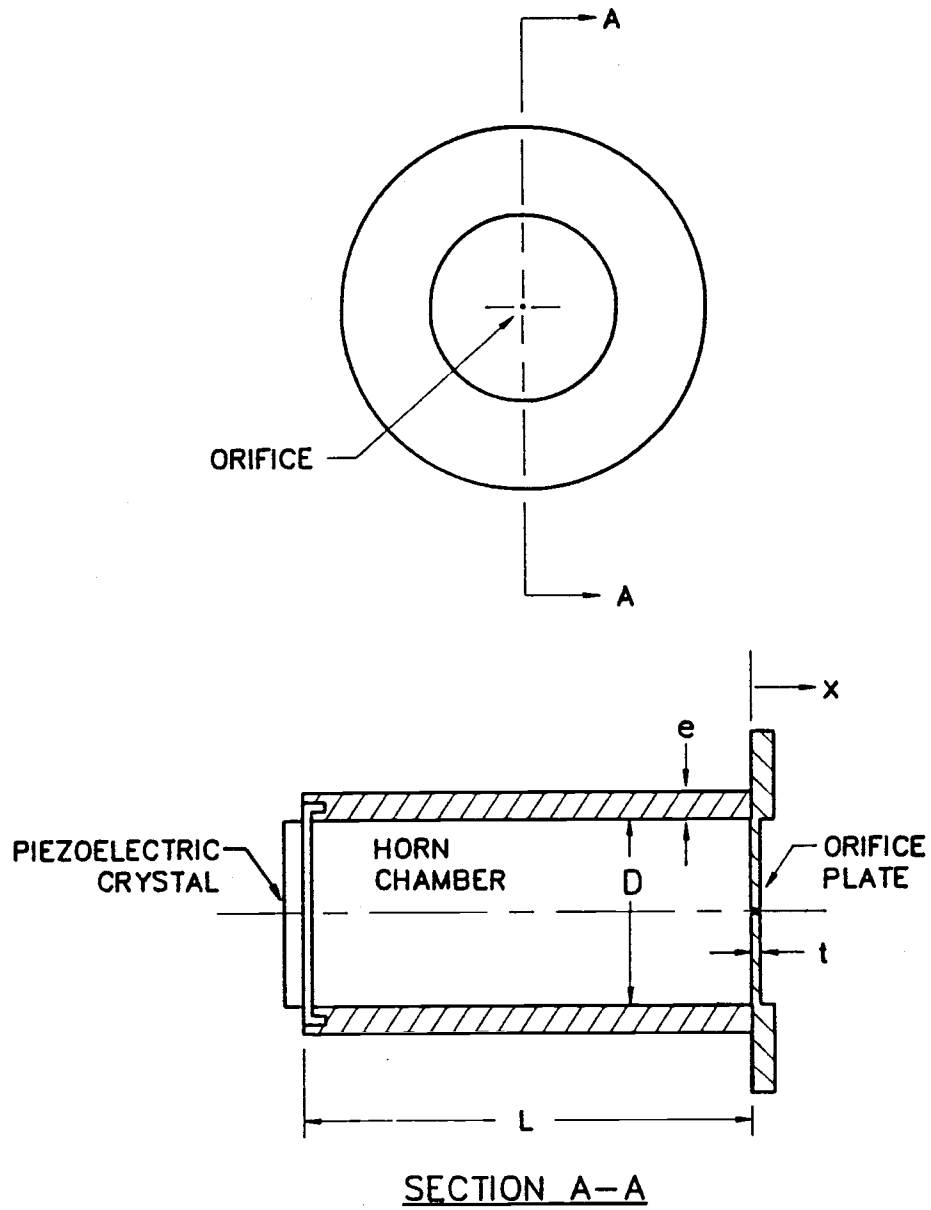


Fig. 2.1. A simplified cross sectional view of the DOD ink-jet printhead

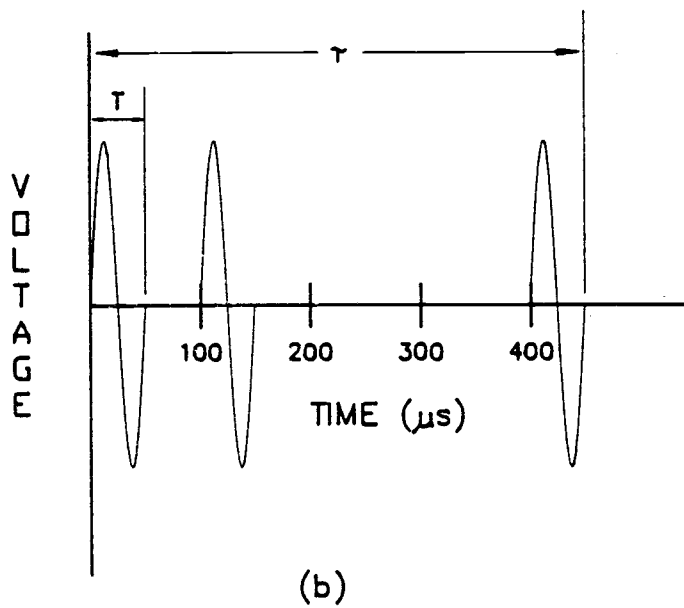
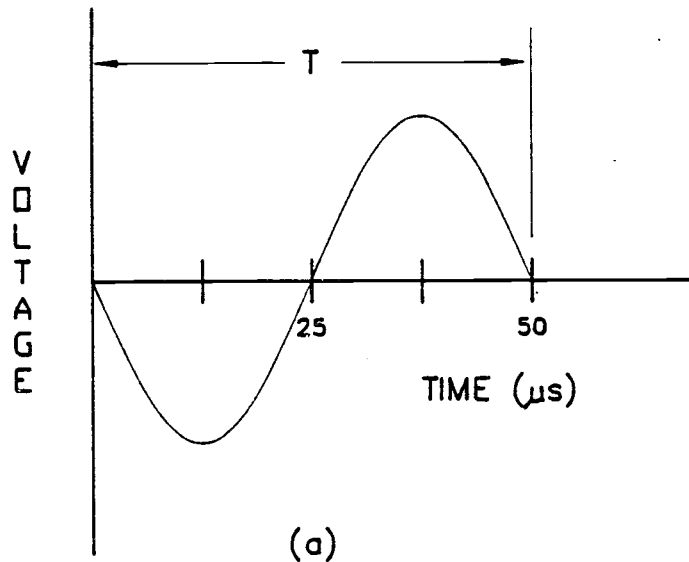


Fig. 2.2. Input voltage signal to produce
(a) one ink drop
(b) three ink drops

negative portion of the voltage signal. An image is formed by generating a pattern of the tiny ink drops. A typical voltage signal to create three drops is shown in Fig. 2.2b. Because of the on/off nature of printing, the time between pulses is not uniform.

The Helmholtz resonator, a simple acoustics model, consists of a chamber connected to the ambient by a neck or orifice. This device will resonate or absorb sound at a characteristic frequency, the Helmholtz resonance, which is determined by its geometry. At resonance, the fluid in the chamber behaves much like a spring and oscillates the fluid in the neck which provides the mass. The vibrating fluid in the neck can be conceptualized as a small vibrating piston of equivalent mass and it is this motion which radiates sound. The sounds produced by the main resonance of a guitar or by blowing over a pop bottle are familiar examples of Helmholtz resonators.

The ink-jet printhead, Fig. 2.1, is seen to be a piston driven Helmholtz resonator. Thus, models of these two devices should have a great deal in common. The derivation of this model begins with a review of ink-jet printhead modeling efforts followed by a dimensional analysis of a piston driven Helmholtz resonator. Next, the resonator is analyzed in a general way to determine what aspects of the physics are important for ink-jet printhead modeling. Finally, a model and its application to the design of an ink-jet printhead are presented.

Ink-jet printing technologies have been reviewed by Heinzl and Hertz [1]. The literature related to the internal fluid mechanics of the drop-on-demand, DOD, printhead will be reviewed here.

Larsson and Lundqvist's [2] analytical and experimental study of a DOD printhead includes drop development, internal fluid dynamics and piezoelectric transducer modeling. The internal fluid flow equations were developed using potential flow theory with an assumed spherical flow field around the orifice. Analog simulation was used to predict system behavior. Experimentally measured drop characteristics are presented.

To model internal flow, Beasley [3] used an incompressible and lumped analysis to arrive at effective inertia and viscous lengths

for different regions in the printhead. Similarly, Kyser et al. [4] used an lumped incompressible model to develop effective masses, springs and damping coefficients.

Bogy and Talke [5] performed an analysis of the internal fluid dynamics and present experimentally measured drop parameter data and a photographic record of the drop formation process. The analysis used the piezoelectric crystal displacement as an initial condition for d'Alembert's solution to the wave equation. They concluded that the use of linear acoustic theory produced good agreement with their measured data.

Mizuno et al. [6] used four transfer functions to describe printhead fluid flow. Compressibility effects were included and the transfer function coefficients were determined experimentally.

Roy et al. [7] developed a coupled 1D numerical model of the piezoelectric driver and horn chamber. The model treated the horn chamber as a closed cavity (no orifice). Plate modeling was performed with an assumed modes method and fluid modeling was performed using the 1D method of characteristics. Model results showed good agreement with measured pressures in a piezoelectric driven closed cavity.

Drop development studies related to DOD ink-jet technologies have been presented by Adams and Roy [8] and Fromm [9].

Several conclusions may be drawn about the literature reviewed. The fluid mechanics have been primarily treated using a variety of a "lumped parameter" approaches, with fluid compressibility sometimes included. With the exception of Roy et al. [7], the existing data are measurements and photographs of drops ejected from a printhead. A nondimensional grouping of the variables important to the internal fluid mechanics has not been presented. An analysis of fluid structure interactions has not been presented. Finally, there are a number of existing studies related to printhead physics which have not been referenced.

2.2 Scope

Consider a device that is identical in size and operation to a DOD ink-jet printhead, with the exception that the fluid in the horn region is the same as that in the ambient region. Define this as the "printhead" under study. By studying this device a great deal can be learned about the physics of an actual printhead. Then in §2.5 the surface tension boundary condition present during drop formation will be incorporated into the analysis.

2.3 Dimensional Analysis

The approach used in conducting the dimensional analysis was to break the independent variables into two groups: (1) those influencing the fluid flow in the horn chamber, and (2) those influencing the fluid flow out the orifice. The reason for this is because analyzing the horn chamber fluid dynamics is a separate problem from analyzing the orifice fluid dynamics. Using this formulation, the coupling between the fluid dynamics of the two regions was contained in one dimensionless group.

Significant variables with typical values are presented in Table 2.1. It was assumed that the fluid thermal transport properties are not important. The characteristic frequency, ω , is defined as $2\pi/T$; with T given on Fig. 2.2. Structural properties are included because fluid/structure interactions were considered.

The dimensionless groups formed from the Table 2.1 variables are presented in Table 2.2. The particular groupings are arranged to emphasize physical significance. These groupings were derived by first using standard dimensional analysis to form "initial groups." Next, scaling of the governing physical equations was used as guidance in combining the initial groups into the groups appearing in Table 2.2.

There are three groups governing the fluid dynamics in the horn region. The value of the frequency ratio, kL , reflects the influence of compressibility. As kL changes from small to large, the fluid will behave as incompressible (zero degrees of freedom), lumped compressible (one degree of freedom) and distributed compressible (partial differential equation). The value of kL/π , which is analogous

Table 2.1. Significant variables.

Symbol	Name	Nominal Value
<u>HORN REGION</u>		
β	Fluid bulk modulus	207×10^7 Pa
ρ	Fluid density	998 kg/m^3
μ	Fluid viscosity	$1.0 \times 10^{-3} \text{ kg/(m}\cdot\text{s)}$
P'	Peak horn pressure	$\approx 1.0 \times 10^5$ Pa
L	Horn length	$4750 \text{ }\mu\text{m}$
D	Horn diameter	$2000 \text{ }\mu\text{m}$
ρ_s	Structure density	7700 kg/m^3
E	Young's modulus	194×10^9 Pa
ν_s	Poisson's ratio	0.27
t_p	Orifice plate thickness	$100 \text{ }\mu\text{m}$
e	Horn wall thickness	$1000 \text{ }\mu\text{m}$
ω	Frequency	$1.26 \times 10^5 \text{ rad/s}$
<u>ORIFICE REGION</u>		
v_o	Orifice velocity	$\approx 8 \text{ m/s}$
ρ	Fluid density	998 kg/m^3
μ	Fluid viscosity	$1.0 \times 10^{-3} \text{ kg/(m}\cdot\text{s)}$
d_o	Orifice diameter	$45 \text{ }\mu\text{m}$
t_o	Orifice thickness	$22 \text{ }\mu\text{m}$

Table 2.2. Dimensionless groups.

Symbol	Name	Nominal Value
<u>HORN REGION (fluid mechanics)</u>		
kL	Frequency ratio	0.41
P'/β	Pressure coefficient	5×10^{-5}
$S = \frac{D}{2} \sqrt{\frac{\omega}{\nu}}$	Shear wave number	355
L/D	Aspect ratio	2.4
<u>HORN REGION (fluid/structure interactions)</u>		
$(\rho c)_s / \rho c$	Characteristic impedance ratio	27
ω / ω_{pc}	Coincidence frequency ratio	0.062
$\beta D / Ee$	---	0.02
ν_s	Poisson's ratio	0.27
t_p / d_o	---	0.05
e / D	---	0.5
<u>ORIFICE REGION</u>		
$v_o / \sqrt{\omega \nu}$	---	26
$S_o = \frac{d_o}{2} \sqrt{\frac{\omega}{\nu}}$	Shear wave number	8
t_o / d_o	Aspect ratio	0.5
<u>ORIFICE/HORN REGION INTERACTION</u>		
kLz_o / Z	Impedance ratio	$kL z_o / Z \approx 2.8$

to the frequency ratio used in vibrations, gives the ratio of ω to the first natural frequency of the horn chamber (as a closed cavity).

It will be shown in §2.4.1 that the wave equation governs the fluid flow in the horn region. This equation is linear and the value of P'/β gives an indication of when the order of magnitude assumptions used in the derivation are met.

The value of the shear wave number, S , reflects the influence of viscosity. Physically, $\sqrt{1/2\pi} S$ is equal to the ratio of tube diameter to boundary layer thickness.

As shown in Table 2.2, the physics of the fluid flow around the orifice are determined by three groups. Note that fluid compressibility is not contained in any of these groups; the small length scale involved precludes compressibility effects. Panton and Goldman [10] present an excellent discussion of the physics associated with oscillating flow through an orifice, for the case of $t_o/d_o < 0.1$. The results will be summarized here.

When experimental data were examined, S_o had some influence of the onset of nonlinear behavior and on the values of orifice impedance in the linear and nonlinear regions. However, the data correlated primarily with $v_o/\sqrt{\omega\nu}$. Thus, it appears that flow around an orifice is primarily a function of t_o/d_o and $v_o/\sqrt{\omega\nu}$, with a secondary influence by S_o .

There are five groups governing fluid/structure interactions. The value of the characteristic impedance ratio is an indication of the degree of fluid/structure interaction via a longitudinal wave mechanism. The coincidence frequency ratio controls the interactions of the fluid with the orifice plate, via a mechanism of longitudinal waves in the fluid interacting with bending waves in the plate. The value of the thickness modulus ratio indicates the relative compressibility of the fluid in the horn chamber as compared to the horn chamber structured elasticity.

Finally, the coupling between the fluid in the horn chamber and the orifice is governed by a single group, the horn/orifice impedance ratio. The definition of orifice impedance, z_o , and the physical

significance of the impedance ratio will be presented in §2.4.4 and §2.5, respectively.

2.4 Analysis

As shown in Fig. 2.2, typical input to a printhead is transient with frequency content at more than one frequency. However, the analysis presented will be for monochromatic input. Using superposition or other methods, solutions for nonmonochromatic input may be developed. It was felt that the monochromatic approach yields the most general results.

The fluid in a printhead is a water based ink and the properties were assumed to be those of water. However, there are ink particles present as large as 1/5 of the orifice diameter and so it is not clear that the continuum and Navier Stokes assumptions are valid in the fluid. However, based on laboratory experience with printheads, assuming the continuum and Navier Stokes assumptions appeared to be a good starting point.

2.4.1 The Horn Region

Suppose the following conditions are satisfied in the horn region: (i) $P' \ll \beta$, (ii) $\mu = k_c = 0$, and (iii) $\rho' \ll \rho$. Then it is possible to show that the fluid motion in the horn region is governed by (1), the wave equation.

$$\frac{\partial^2 a}{\partial t^2} - c^2 \nabla^2 a = 0 \quad (1)$$

where a can be any one of four variables, $\phi(\vec{x}, t)$, $\vec{V}(\vec{x}, t)$, $P'(\vec{x}, t)$, or $\rho'(\vec{x}, t)$.

Due to the radial symmetry of a printhead, (1) can be used in component form in terms of r , x , and t . However, it will now be shown that it is not necessary to include the radial dependence. The reason for this is that the radial effects are confined to regions near the boundaries.

Consider the following problem, solve:

$$\frac{\partial^2 \phi}{\partial t^2}(r, x, t) = c^2 \nabla^2 \phi(r, x, t)$$

subject to:

$$\frac{\partial \phi}{\partial x}(r, x=0, t) = f(r)e^{-i\omega t} \quad (2)$$

$$\frac{\partial \phi}{\partial x}(r, x=L, t) = \frac{\partial \phi}{\partial r}(r=R, x, t) = 0$$

$$\frac{\partial \phi}{\partial r}(r=0, x, t) \text{ is finite}$$

where the region of interest, Fig. 2.3, represents the ink-jet print-head with a 2D velocity distribution at one end and rigid walls on all the other boundaries. (Note: the 2D effects introduced by viscous interactions with the horn walls will be discussed in §2.4.5.) Adding a radial dependent boundary condition at both ends (i.e. piezoelectric crystal at one end and orifice at the other) can easily be done using superposition if the solution to (2) is known.

The solution to (2), given by:

$$\phi(r, x, t) = \sum_{n=0}^{\infty} \left[a_n J_0(k_{rn} r) \frac{\cos(k_{xn} (x-L))}{\sin(k_{xn} L)} \right]$$

where

$$a_n = \frac{\left[\int_0^R r f(r) J_0(k_{rn} r) dr \right]}{k_{xn} \left[\int_0^R r J_0^2(k_{rn} r) dr \right]} \quad (3)$$

$$k_{rn}^2 + k_{xn}^2 = k^2 = \left(\frac{\omega}{c}\right)^2$$

$$J_0(k_{rn} R) = 0 \rightarrow k_{rn} R = (0, 3.832, 7.016, \dots) \text{ for } n = (0, 1, 2, \dots)$$

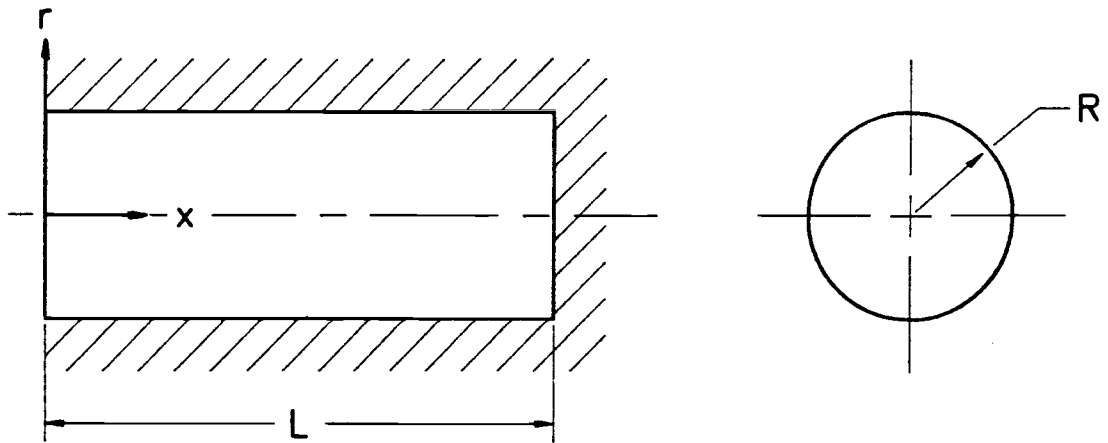


Fig. 2.3. The geometry for analyzing a two dimensional velocity boundary condition in a closed rigid wall tube

was found using standard methods of linear acoustics in ducts, [11,12]. The fluid pressure, velocity and density may be calculated using:

$$P'(r,x,t) = -\rho \frac{\partial \phi}{\partial t} (r,x,t) \quad (4)$$

$$V(r,x,t) = \vec{\nabla} \phi(r,x,t) \quad (5)$$

$$\frac{\rho'(r,x,t)}{\rho} = -\frac{\rho}{\beta} \frac{\partial \phi}{\partial t} (r,x,t) \quad (6)$$

respectively.

Now, examine the terms in (3). Since $J_0(0) = 0$, the $n = 0$ term has no radial dependence. For

$$\omega < \omega_c = \frac{7.663c}{D} \quad (7)$$

where ω_c is called the cutoff frequency, the values of k_{xn} are imaginary for the $n > 0$ terms. Using imaginary values of k_{xn} in (3), the magnitudes of the $n > 0$ terms drop off exponentially with distance from the 2D boundary. The remaining problem is to show that the magnitudes of these terms are sufficiently small that they may be dropped.

For the case of $\omega < \omega_c$, (3) may be used to find the length from the 2D boundary, L' , and frequency, ω , at which the $n = 1$ term has dropped off by 95%:

$$kL' \sqrt{\left(\frac{\omega_c}{\omega}\right)^2 - 1} > 3.688 \quad (8)$$

Since the $n > 1$ terms drop off faster than the $n = 1$ term, use of (8) will cover all the terms with radial dependence.

Using the values in Table 2.1., $\omega_c = 878$ khz. Similarly, (8) with L' equal to the horn length, indicates that below 860 khz the $n > 0$ terms will have dropped off by 95% at the closed end. Since 860 hz is approximately 40 times the characteristic ink-jet printhead

operating frequency, 2D effects are confined to regions very close to the ends of the horn region.

The conclusion is that only a 1D formulation of the wave equation is required in the horn region. It may be easily shown that the magnitude of the $n = 0$ term in (3) is equal to the radially averaged value of the 2D BC shown on Fig. 2.3.

2.4.2 Piezoelectric Driver

Development of a piezoelectric driver model was not a part of this work. However, there are results of the analysis in §2.4.1 which are useful for driver modeling and design. Since only the average displacement of the driver is important, analysis may be performed using a flat plate with an equivalent volumetric displacement. Furthermore, the fluid mechanics of ink-jet printheads are fundamentally the same regardless of the mechanical method to move fluid down the horn chamber.

2.4.3 Fluid/Structure Interactions

Fluid/structure interactions were analyzed because of the high frequencies present in an ink-jet printhead and the high value of the fluid bulk modulus. Two fluid/structure interactions were considered. A plate/fluid interaction occurs when the fluid interacts with the plates at the ends of the horn chamber. A cylinder/fluid interaction occurs between the walls of the horn chamber and the fluid.

First consider the analysis of a fluid/plate interaction. Assume no energy loss at the fluid/plate interface so that energy incident on the plate is either reflected back into the fluid or transmitted through the plate. Define the transmission coefficient, α , as:

$$\alpha \equiv \frac{\langle \text{Energy transmitted through plate} \rangle}{\langle \text{Energy incident on plate} \rangle} \quad (9)$$

where the brackets, $\langle \rangle$, denote a time average. To estimate α assume plane monochromatic waves in the fluid in which case:

$$\alpha = \left[\frac{\langle P'(x,t)V(x,t) \rangle_t}{\langle P'(x,t)V(x,t) \rangle_i} \right]_{\text{plate}} \quad (10)$$

where the subscripts t and i denote transmitted and incident; P' and V are fluid pressure and velocity evaluated at the plate surface.

Since the plate wave number times plate thickness is much less than one, plate thickness is not important. Thus the problem considered, Fig. 2.4, consists of a zero thickness plate characterized by a stiffness and mass per unit area of m' and k' ; where k' is an average bending stiffness. There are fluids on both sides of the plate denoted by subscripts 1 and 2.

The pressure fields in fluids 1 and 2 are:

$$P'_1(x,t) = P'_i e^{i(kx-\omega t)} + P'_r e^{-i(kx+\omega t)} \quad (11)$$

$$P'_2(x,t) = P'_t e^{i(kx-\omega t)}$$

where P'_i , P'_r , and P'_t are the magnitudes of the incident, reflected and transmitted pressures. By using (10) and (11), α may be written as:

$$\alpha = \frac{(\rho c)_1 P'_t}{(\rho c)_2 P'_i} \left(\frac{\widetilde{P'_t}}{P'_i} \right) \quad (12)$$

where \sim denotes complex conjugate.

To determine P'_t/P'_i , velocity continuity at the plate/fluid interface and Newton's second law applied to the plate were used. The end result is:

$$\alpha = \frac{(\rho c)_1 / (\rho c)_2}{\left(\frac{1 + (\rho c)_1 / (\rho c)_2}{2} \right)^2 + \left(\frac{\omega m'}{2(\rho c)_2} \left(\left(\frac{\omega}{\omega_{pc}} \right)^2 - 1 \right) \right)^2} \quad (13)$$

where k'/m' has been replaced by the coincidence frequency, ω_{pc} , squared. The coincidence frequency is the natural frequency for a plate vibrating with fluid loading.

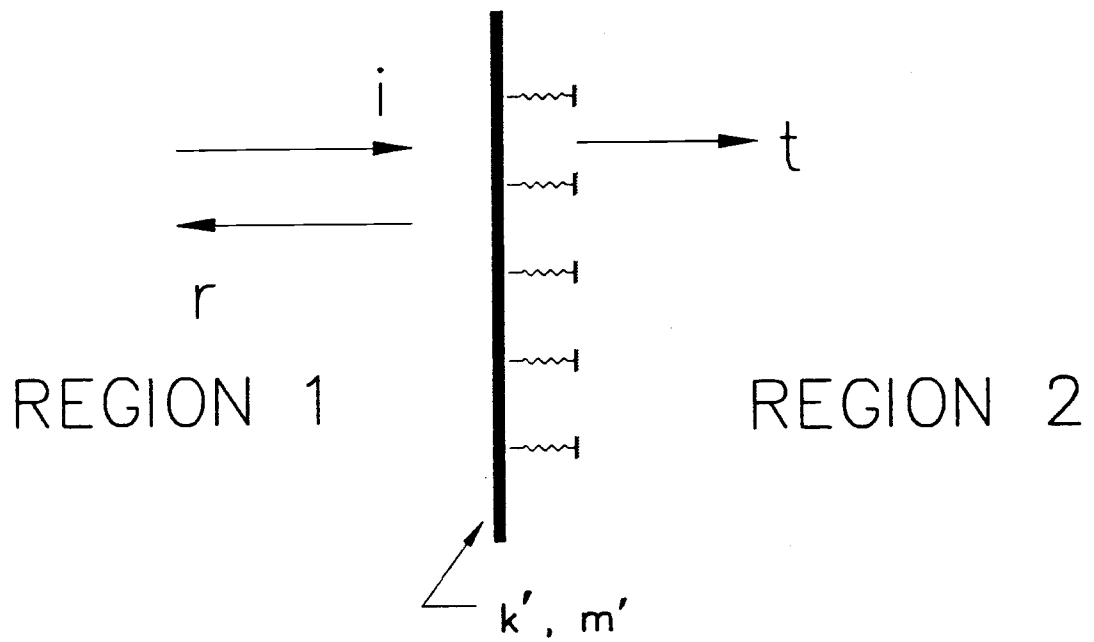


Fig. 2.4. A lumped plate model subjected to a monochromatic pressure field for transmission coefficient calculation

For a typical printhead, fluid 1 is water and fluid 2 is air and it is easily shown that:

$$\alpha < \frac{4}{(\rho c)_1 / (\rho c)_2} \approx 1.5 \times 10^{-4} \quad (14)$$

For the case where fluids 1 and 2 are both water (this occurs in printheads which employ a double orifice configuration) (13) reduces to:

$$\alpha = \frac{1}{1 + \left(\frac{\omega m'}{\rho c} \left(\left(\frac{\omega_{pc}}{\omega} \right)^2 - 1 \right) \right)^2} \quad (15)$$

The coincidence frequency for a metal plate in water is given by Ross [13] as:

$$\omega_{pc} = 1728/t \frac{\text{rad}}{\text{s}} \quad (16)$$

where t is plate thickness in meters. Using (15) and (16) $\alpha \approx 10^{-5}$ for the case where fluids 1 and 2 are water. Thus for both cases of interest in printhead operation, the plate will act as a rigid reflector.

Next, the fluid/cylinder interaction will be examined following methods used in water hammer analysis [14]. The idea is that both the fluid and the cylinder act as springs and thus the question is to determine their relative stiffness.

Define a compressibility factor, γ as:

$$\frac{1}{\gamma} \equiv - \frac{1}{V} \frac{\Delta V}{\Delta P} \quad (17)$$

where V is horn volume and P is pressure. Rewrite (17) as:

$$\frac{1}{\gamma} = - \frac{1}{V} \left(\frac{\Delta V}{\Delta P} \Big|_{\text{fluid compression}} + \frac{\Delta V}{\Delta P} \Big|_{\text{wall deformation}} \right) \quad (18)$$

From the definition of fluid bulk modulus, β :

$$\left. \frac{\Delta V}{\Delta P} \right|_{\text{fluid compression}} = -\frac{V}{\beta} \quad (19)$$

The volume change due to wall deformation is given by:

$$\begin{aligned} \Delta V \Big|_{\text{wall deformation}} &= \frac{\pi D^2}{4} \Delta L + \frac{2\pi DL}{4} \Delta D \\ &= \frac{\pi D^2 L}{4} (\epsilon_1 + 2\epsilon_2) \end{aligned} \quad (20)$$

where ϵ_1 is longitudinal strain and ϵ_2 is hoop strain.

Using simple pressure vessel theory with 2D elasticity stress/strain equations yields:

$$\epsilon_1 = \frac{\Delta PD}{4Ee} (1-2\nu_s) \quad (21)$$

$$\epsilon_2 = \frac{\Delta PD}{4Ee} (2-\nu_s)$$

Combining (20) and (21) yields:

$$\left. \frac{\Delta V}{\Delta P} \right|_{\text{wall deformation}} = -\frac{VD}{Ee} \left(\frac{5}{4} - \nu_s \right) \quad (22)$$

Combining (18), (19), and (22) yields:

$$\gamma = \frac{\beta}{1 + \frac{\beta D(5/4 - \nu_s)}{Ee}} \quad (23)$$

Equation (23) is valid for $e/D < 0.1$ and the horn chamber free to expand. The results for $e/D > 0.1$ and/or physical constraints on the expansion may be written in the form:

$$\gamma = \frac{\beta}{1 + \frac{\beta D}{Ee} C} \quad (24)$$

Where C is determined by e/D , the constraint and Poisson's ratio. Values of C for a number of cases are presented by Wylie and Streeter [14]. In all cases, C is of the order of 1.

From (17) and (24) it is seen that the physical effect of wall elasticity may be represented as a decrease in effective fluid bulk modulus. Furthermore, (24) may be used to determine when wall elasticity effects should be included. Letting $C = 1$ in (24), the horn chamber wall can be considered rigid (i.e., less than a 5% change in wave speed; $C = \sqrt{\beta/p}$) for $e/D > 0.1$.

2.4.4 The Orifice Region

The method for modeling the orifice region is to treat it as a BC for a solution to the wave equation in the horn region. In this section appropriate values of the orifice BC are discussed and in §2.5 a coupled solution for the horn chamber and orifice is presented.

The problem of sinusoidally oscillating zero mean flow through an orifice has been extensively studied in connection with muffler design, sound damping and other problems in acoustics [10,15-18]. Results are typically presented as a relationship between pressure across an orifice and the volume velocity through the orifice called the orifice impedance, z_o , defined as:

$$z_o = \frac{R - iX}{A_o} = \frac{P_1'(t) - P_2'(t)}{A_o v_o(t)} \quad (25)$$

for the geometry shown in Fig. 2.5. $P_1'(t)$ is a complex monochromatic sinusoidal pressure with magnitude P_1' . $v_o(t)$ is the complex fundamental harmonic component of the fluid velocity through the orifice with magnitude v_o . $P_2'(t)$ is the complex fundamental harmonic component of pressure at 2 with magnitude P_2' . The real and imaginary parts of orifice impedance as defined by (24) are called the resistance, R , and the reactance, X . In (25) impedance is written as $z_o = (R-iX)/A_o$. One should note that the sign on iX depends on the way that the solution to the wave equation is written. The minus sign is consistent with a solution of the form, $\phi(x,t) \approx f(x)e^{-i\omega t}$; which is used here. The plus sign would be used for a solution of the form, $\phi(x,t) \approx f(x)e^{+i\omega t}$.

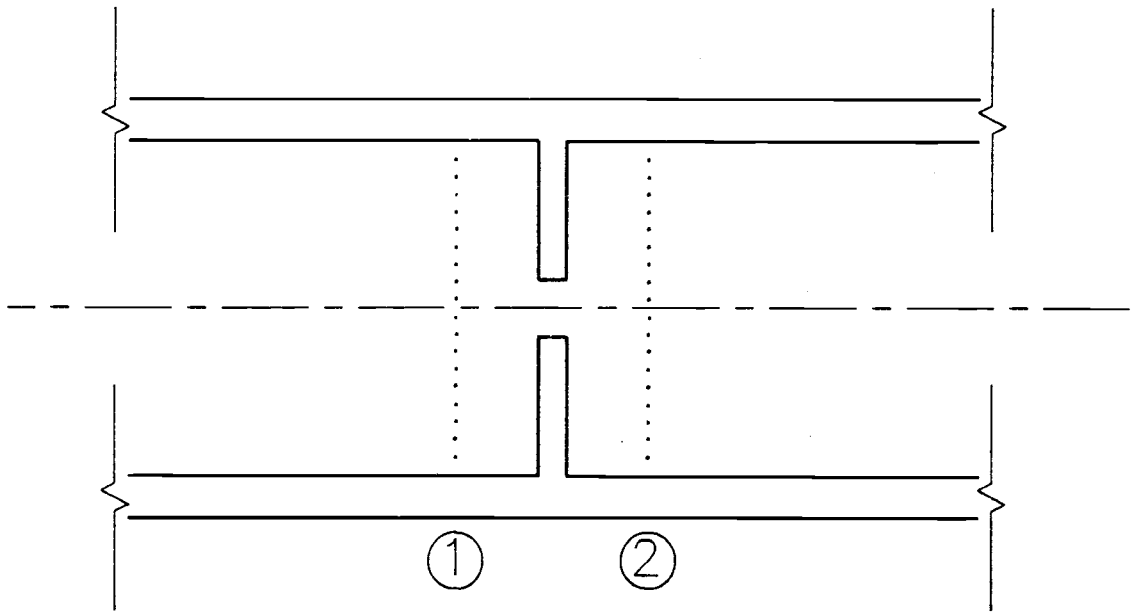


Fig. 2.5. Geometry for orifice impedance definition

The impedance approach derives from the idea that the fluid motion through the orifice is analogous to that of a vibrating piston. In this way the complicated fluid dynamics are lumped into a one degree of freedom model and the orifice is characterized by a mass and damping term. The mass term, embodied in the reactance, contains contributions from the fluid within the orifice and the fluid in the near field of the orifice (added mass). The damping term, or resistance, is primarily due to viscous losses in the near field of the orifice and contains a lesser contribution from losses within the orifice.

Typical curves for R , X , and z_o are presented in Fig. 2.6 as a function of v_o . At low values of v_o the curves approach a region where X and z_o are not dependent on v_o , called the linear region. However, R , X , and z_o usually depend on v_o and in this case these parameters are in the nonlinear range. This nomenclature is used because when an impedance BC is formulated for a problem, the BC will be nonlinear (linear) when v_o is in the nonlinear (linear) region. This is discussed further in §2.5.3.

Semi-theoretical predictions of R and X have been presented and validated for the linear regime. The model uses a combination of Crandall's [19] solution for oscillating fluid flow in an infinite length tube, a theoretical correction to X for end effects [20] and an empirical correction to R for end effects.

Thus, in the linear regime z_o is given by:

$$z_o = \frac{i\rho\omega(t_o + \delta)}{A_o \left(1 - \frac{J_1(i^{3/2}S_o)}{J_o(i^{3/2}S_o)} \frac{2}{i^{3/2}S_o} \right)} \quad (26)$$

where δ is an end correction. If $S_o < 1$ (26) will reduce to:

$$z_o = \frac{1}{A_o} \left(\frac{8\rho\omega(t_o + \delta)}{S_o^2} - i \frac{4}{3} \rho\omega(t_o + \delta) \right) \quad (27)$$

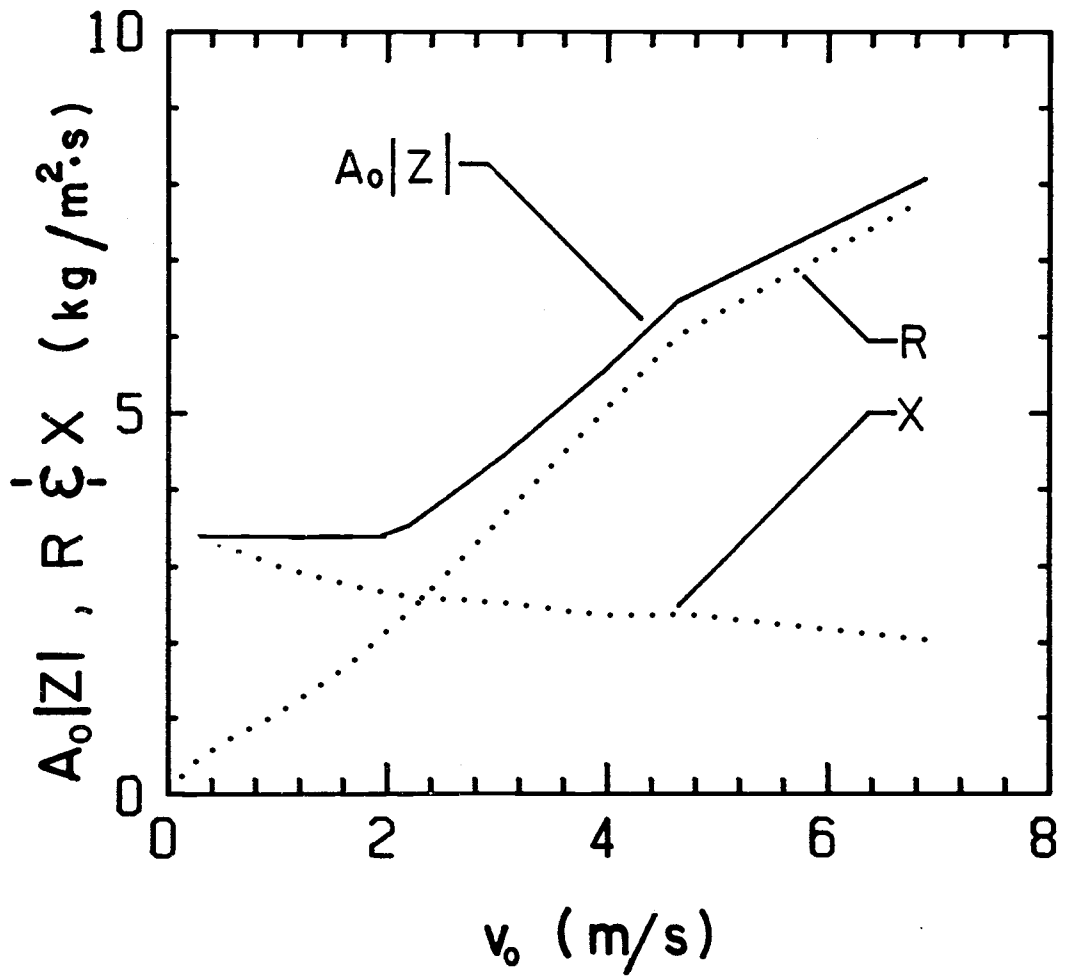


Fig. 2.6. Orifice impedance, resistance, and reactance as a function of the orifice velocity magnitude, v_o .

and if $S_o > 10$, (26) will reduce to:

$$z_o = \frac{1}{A_o} (\sqrt{2\mu\rho\omega} (t_o + \delta) - i\rho\omega(t_o + \delta)) \quad (28)$$

The end correction for reactance,

$$\delta = \frac{8d_o}{3\pi} \cong 0.85 d_o \quad (29)$$

is equal to twice the added mass due to fluid loading for the classical problem of a piston vibrating in an infinite wall. The end correction for the resistance has been experimentally determined to also be given by (29) even though there is no obvious physical explanation, [15,21].

In the nonlinear impedance regions, values of R and δ are found experimentally. The typical form is:

$$z_o = \frac{1}{A_o} [R(v_o) - i\rho\omega(t_o + \delta(v_o))] \quad (30)$$

where R and δ are functions of orifice velocity magnitude, v_o .

References previously cited and others cited therein contain a large pool of data. However, most of the data is presented in a dimensional form and there is some lack of agreement between references. Panton and Goldman [10], present an excellent dimensional analysis study of orifice impedance and nondimensionalize and correlate data from a number of references for the case of $t_o/d_o < 0.1$. It should also be mentioned that there are fluid dynamics based analytical models which predict impedance, see for example Hersh and Rogers [17].

2.4.5 Viscous Effects in the Horn Region

Tijdeman [22], in an excellent review article, presents a solution for the fluid dynamics of oscillating zero mean flow in a long tube. This solution is equivalent to solving the wave equation, (1), in a duct with viscous and thermal transport properties included.

Since end effects were shown to be confined to the near field of the ends of the horn chamber in §2.4.1, Tijdeman's solution may be used to examine effects of viscosity in the horn region. It is shown in [22] that when:

$$\kappa = \frac{\omega D}{2c} \ll 1 \quad (31)$$

and

$$\kappa/S \ll 1 \quad (32)$$

$P'(r,x,t)$ is given by:

$$\frac{P'(r,x,t)}{P} = (Ae^{\Gamma kx} + Be^{-\Gamma kx})e^{-i\omega t} \quad (33)$$

and $V(r,x,t)$ is given by:

$$\frac{V(r,x,t)}{c} = \frac{i\Gamma}{\gamma} \left[1 - \frac{J_0(i^{3/2}S r/R)}{J_0(i^{3/2}S)} \right] [Ae^{\Gamma kx} - Be^{-\Gamma kx}] \quad (34)$$

where the propagation constant, Γ , is given by:

$$\Gamma = \sqrt{\frac{J_0(i^{3/2}S)}{J_2(i^{3/2}S)}} \frac{\gamma}{n} \quad (35)$$

with

$$n = \left[1 + \frac{\gamma-1}{\gamma} \frac{J_2(i^{3/2}\sigma S)}{J_0(i^{3/2}\sigma S)} \right]^{-1}$$

where γ is the specific heat ratio and σ is the square root of the Prandtl number.

From (33) and (34) viscosity introduces 2D effects into the velocity profile given in (34) and produces an attenuation with dis-

tance determined by the value of Γ . Velocity profiles as a function S are presented in Fig. 2.7. Plots of $\Gamma(S)$, presented in [25], show that above $S \approx 7$, $\Gamma = 1$, the unattenuated case.

Because $S \approx 350$, it may be concluded that viscosity will have little influence on the fluid dynamics in the horn region. An exception is for frequencies near resonance in the horn region, $\omega_n = n\pi/2L$, damping mechanisms are quite important in determining system behavior.

2.5 A System Model

2.5.1 The Piston Driven Helmholtz Resonator

Based on the analysis presented in §2.4, the following assumptions were made with regards to modeling an ink-jet printhead.

- (i) The structural materials including the orifice plate will act as rigid reflectors. There will be no coupled fluid/structure interactions.
- (ii) The 1D linear wave equation is valid in the horn region.
- (iii) The orifice may be treated as a boundary condition using the impedance concept.
- (iv) The piezoelectric crystal may be modeled as a flat piston with a displacement equal to the radially averaged value of the actual device.
- (v) Fluid thermal and momentum transport coefficients are zero in the horn region.

With these assumptions, the model of the printhead, Fig. 2.8, can be viewed equivalently as an ink-jet printhead or as a piston driven Helmholtz resonator. The problem to be solved may be formulated as:

solve:

$$\frac{\partial^2 \phi(x,t)}{\partial t^2} - c^2 \frac{\partial^2 \phi(x,t)}{\partial x^2} = 0 \quad (36)$$

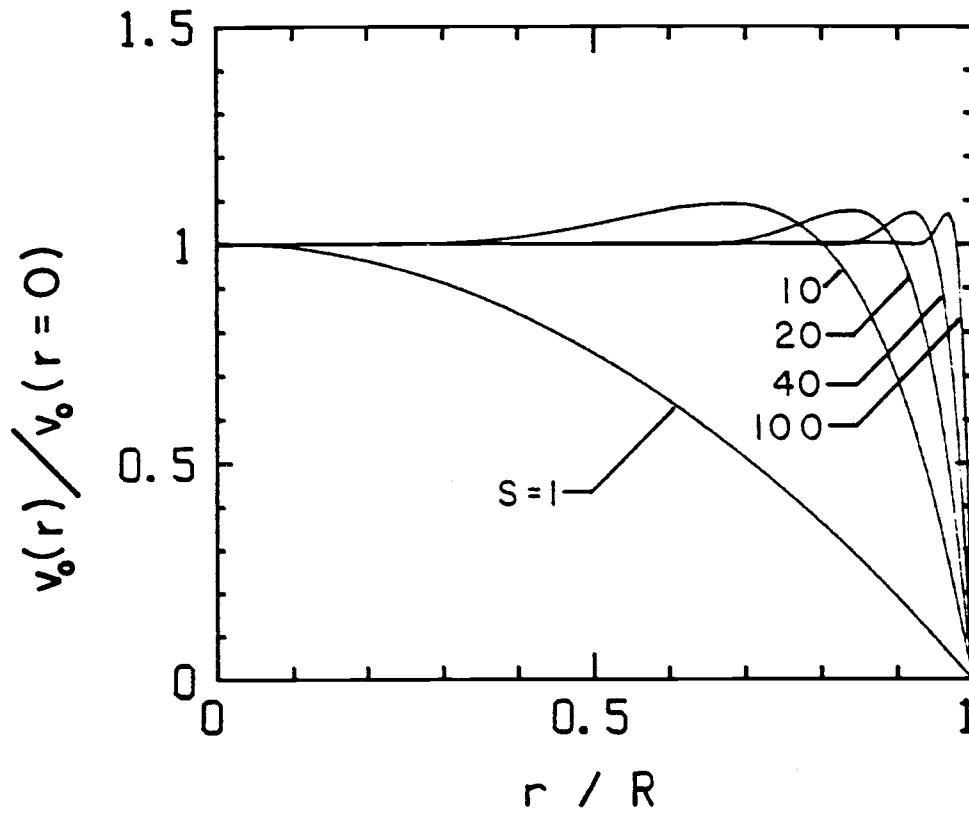


Fig. 2.7. Axial velocity profiles in a long tube as a function of shear wave number, S

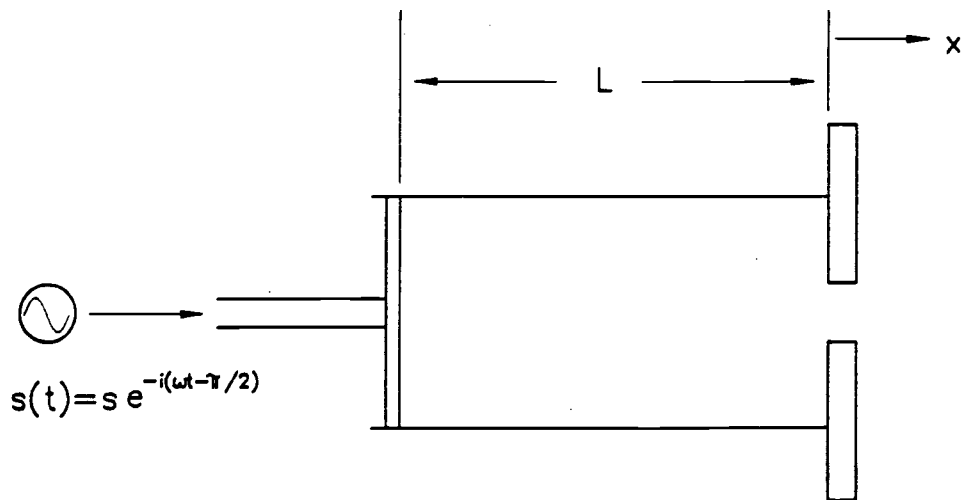


Fig. 2.8. A piston driven Helmholtz resonator subjected to monochromatic input

subject to:

$$\frac{\partial \phi(x = -L, t)}{\partial x} = \dot{s}(t) = \omega s e^{-i\omega t} \quad (37)$$

$$\frac{P'(x=0, t)}{V(x=0, t)A} = \frac{-\rho \frac{\partial \phi(x=0, t)}{\partial t}}{A \frac{\partial \phi(x=0, t)}{\partial x}} = z_o \quad (38)$$

The solution to (36) is:

$$\phi(x, t) = a(e^{ikx} + be^{-ikx}) e^{-i\omega t} \quad (39)$$

Applying BCs (37) and (38) to (39) to solve for constants a and b , and using (4) and (5) yields:

$$V(x, t) = \omega s \frac{(\cos(kx) + i \frac{z_o}{Z} \sin(kx))}{(\cos(kL) - i \frac{z_o}{Z} \sin(kL))} e^{-i\omega t} \quad (40)$$

$$P'(x, t) = i\rho c\omega s \frac{(\sin(kx) - i \frac{z_o}{Z} \cos(kx))}{(\cos(kL) - i \frac{z_o}{Z} \sin(kL))} e^{-i\omega t} \quad (41)$$

where $Z = \rho c/A$ is the characteristic fluid impedance.

Equations (40) and (41) are the desired result, the solution to the pressure field in a piston driven Helmholtz resonator. There are a number of important comments about these equations.

In the usual case when orifice impedance, z_o , is a function of the orifice velocity (nonlinear), (40) and (41) must be solved iteratively. Panton and Goldman [10] present a good summary of thin orifice impedance data taken with systems using air, water, and oil as the working fluids. For orifices with $t_o/d_o > 0.1$, data in the literature is more difficult to find.

The impedance ratio, $(\sin kL)z_o/Z \approx kLz_o/Z$, governs the interactions of the orifice with the horn region. When it is sufficiently large, the fluid in the horn region behaves as if the orifice was not

present and (40) and (41) reduce to (42) and (43), the equations governing the fluid motion in a closed tube, Tempkins [11].

$$V(x,t) = \frac{-\omega s \sin(kx)}{\sin(kL)} e^{-i\omega t} \quad (42)$$

$$P'(x,t) = \frac{i\rho c \omega s \cos(kx)}{\sin(kL)} e^{-i\omega t} \quad (43)$$

If z_o is taken to be purely reactive:

$$z_o = \frac{-i\rho\omega(t_o + \delta)}{A_o} \quad (44)$$

the usual formula for the natural frequency of a Helmholtz resonator can be recovered from (40) or (41).

$$\omega_h = c \sqrt{\frac{A_o}{(t_o + \delta)AL}} \quad (45)$$

When z_o contains a resistive component, R , (45) still provides a good estimate of ω_h .

Also note that (42) and (43) may be used to derive closed tube natural frequencies at:

$$\omega_n = \frac{n\pi c}{L} \quad (46)$$

In many cases at the frequencies given by (46), kLz_o/Z is sufficiently large such that the resonator is behaving like a closed tube and (46) provides good estimates of the resonator's higher natural frequencies.

The derivation of (40) and (41) was done using a BC of known piston displacement-vs-time. It could also have been solved using a BC of a known force (or voltage with appropriate transfer function) applied to a piston modeled as a mass, spring and damper. In this case an additional parameter, the mechanical impedance of the piston divided by the horn impedance would appear. In this way the desired impedance match of the driver could be modeled.

2.5.2 Application to Ink-jet Printheads

If surface tension effects are introduced, what is the validity of the previous analysis? The approach used to answer this question was to include surface tension effects as a stiffness parameter modifying the orifice characteristics. Thus let z_o be given by:

$$z_o = \frac{1}{A_o} (R_s - iX_s) = \frac{1}{A_o} \left(R_s + i \left(\frac{k_s}{\omega} - \rho \omega (t_o + \delta) \right) \right) \quad (47)$$

where k_s is the stiffness/area due to surface tension effects. The subscript s is used to denote that the usual values of δ and R would change due to the surface tension boundary.

When the same fluid is on both sides of the orifice δ and R are due to end effects with an approximately equal contribution from each side of the orifice. Thus let:

$$R_s = R/2 \quad (48)$$

and

$$\delta_s = \delta/2 \quad (49)$$

To estimate k_s , assume drops develop with equal principle radii of curvature as shown in Fig. 2.9. Then,

$$k_s = \frac{\tau}{x_d^2 + d_o^2/4} \quad (50)$$

where τ is surface tension. Using (47) and (50), the ratio of stiffness to mass characteristics may be calculated:

$$\frac{\text{stiffness}}{\text{mass}} = \frac{\tau}{(x_d^2 + d_o^2/4)\omega^2\rho(t_o + \delta/2)} \quad (51)$$

For $x_d = 0$, this ratio is 0.17. Thus, surface tension effects are of the same order of magnitude as the mass and damping effects intro-

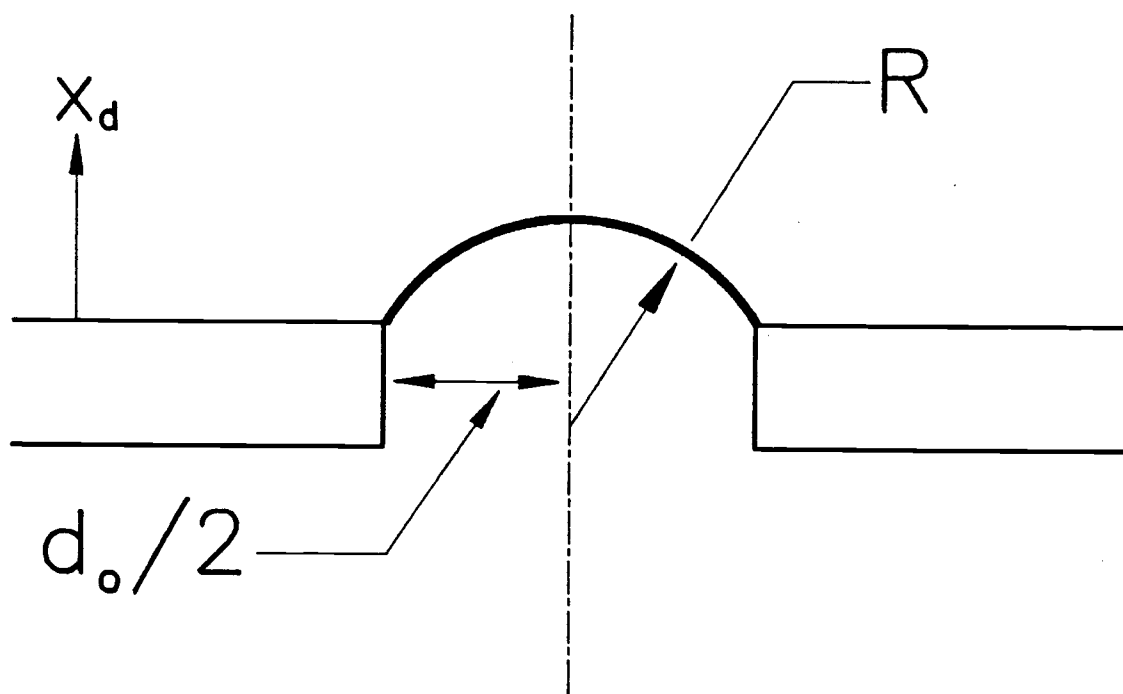


Fig. 2.9. Geometry for drop development

duced by the orifice. The use of (40) and (41) with an analytical estimate of k_s should be reasonable.

2.5.3 A Simple Analogy

A simple mechanical analogy of an ink-jet printhead is presented in Fig. 2.10. The relationships of the analogy are presented in Table 2.3.

The fluid in the horn region, represented by the elastic element, has only the attribute of stiffness. M represents the orifice's mass characteristic associated with the acceleration of fluid in and near the orifice. The damping, C , represents the energy losses created by the flow oscillating through the orifice. The stiffness, K , is due to surface tension effects.

The impedance mismatch of §2.5.1 occurs when M and C are so large that they appear as a rigid wall to the elastic element.

The question of whether the elasticity of the elastic element needs to be incorporated into the model (does the fluid need to be modeled as compressible?) depends of the relationship of ω to ω_n ; and on the values of M , C , and K relative to the elastic element's properties. For an ink-jet, most of the compressibility is due to the later.

Equation (40) or (41) can be used to determine if the elastic element can be modeled as rigid, as a 1-degree-of-freedom system or using a partial differential equation. Of course, (39) and (40) are a representation of the later of these choices and thus will reduce to the simpler cases when they apply.

2.5.4 Design of an Ink-Jet Printhead

In this section an example ink-jet printhead design is developed using the information from §2.5.1-§2.5.3. It is stressed that the intent is to describe a way to think about ink-jet printhead design and many details were not included.

The objective was to design an ink-jet printhead to produce 70 μm drops at a maximum repetition rate of 4000 drops/s. A printhead geometry similar to that shown in Fig. 2.1 was selected. Since

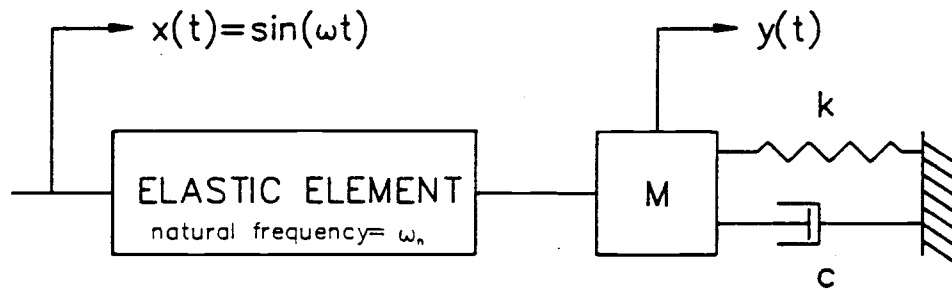


Fig. 2.10. Mechanical analogy of an ink-jet printhead

Table 2.3. Mechanical, electrical, and acoustic analogies.

Mechanical Analogy	Electrical Analogy	Orifice Analogy
Position	Charge	Particle position*area = $y(t)$
Velocity	Current	Volume velocity = $v_o(t)A_o$
Mass	Inductance	Mass/area ² = $\rho t_o/A_o = X/(\omega A_o)$
Damping	Resistance	Damping/area ² = R/A_o
Force	Voltage	Pressure = P'
Stiffness	Inverse Capacitance	Stiffness/area ²

the mode shape of the piezoelectric driver was not important, the driver was conceptualized as a piston with an equivalent volumetric displacement. To simplify matters, no refill mechanism was included. The ink fluid properties were assumed to be those of water.

From a design standpoint, the interest was in producing a given fluid displacement-vs-time out the orifice. In other words, design to control when and how much fluid comes out the orifice. The idea underlying the design process was to make the mass, M , of Fig. 2.10 move in a desired fashion.

An orifice volumetric fluid displacement as a function of time, $y(t)$, Fig. 2.11, was selected as the design waveform. Note that a different waveform could have been selected without any real change in the approach. The characteristic time for $y(t)$ is $T = 83 \mu s$, corresponding to a frequency of 12 khz. The magnitude, y_m , of $y(t)$ corresponds to the volume of one drop, $y_m = 4\pi r_d^3/3 = 1.80 \times 10^{-13} \text{ m}^3$.

To analyze a printhead capable of producing the Fig. 2.11 output, a solution method for non-monochromatic input was required. One method examined was the use of superposition with the §2.5.1 monochromatic solution. However, there were two significant problems. First, how is superposition used with (40) and (41)? Second, if superposition would work, what about the nonlinear orifice impedance BC?

To use superposition, it was necessary to slightly alter the formulation given in (36)-(38). In particular let z_0 be given by (47) and then if the BC given by (38) is written as:

$$\left[\frac{\rho(t_0 + \delta)}{A_0} \frac{\partial^2 \phi}{\partial x \partial t} + \frac{R_s}{A_0} \frac{\partial \phi}{\partial x} + \frac{k_s}{A_0} \int^t \frac{\partial \phi}{\partial x} dt = - \frac{\rho}{A} \frac{\partial \phi}{\partial t} \right]_{(x=0, t)} \quad (52)$$

superposition will work, provided (52) is linear. However, in the regions of interest, z_0 is nonlinear and consequently R and δ are functions of v_0 . From (50) it is seen that k_s also introduces nonlinearities.

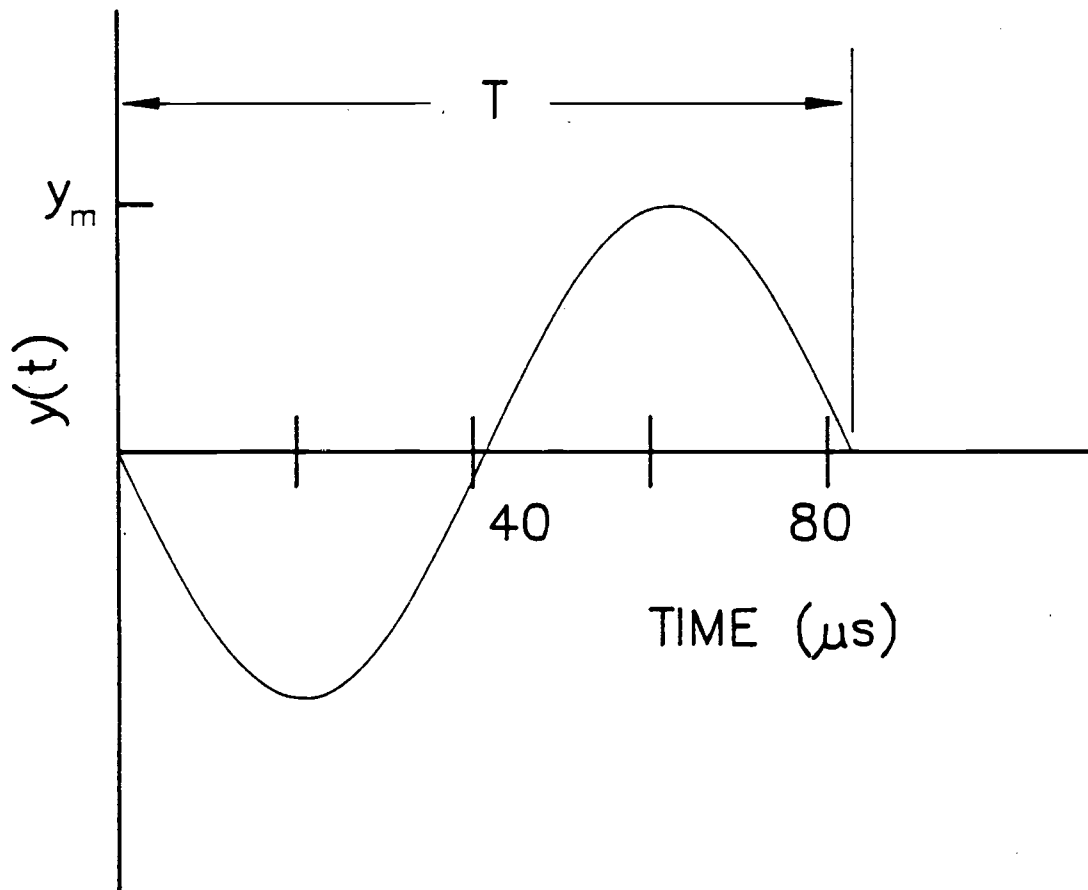


Fig. 2.11. The design fluid volumetric displacement, $y(t)$, out the orifice

The set of equations to be solved is (36), (37), and (52). They may be solved numerically or by linearizing (52) and using superposition. Unfortunately, no general approach to linearizing (52) was found. Furthermore, a numerical solution was not selected because it would tend to obscure some of the important physics. Instead, the following approach was developed.

From Fig. 2.10 it is seen that the ink-jet printhead may be conceptualized as a spring-mass-damper system. Equation (41) may be used to determine that when:

$$|\cos(kx)z_o/Z| \gg |\sin(kx)| \quad \text{for } -L \leq x \leq 0 \quad (53)$$

pressure in the horn chamber does not depend on axial position, x . In this case a lumped formulation for the horn chamber may be used in modeling the ink-jet printhead.

Assuming that (53) would apply to the final design, an ordinary differential equation was formulated for the printhead. This was derived using a force balance on the fluid in the orifice together with the continuity equation and the definition of β . As a check it was also derived using (25) and (40). The result is:

$$M\ddot{y}(t) + (R_s/A_o)\dot{y}(t) + (k'_s + k_h)y(t) = k_h x(t) \quad (54)$$

where:

$y(t)$ = orifice fluid volumetric displacement

$x(t)$ = piston volumetric displacement = $A_s(t)$

M = mass term = $\rho(t_o + \delta_s)/A_o$

R_s = damping term modified for liquid/air boundary

k'_s = stiffness due to surface tension per unit orifice area²

k_h = stiffness due to fluid in horn chamber = $\rho c^2/L A$

Equation (54) is still nonlinear, but it is easier to solve than the previous case and it is much easier to place a physical significance on each of the terms. The nonlinear terms are of the form

$k_s = k_s(y(t))$, $R = R(\dot{y}(t))$ and $\delta = \delta(\dot{y}(t))$. However, only R was used in its nonlinear form. While use of the other terms in their non-

linear forms would be the most accurate, the added complexity would not add any additional insight into the physics.

k_s was fixed by setting $x_d = d_o/\sqrt{2}$ in (50). To determine δ and R , the data correlated by Panton and Goldman [10] was used. The data from [10] is valid for the case of $t_o/d_o < 0.1$ but was used due to a lack of data for $t_o/d_o > 0.1$. Correcting for the surface tension BC using (49), a fixed value of δ_s was used such that $\delta_s/0.85d_o = 0.4$. Similarly using (48) with curves presented in [10] yielded an equation for R as a function of v_o . It was assumed that damping was proportional to velocity magnitude and then using (48) an equation for R_s could be written as:

$$R_s = \frac{0.87}{2} \rho |\dot{y}(t)| / A_o \quad (55)$$

Using (55) and nondimensionlizing (54) with $t^* = \omega t$, $y^* = y/y_m$, $x^* = x/y_m$ yields:

$$\ddot{y}^* + 2\zeta\left(\frac{\omega_o}{\omega}\right) \dot{y}^* |\dot{y}^*| + (\omega_o/\omega)^2 y^* = \left(\frac{\omega_h}{\omega}\right)^2 x^* \quad (56)$$

where

$$\zeta = \frac{0.87 \rho y_m \omega}{A_o^2 \sqrt{M(k'_s + k_h)}}$$

$$\omega_h = \sqrt{k_h/M}$$

$$\omega_o = \sqrt{\frac{k'_s + k_h}{M}}$$

which is the desired result.

From (56) it is seen that for the case of interest an ink-jet printhead is completely characterized by three dimensionless groups; which are a damping factor and two natural frequency ratios. By varying the values of the groups it is possible to design the print-head to produce any reasonable output.

The procedure followed was to develop a fourth order Runge-Kutta numerical solution to (56) and perform parametric studies to get a feel for a desirable printhead design in terms of the three dimensionless groups. Four typical parametric study cases are shown on Fig. 2.12. The results of the parametric studies were that an ink-jet printhead should be designed with a value of $\omega_0/\omega > \approx 1.3$ and $\zeta > \approx 0.8$. As ω_0/ω increases, the required damping ratio will decrease.

An additional important conclusion from the parametric studies was that one could think about the design in terms of a linear system with constant parameters. In other words, one could examine the Bode diagrams for a single degree of freedom spring/mass/damper system [23], and select values of the frequency ratio and the damping factor and come reasonable close to a good design.

The final design was produced by solving (56) numerically using a fourth order Runge-Kutta algorithm. The relationship between $x(t)$, $y(t)$, and $\dot{y}(t)$ is shown on Fig. 2.13. The printhead geometry is cylindrical with dimensions of $L = 2200 \mu\text{m}$, $D = 2000 \mu\text{m}$, $d_o = 39 \mu\text{m}$ and $t_o = 13 \mu\text{m}$. The maximum fluid volumetric displacement out the orifice is $1.80 \times 10^{-13} \text{ m}^3$ and the maximum driver volumetric displacement is $1.86 \times 10^{-13} \text{ m}^3$. It is seen that the output, $y(t)$, is reasonable close to the desired output shown on Fig. 2.11. The ringing shown could be reduced further by adding damping to the horn chamber.

It may be noted that the Fig. 2.12d design has better performance than the final design. The reason the final design was selected was its larger geometry as compared with that used for the Fig. 2.12d curves. This illustrates a fundamental limitation on ink-jet printhead design: For a given drop size, increasing the speed/performance of the printhead requires a decrease in the horn chamber size. Conversely, increasing speed/performance can be achieved by decreasing the orifice/drop diameter.

Finally, as previously mentioned, a mechanism for horn refill was not included in any of the analyses presented in this chapter. It would seem appropriate to discuss the influence of neglecting horn refill. In a physical sense, the fluid dynamics in a printhead horn

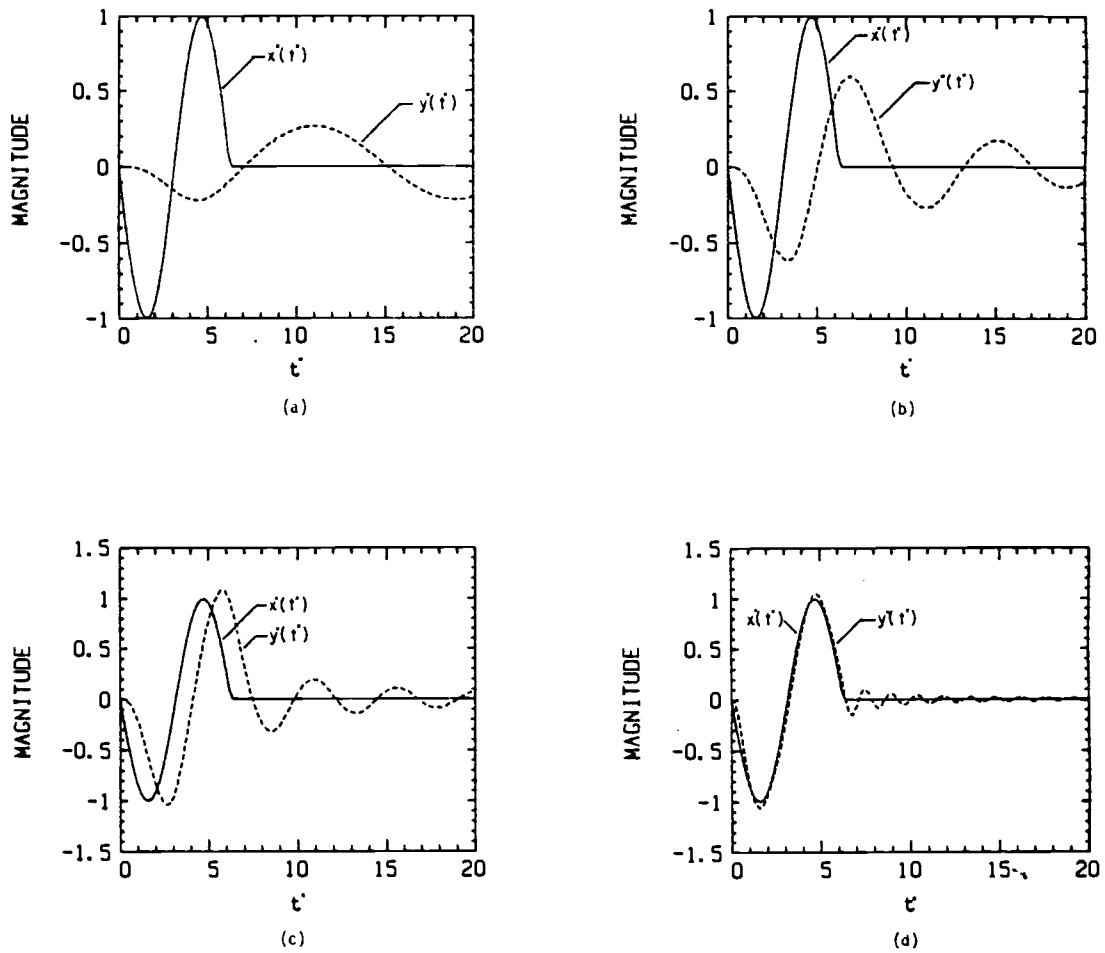


Fig. 2.12. Example performance curves for parametric study cases:

(a) $\omega_o/\omega = 0.39$, $\omega_h/\omega = 0.24$, $\zeta = 0.74$

(b) $\omega_o/\omega = 0.80$, $\omega_h/\omega = 0.63$, $\zeta = 0.90$

(c) $\omega_o/\omega = 1.36$, $\omega_h/\omega = 1.27$, $\zeta = 0.53$

(d) $\omega_o/\omega = 4.37$, $\omega_h/\omega = 4.33$, $\zeta = 0.25$

The dimensional variables are:

(a) $D = 4000 \mu\text{m}$, $L = 30000 \mu\text{m}$, $d_o = 60 \mu\text{m}$, $t_o = 22.5 \mu\text{m}$

(b) $D = 3000 \mu\text{m}$, $L = 6000 \mu\text{m}$, $d_o = 45 \mu\text{m}$, $t_o = 15 \mu\text{m}$

(c) $D = 3000 \mu\text{m}$, $L = 1500 \mu\text{m}$, $d_o = 45 \mu\text{m}$, $t_o = 15 \mu\text{m}$

(d) $D = 1000 \mu\text{m}$, $L = 1000 \mu\text{m}$, $d_o = 39 \mu\text{m}$, $t_o = 13 \mu\text{m}$

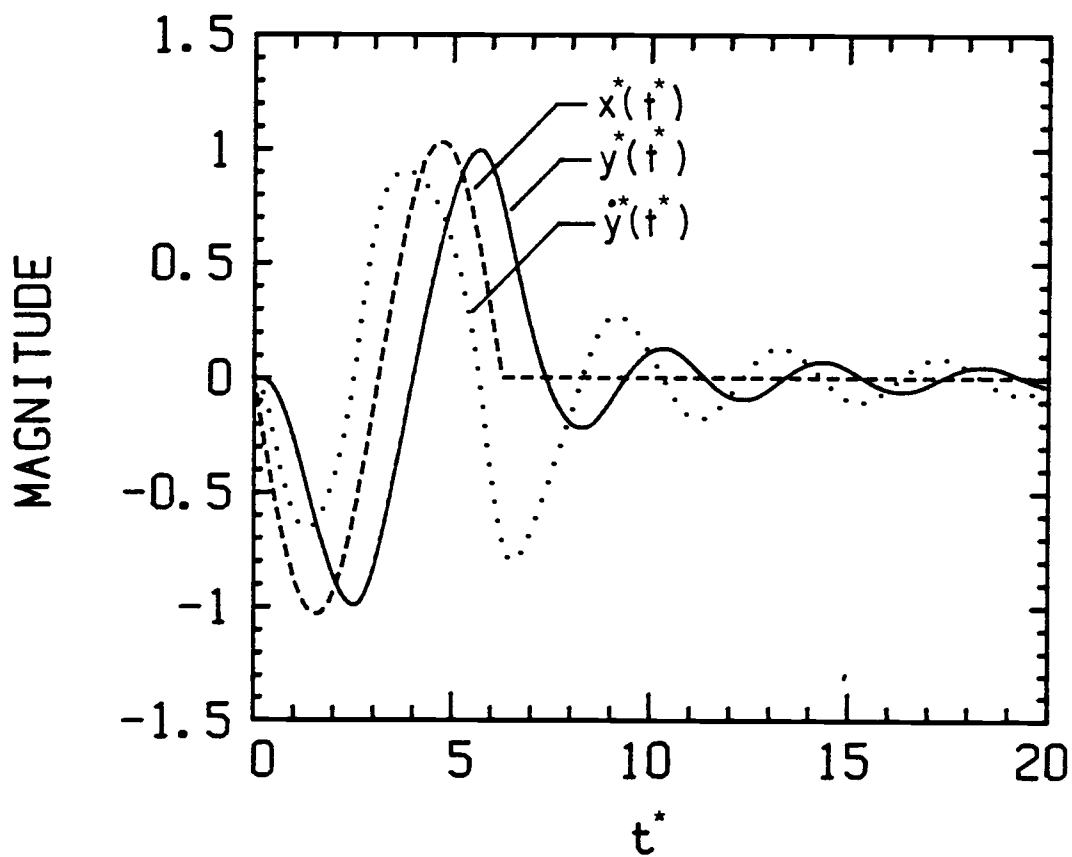


Fig. 2.13. Performance curves for the final design

chamber is separate from that in the orifice region. Thus, the refill port will effect the operation of a printhead by (i) influencing the horn characteristics by the addition of a damping term, a mass term, and perhaps a stiffness term (i.e., an impedance) to the horn's stiffness characteristic and by (ii) adding another degree of freedom (fluid volumetric displacement out the refill port) to the system. While the analysis to incorporate these effects was not performed, it would appear that some of the physical interpretations and methods presented would be useful for such an analysis.

2.6 Conclusions

A simple model of an ink-jet printhead has been developed together with a simple mechanical analogy, Fig. 2.10. In the development of this model it was shown that the ink-jet printhead may be viewed as piston driven Helmholtz resonator. The use of a mechanical analogy of an ink-jet printhead and/or a Helmholtz resonator is really nothing new. However, since the analysis presented in support of this approach is traceable to the fundamental governing equations, the applicability of the model may be determined for a wide variety of cases. In addition, the analysis provides a good set of tools for analyzing more complicated geometries and/or operating conditions.

It was shown how the simple model developed from the analysis could be used for an ink-jet printhead design. Ink-jet printhead operating characteristics are primarily a function of the damping introduced by the orifice and the ratio of the Helmholtz natural frequency to the printhead characteristic driving frequency.

The analysis also provided other useful information. The only mode of fluid/structure interaction in an ink-jet printhead likely to become important is that between the fluid and the horn chamber wall. For $e/D > 0.1$, this effect is not important; below this value it can be accounted for by modifying kL .

With regards to the design of the driving element of an ink-jet printhead, the only variable influencing the internal fluid mechanics is volumetric displacement. For analysis purposes, there is no reason or benefit to a 2D model of the driver (unless required to cor-

rectly predict volumetric displacement). Similarly, except for the near field of the orifice, there is no reason or benefit to a 2D fluid model.

A dimensional analysis of a simplified ink-jet printhead has been performed. The dimensionless groups were treated separately in different regions of the printhead to reflect the differences in the physics. The analysis performed allowed the effects of the dimensionless groups to be determined. The fluid mechanics in the horn chamber are governed by kL and L/D . In addition P'/β becomes important as it approaches a large value and S becomes important as it approaches a small value. The fluid mechanics in the orifice region are governed primarily by $v_o/\sqrt{\omega v}$ and t_o/d_o with a weak influence by S_o . The coupling between the fluid dynamics in the orifice region and the horn chamber is contained in a single group, the horn/orifice impedance ratio written as kLz_o/Z .

For an experimental study, proper scaling may be achieved by matching the important dimensionless groups presented in the previous paragraph. However, it is important to note that since the physics in the different region of the printhead are independent, a study of a specific part of an ink-jet printhead need not match all the groups. For example, a study of orifice impedance does not require matching the groups governing fluid mechanics in the horn region.

Since accurate values of orifice impedance, z_o , are the key to the usefulness of the methods presented; measurement of this parameter would appear to be the most important goal of an experimental project.

CHAPTER 3

DYNAMIC CALIBRATION OF A CONSTANT TEMPERATURE HOT WIRE
ANEMOMETER IN A ZERO MEAN OSCILLATING FLOW**3.1 Introduction**

The constant temperature hot wire anemometer has been well established as an instrument for measuring steady laminar and turbulent flows. This project arose from a need to measure a reversing flow which has a sinusoidal time behavior, Fig. 3.1a. It was initially thought that a static calibration would be adequate to interpret the anemometer voltage signal but this was not the case. Figure 3.1b shows three bridge voltage signals corresponding to three values of velocity. The minimum voltage, which correlates with flow reversal, would be the same for all three cases if a static calibration was valid. Coupled with other interpretation problems, a need to establish the relationship of bridge voltage to dynamic fluid velocity was identified.

The approach developed was to design an apparatus to produce a sinusoidal flow field, Fig. 3.1a, with known magnitude and phase. By inserting a hot wire probe into this flow field a relationship between fluid velocity and bridge voltage was found. Results are presented for frequencies of 25, 45, and 70 hz and amplitudes from 0.03 m/s to 4 m/s. It was determined that (i) the static calibration was reasonably accurate for predicting the maximum amplitude of the velocity and that (ii) the static calibration was not accurate for determining the phase of the velocity or for interpreting the velocity around the points of flow reversal.

There are a number of studies on the dynamic calibration of hot wire systems with application to turbulence measurements. In these studies, the procedure was to produce a steady flow plus a small sinusoidal component by mechanically oscillating the hot wire probe in a steady flow. What is of interest is to compare the slope of the static calibration curve, $\partial U/\partial v$ (U = bridge voltage, v = velocity amplitude), with that estimated from the dynamic calibration proce-

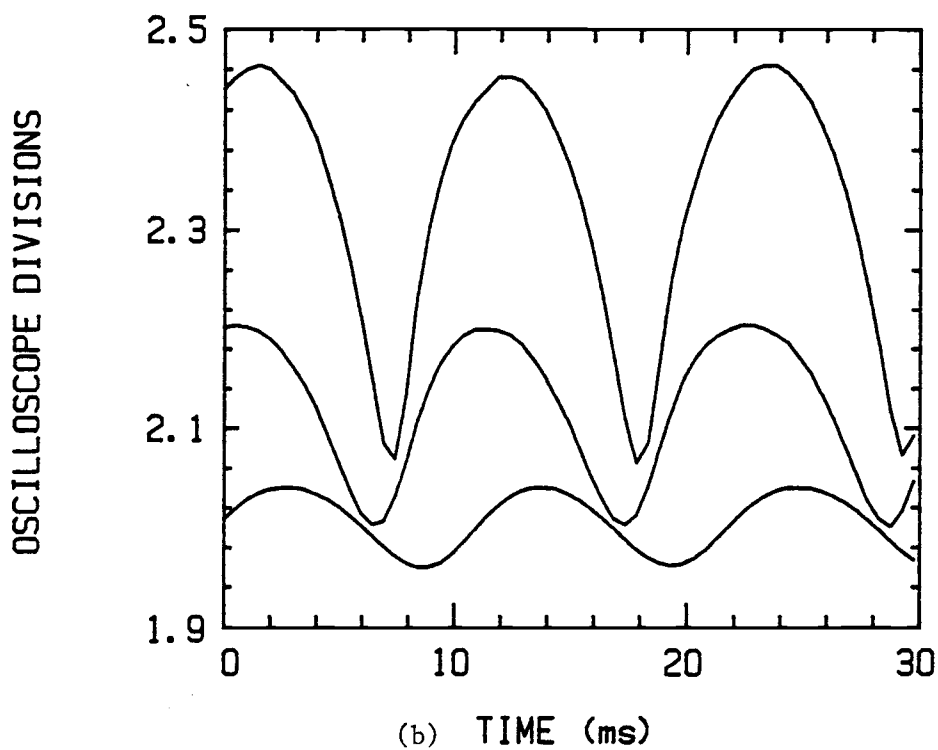
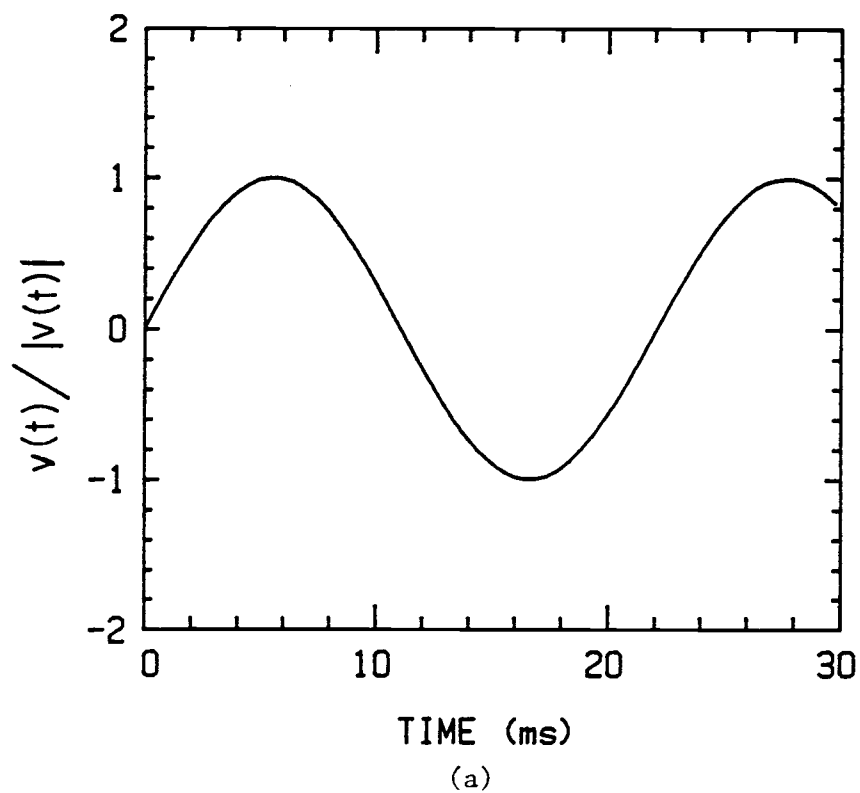


Fig. 3.1. (a) Velocity field to be measured, $v(t)/|v(t)| = \sin(\omega t)$ (b) corresponding bridge voltage for three values of velocity amplitude

ture. While the earlier studies [24,25] indicate that there is a difference obtained by dynamic calibration, more recent work has contradicted this finding [26,27]. No studies involving the measurement of a zero mean oscillating flow were found.

3.2 Analysis and Design of the Test Section

Consider the orifice backed cylinder, Fig. 3.2, driven by sinusoidal piston motion. Analysis is presented to establish the range of parameters such that the flow is incompressible within the cylinder and the velocity profile is relatively flat across the orifice. In this case a measurement of piston position, $s(t)$, can be used to determine the fluid velocity at the orifice center. Since the hot wire probe was located at the orifice center, this allowed a correlation between the anemometer bridge voltage and fluid velocity. In addition, as an independent check on the analysis, a method was developed to use measured pressure to calculate the error introduced by neglecting compressibility effects.

3.2.1 Design for Incompressible Flow

Assume that within the cylinder, Fig. 3.2, the following conditions are satisfied,

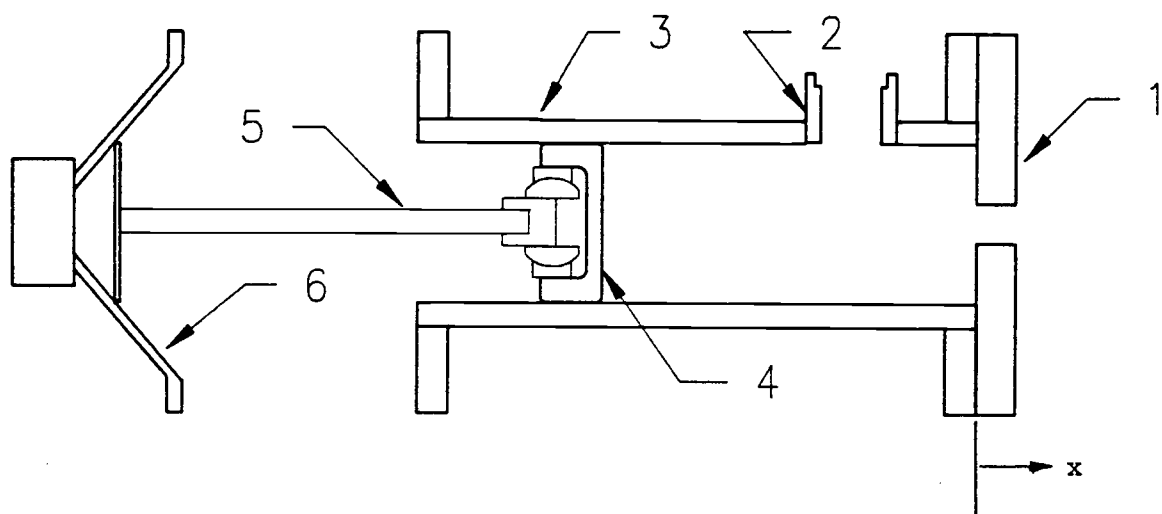
$$\begin{aligned} P' &\ll \beta \\ \rho' &\ll \rho \end{aligned} \tag{1}$$

Then if tube shear wave number is above ≈ 10 , viscosity effects may be neglected. In addition if the cylinder length and diameter are such that:

$$kL\sqrt{\left(\frac{\omega_c}{\omega}\right)^2 - 1} > 3.688 \tag{2}$$

where

$$\omega_c = 7.663c/D$$



- 1 ORIFICE PLATE
- 2 MICROPHONE FITTING
- 3 TUBE
- 4 PISTON
- 5 PISTON ROD
- 6 LOUDSPEAKER DRIVER

Fig. 3.2. Test section

the fluid velocity field will have no radial dependence; except in the near field of the orifice ($\approx 2-3$ orifice diameters). Since (2) holds for the analysis and data reported here, the velocity profile derived in Chapter 2 is valid:

$$V(x,t) = \omega s \frac{\left(\cos(kx) + i \frac{z_o}{Z} \sin(kx)\right)}{\left(\cos(kL) - i \frac{z_o}{Z} \sin(kL)\right)} e^{-i\omega t} \quad (3)$$

where $V(x,t)$ = fluid velocity in the cylinder, z_o is orifice impedance and Z is the characteristic impedance for the fluid in the cylinder.

Define α as the ratio of orifice volume velocity to piston swept volume. Piston swept volume is given by:

$$A\dot{s}(t) = A\omega s e^{-i\omega t} \quad (4)$$

Then, letting the orifice volume velocity equal $AV(x=0,t)$, and using (3) and (4), α may be written as:

$$\alpha = \frac{1-\Gamma}{e^{-ikL} - \Gamma e^{ikL}} \quad (5)$$

where

$$\Gamma = \frac{z_o/Z - 1}{z_o/Z + 1}$$

For incompressible flow, $\alpha = 1$. Compressibility effects cause α to become complex with a magnitude not equal to one. To design the test section, values of α were calculated as a function of t_o , d_o , v_o , D , L and ω . Values of z_o were taken from curve fits of the impedance data correlated by Panton and Goldman [28]. While this data is only correlated in the range of $t_o/d_o < 0.1$, it was adequate outside this range for the objective of this analysis. A typical set of design curves are shown in Fig. 3.3.

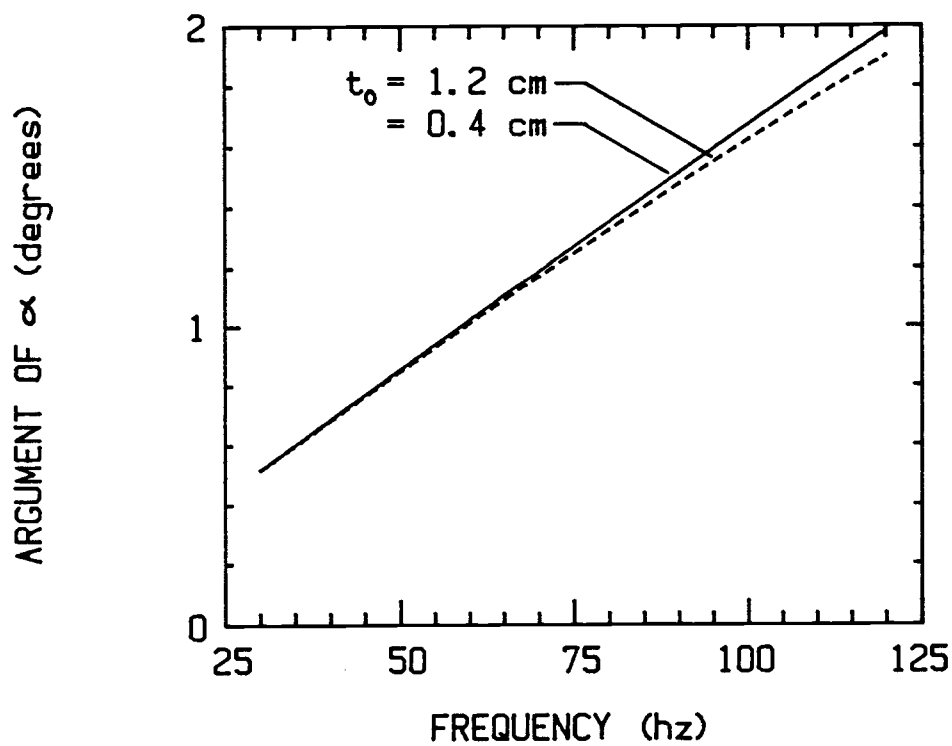
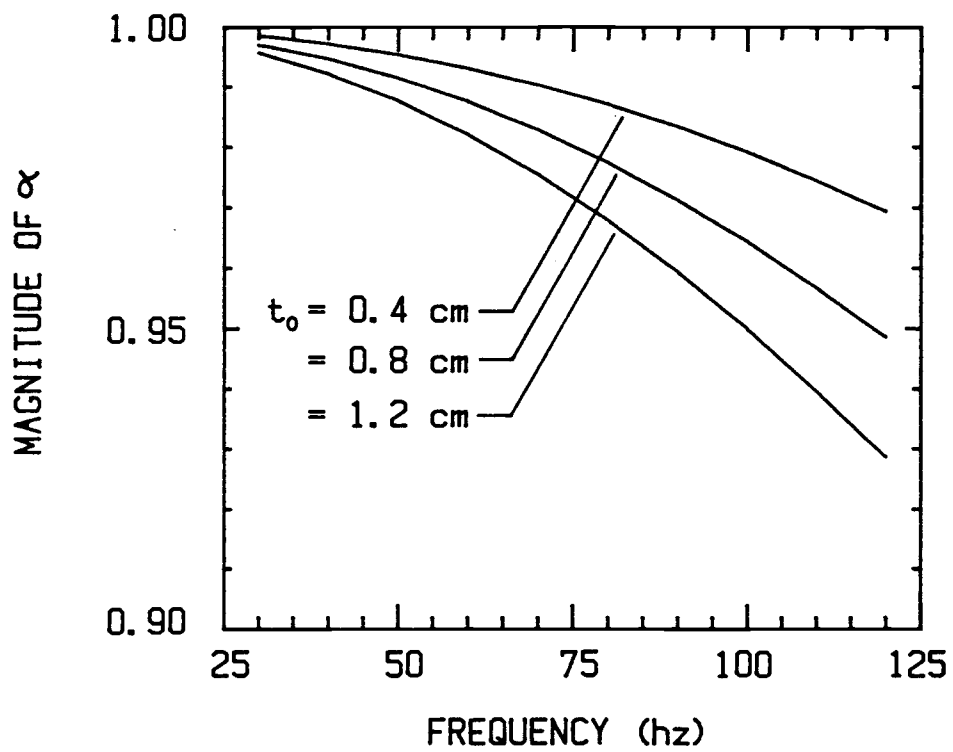


Fig. 3.3. Typical design curves to assess compressibility effects

3.2.2 Orifice Design

Using (5) it was possible to design the test section such that the compressibility error was below some specified value, say 2%. The idea of the orifice design was to produce a flat velocity profile across the orifice. In this case, the velocity at the hot wire probe location will be close to the average fluid velocity in the orifice. Using continuity and neglecting compressibility error, the velocity at the location of the hot wire probe can be written as:

$$v_c(t) = v_o(r=0, x=t_o/2, t) = \gamma \frac{A}{A_o} \omega s e^{-i\omega t} \quad (6)$$

where

$$\gamma \equiv \frac{v_o(r=0, x=t_o/2, t)}{v_o(t)} = \frac{v_c}{v_o} \quad (7)$$

where γ is a parameter indicating the "flatness" of the velocity profile, and $v_o(t)$ is a radially averaged velocity in the orifice.

The procedure followed was to design the orifice to yield $\gamma \approx 1$ but without introducing an unacceptable compressibility error. An estimation of γ was made in the following way.

If the orifice thickness is large enough, the problem has been solved and it can be shown that γ takes a value near one. Thus duct acoustics was used to determine the orifice thickness for which the long tube theory applies. This problem can be formulated using superposition as two problems of the form, solve:

$$\frac{\partial^2 \phi}{\partial t^2} - c^2 \nabla^2 \phi = 0$$

subject to:

$$\frac{\partial \phi}{\partial r}(r=0, x, t) = \frac{\partial \phi}{\partial x}(r, x=t_o, t) = \frac{\partial \phi}{\partial r}(r=r_o, x, t) = 0 \quad (8)$$

$$\frac{\partial \phi}{\partial x}(r, x=0, t) = f(r) e^{-i\omega t}$$

for the orifice given in Fig. 3.4. $v_o(x,r,t)$ may be recovered by evaluating the gradient of the velocity potential, $\phi(x,r,t)$. The solution to (8) is given in Chapter 2 as:

$$\phi(r,x,t) = \sum_{n=0}^{\infty} a_n J_0(k_{rn} r) \frac{\cos(k_{nx} (x - t_o))}{\sin(k_{nx} t_o)}$$

where:

$$a_n = \frac{\left[\int_0^{r_o} r f(r) J_0(k_{rn} r) dr \right]}{k_{xn} \left[\int_0^r r J_0^2(k_{rn} r) dr \right]} \quad (9)$$

$$k_{rn}^2 + k_{xn}^2 = k^2 = (\omega/c)^2$$

$$k_{rn} r_o = (0, 3.832, 7.016, \dots) \rightarrow J_0(k_{rn} r_o) = 0 \text{ for } n = (0, 1, 2, \dots)$$

For the case of $k_{rn} > k$; $k_{xo} = k$ and k_{xn} is imaginary. Thus let:

$$k_{xn} = ip_n \quad \text{for } n = 1, 2, \dots$$

where:

$$p_n \equiv \sqrt{k_{rn}^2 - k^2} \quad (10)$$

Using (10) and expanding (9) yields:

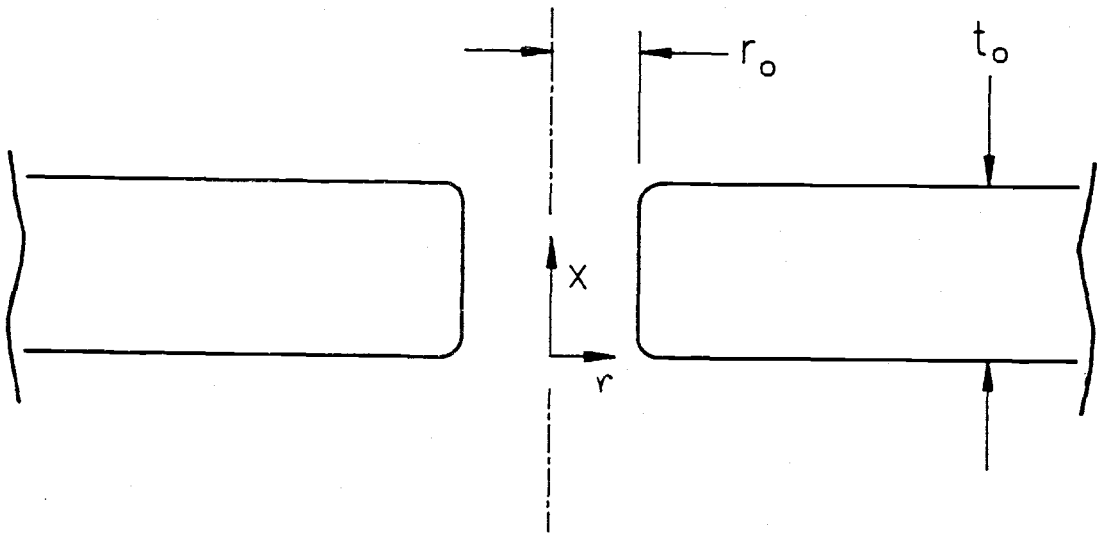


Fig. 3.4. Orifice geometry

$$\begin{aligned} \phi(r,x,t) = & \frac{\bar{f}}{k} \frac{\cos k(x-t_o)}{\sin(kt_o)} - ia_1 J_o(3.83r/r_o) \frac{\cosh(p_1(x-t_o))}{\sinh(p_1 t_o)} \quad (11) \\ & - ia_2 J_o(7.02 r/r_o) \frac{\cosh(p_2(x-t_o))}{\sinh(p_2 t_o)} - \dots \end{aligned}$$

where \bar{f} = radially averaged value of $f(r)$.

In (11), the $n = 0$ term has no radial dependence and the $n > 0$ terms drop off exponentially with x . Since the $n = 1$ term drops the most slowly, when it has vanished there will be no radial dependence. From (11) the magnitude of the $n=1$ term at the orifice midplane divided by its magnitude at the orifice inlet may be calculated:

$$\frac{\phi(r,x=t_o/2,t)_{n=1}}{\phi(r,x=0,t)_{n=1}} \frac{\cosh(p_1 t_o/2)}{\cosh(p_1 t_o)} \approx e^{-p_1 t_o/2} \quad (12)$$

As an example, using orifice geometry values from the final design in (12), yields a value of 0.022. Equal contributions of 0.022 from both sides of the orifice are assumed (i.e., superposition). Then, it can be estimated that the terms with radial dependence at the inlet/exit of the orifice have dropped in magnitude by greater than 95% by the axial midplane of the orifice. Now, the long tube theory velocity profile can be used to determine γ . From Tijdeman [29], this velocity profile is:

$$v_o(r,x,t) = g(x,\Gamma')(1 - \frac{J_o(i^{3/2} S_o r/r_o)}{J_o(i^{3/2} S_o)}) e^{-i\omega t} \quad (13)$$

where $g(\Gamma',x)$ is given in [29] and S_o is the shear wave number for the orifice. Radially averaging (13) and using (7) leads to:

$$\gamma = \frac{J_0(i^{3/2}S_0) - 1}{J_0(i^{3/2}S_0) + \frac{\sqrt{2}}{S_0} (1+i)J_1(i^{3/2}S_0)} \quad (14)$$

Values of γ from (14) are presented on Fig. 3.5. Velocity profiles from (13) are presented on Fig. 3.6. It is seen that long tube theory applied to an orifice indicates that above $S_0 \approx 10$ the velocity profile is relatively flat across the orifice.

3.2.3 An Experimental Check

The objective of this section is to derive a method to experimentally estimate the compressibility error without relying on the §3.2.1 analysis. Because $kL \ll \pi$ within the test section, density did not depend on axial position, $\rho'(x,t) = \rho'(t)$. Applying conservation of mass to a control volume consisting of the interior of the test section, Fig. 3.2, yields:

$$(L + s(t)) A \frac{d\rho'(t)}{dt} + \rho v_o(t) A_o - \rho \dot{s}(t) A = 0 \quad (15)$$

To eliminate $\rho'(t)$ in favor of $P'(t)$, which is measurable, an equation of state with an isentropic assumption was used:

$$\frac{d\rho'(t)}{dt} = \frac{1}{c} \frac{dP'(t)}{dt} \quad (16)$$

Combining (15) and (16) yields:

$$v_o(t) = \frac{A}{A_o} \dot{s}(t) (1 - \epsilon(t)) \quad (17)$$

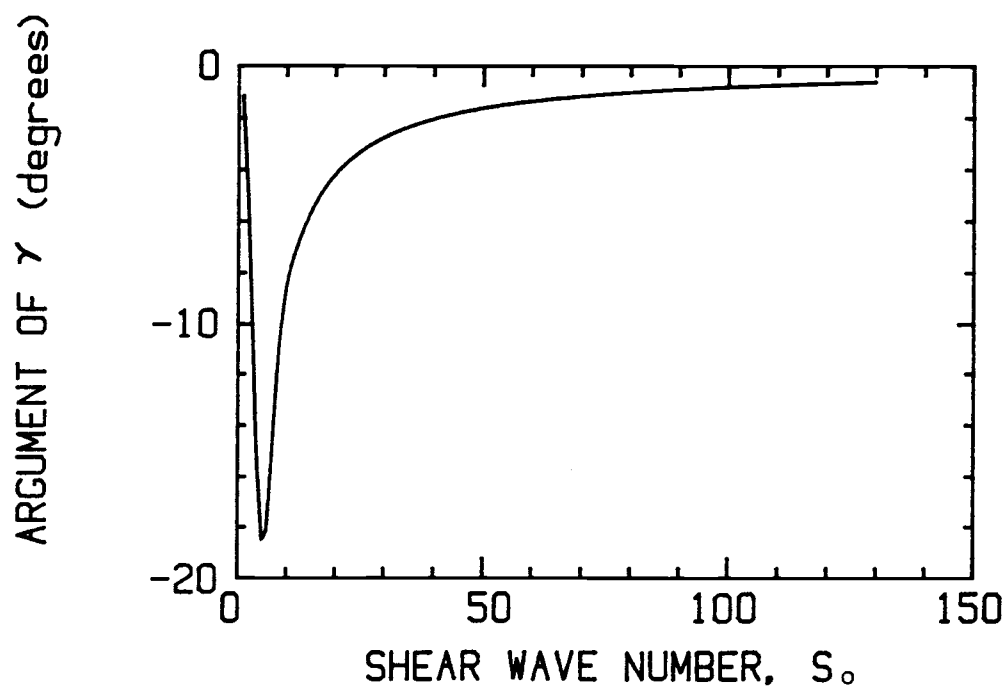
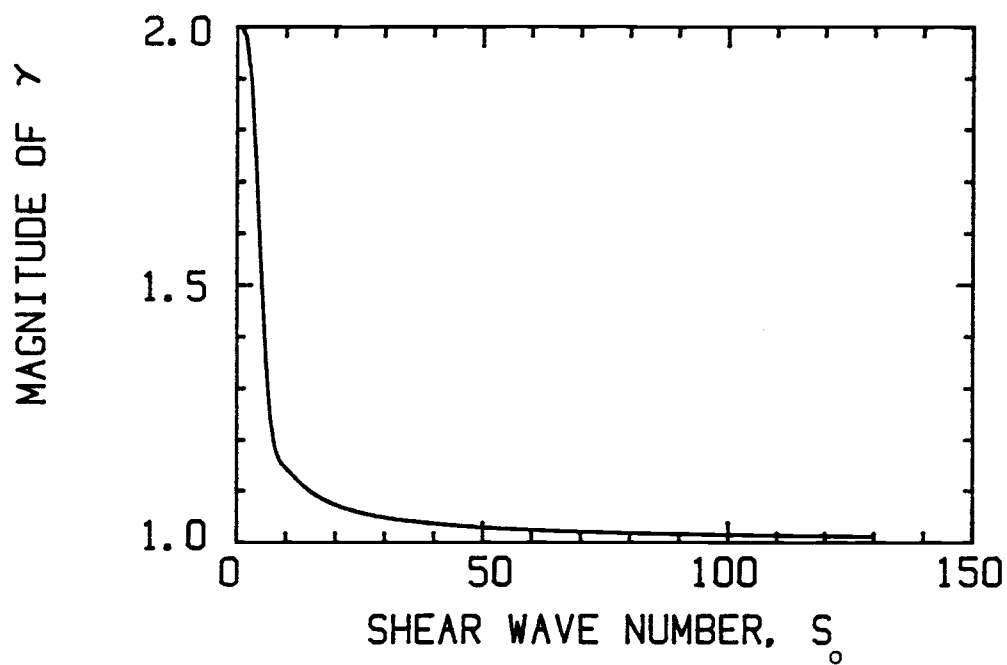


Fig. 3.5. Magnitude and argument of γ as a function of shear wave number, S_0

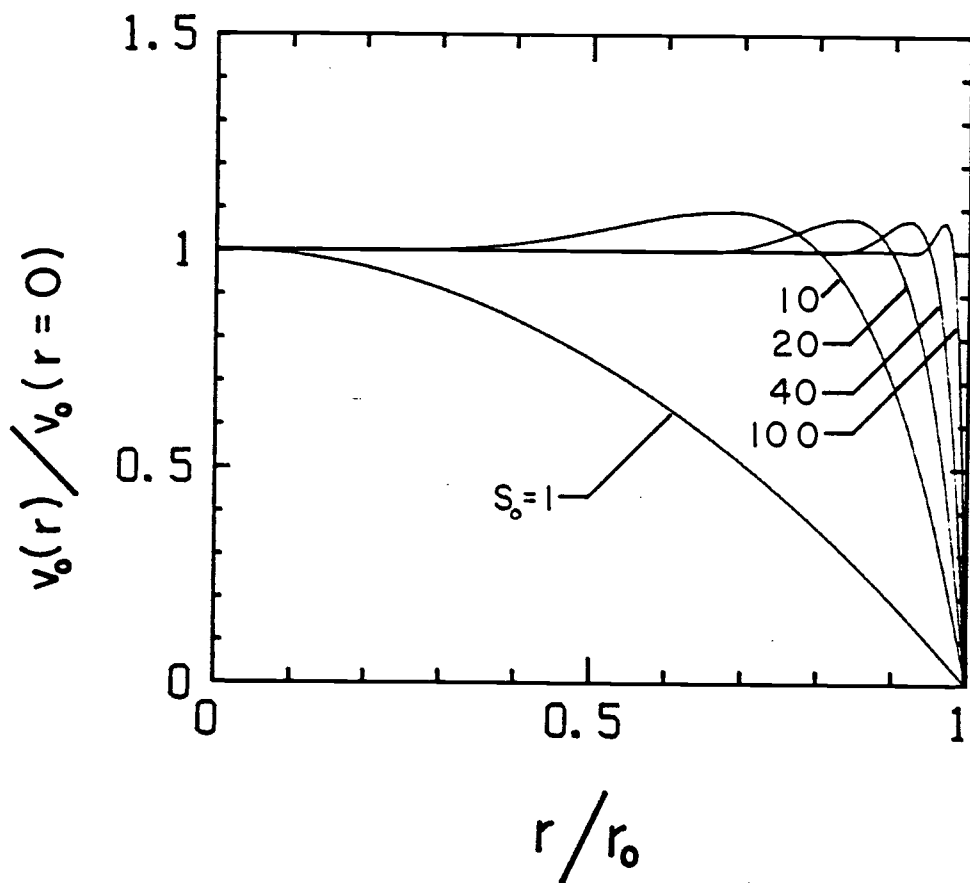


Fig. 3.6. Axial velocity profiles as a function of radius for four values of shear wave number, S_0

where

$$\epsilon = \frac{L+s(t)}{\rho c^2} \frac{dP'(t)/dt}{ds(t)/dt}$$

where $\epsilon \equiv$ compressibility error, was estimated using typical data, Fig. 3.7a, as:

$$\epsilon \approx \frac{LP'}{s\rho c^2} \quad (18)$$

Equation (18) was used to experimentally estimate the error introduced by neglecting fluid compressibility.

3.3 Experimental Apparatus and Procedures

The test section which was oriented vertically is shown in Fig. 3.2. An orifice with a 0.79 cm diameter and a 0.79 thickness was used. The cylinder was fabricated from mild steel with a honed inside diameter of 3.15 cm and a wall thickness of 0.46 cm. The effective tube length which is variable up to 15.8 cm was fixed at 7.5 cm.

A brass piston with a machined outside diameter $\approx 25 \mu\text{m}$ less than that of the cylinder, was used. A piston length of 1.27 cm was used to provide accurate alignment. The piston was connected to the piston rod with a Aurora spherical bearing which solved the problem of aligning the piston with the driver. The piston was driven by mechanically coupling the piston to the paper cone of an 20 cm woofer-type loudspeaker. A sine wave output from a Tektronix FG 501A function generator was amplified with a Dynaco mono amplifier to power the speaker.

Pressure seal in the test section was achieved by using vacuum pump oil between the piston and tube walls; and O-rings around the microphone and under the orifice plate. It was estimated that the measured leak rate contributed an error of less than 0.004%.

Piston position was measured with a Bently Nevada 7200 series proximity transducer which has an operating range to 10 khz. Cali-

bration was performed with a micrometer which has a 2.5 μm smallest division.

Pressure was measured with a 1.3 cm GenRad measuring microphone. Calibration was performed with a GenRad 1986 sound level calibrator which has a stated accuracy of ± 0.35 dB re 20 μPa .

The hot wire probe, TSI 1210-T1.5, consisted of a 3.8 μm diameter platinum coated tungsten wire with an active sensing length of 1.27 mm and a total wire length of 1.52 mm. The anemometer bridge circuit used was a TSI 1050 and 2 VDC were subtracted from the signal with a TSI 1057 signal conditioner. No filtering was performed. The probe was operated at 250°C and the system frequency response was estimated to be 102 khz.

Positioning the the hot wire probe was performed with a three axis Velmex unislide assembly, which has a stated accuracy of ± 125 $\mu\text{m}/\text{m}$. The method used for referencing the hot wire probe was to "eyeball" the probe to the center of the orifice flush with the top surface. Scribed lines in the orifice plate helped to insure accurate reference and alignment. The estimated error in absolute position is ± 175 μm . In view of the flatness of the velocity profiles in the orifice, Fig. 3.6, very accurate positioning was not required.

Static calibration of the hot wire probe was performed using a TSI 1125 calibrator. The stated calibrator accuracy is $\pm 2\%$ for velocities from 3 to 300 m/s, $\pm 5\%$ for velocities from 0.15 to 3 m/s and $\pm 10\%$ for velocities below 0.15 m/s.

Frequency measurements were performed with a Tektronix DC 503A counter.

The data acquisition system consisted of a Tektronix 7D20 digitizer interfaced via a GPIB to an IBM PC. All voltage signals were averaged over ≈ 250 cycles to remove random noise in pressure, position and velocity and fluctuations (due to flow instabilities and turbulence) in the velocity channel. This averaging greatly improved the repeatability of the data and also made it possible to record data at very low amplitudes. Observations of the unaveraged waveforms indicated that the averaging did not remove any significant amount of information. Voltage and time measurements were recorded

off the digitizer using cursors, with the PC functioning as a data storage and display system.

3.4 Experimental Data

The dynamic calibration consisted of (i) measuring piston position, $s(t)$, and using (6) and (14) to calculate known velocity passing by the hot wire, (ii) measuring anemometer bridge voltage and relating this voltage to the known velocity and (iii) measuring $P'(t)$ and using (18) to estimate the error in (6) from neglecting fluid compressibility.

Four typical sets of measured waveforms are shown in Fig. 3.7. Each set contains an oscilloscope trace of piston position, $s(t)$, pressure $P'(t)$, and anemometer bridge voltage, $U(t)$. Points A, B, E, and F are where amplitude and time information were recorded. Points A and C correspond to the maximum positive (+x direction) and negative (-x direction) flow velocities out the orifice, respectively. Points B and D correspond to flow reversals.

The data in Fig. 3.7 span the range of the variables measured and illustrate qualitative information about the experiment. In Fig. 3.7a, note that the point A is slightly higher than point C; and in Fig. 3.7b the same effect occurs at the points of flow reversal. One possible cause is that the outflow velocity is less than the inflow velocity at the probe location. It has also been noted that the effect seems to occur in a much more pronounced fashion when a cylindrical hot film probe (which has a much larger diameter) was used and thus could be due to a heat transfer phenomena.

In Figs. 7a and 7b, the pressure data is quite harmonic except for a little ripple. The ripple is introduced by the piston driver and is correlated with friction between the piston and the tube walls. Friction causes the piston driver to deviate slightly from a monochromatic motion and the frequency content at the Helmholtz natural frequency of the test section shows up as the ripple in the pressure signal.

In Figs. 7c and 7d, the pressure data clearly shows the presence of nonlinearities. This is very significant because the design pro-

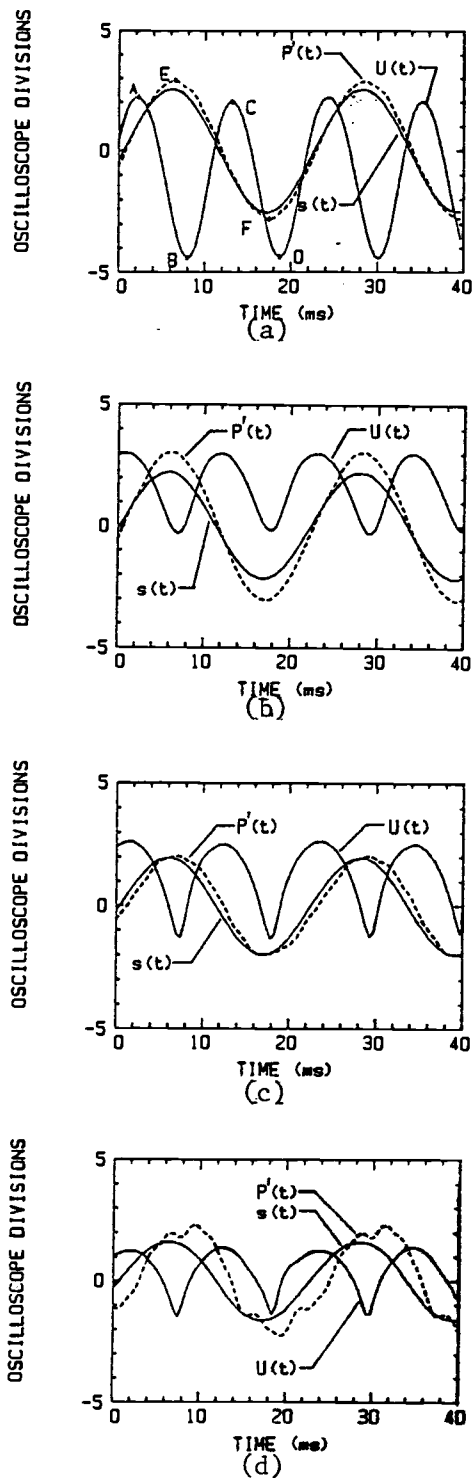


Fig. 3.7. Typical waveforms at 45 hz ($S_o = 16.7$); these curves correspond to known orifice velocities of (a) 0.29 m/s, (b) 0.63 m/s, (c) 2.24 m/s, and (d) 4.57 m/s

cedures used linear acoustic theory and hence the applicability to these cases is in question. However, the method for checking on the theory, §3.2.3, is valid in any case. Use of numbers from (18) indicated that (6) was reasonable for all cases.

In Figs. 7a-7c, the bridge voltage trace appears approximately as an rectified sine wave (actually as a rectified sine wave squared). In 7d, a characteristic flat top wave is appearing, which becomes more pronounced at higher velocity amplitudes.

Ideally, the calibration would result in a correlation for instantaneous bridge voltage as a function of instantaneous velocity. For a number of reasons, especially related to the degree of uncertainty associated with this procedure, this was not done. Instead, relationships were found between (a) the peak flow velocity, v_c , and the peak bridge voltage (b) v_c and the bridge voltage corresponding to flow reversal and (c) v_c and the bridge voltage phase lag behind the fluid velocity.

Figure 3.8 shows peak bridge voltage as a function of v_c . At low velocities, the agreement is very good and as velocity increases, the dynamic calibration curves are slightly higher than the static calibration curve. The uncertainty of the data points at the higher velocities is greater than those at the lower velocities due to compressibility effects and higher harmonics appearing in the bridge voltage (Fig. 3.7d); consequently the slight trend cannot be justified with a high degree of certainty. It is concluded that the static calibration curve correctly predicts the peak velocity magnitude with an estimated uncertainty of $\pm 10\%$.

Figure 3.9 shows minimum bridge voltage as a function of v_c . Clearly this indicates that the static calibration results are not valid in interpreting the velocities around the points of flow reversal.

Figure 3.10 shows the phase lag of the bridge voltage behind fluid velocity as a function of v_c . Figure 3.10a is the phase lag of the maximum bridge voltage from the maximum fluid velocity. Figure 3.10b is phase lag of the minimum bridge voltage behind the flow reversal point.

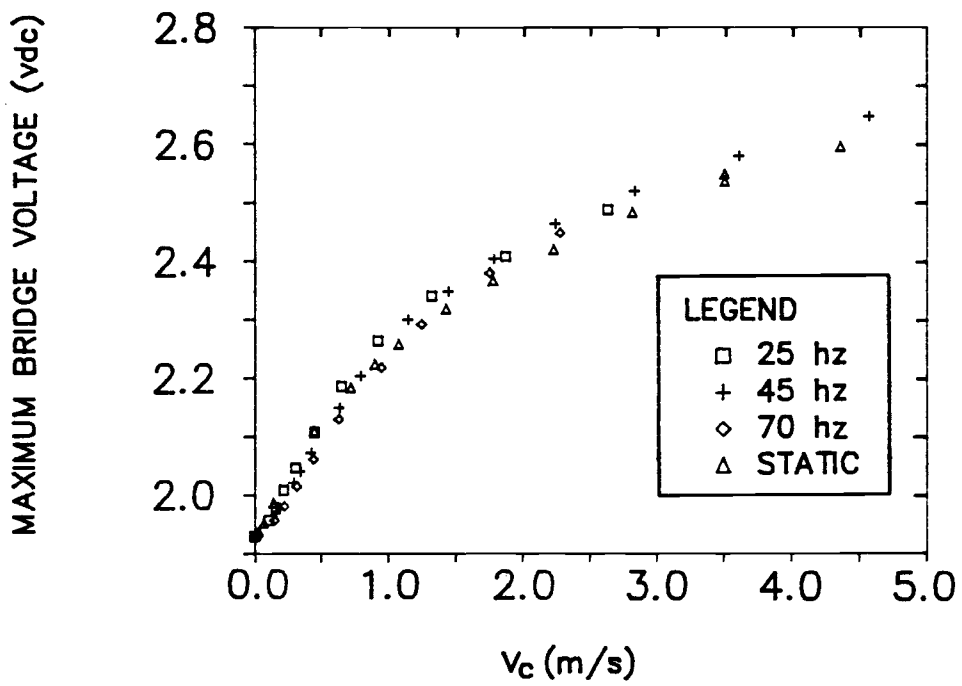


Fig. 3.8. Maximum bridge voltage as a function of v_c

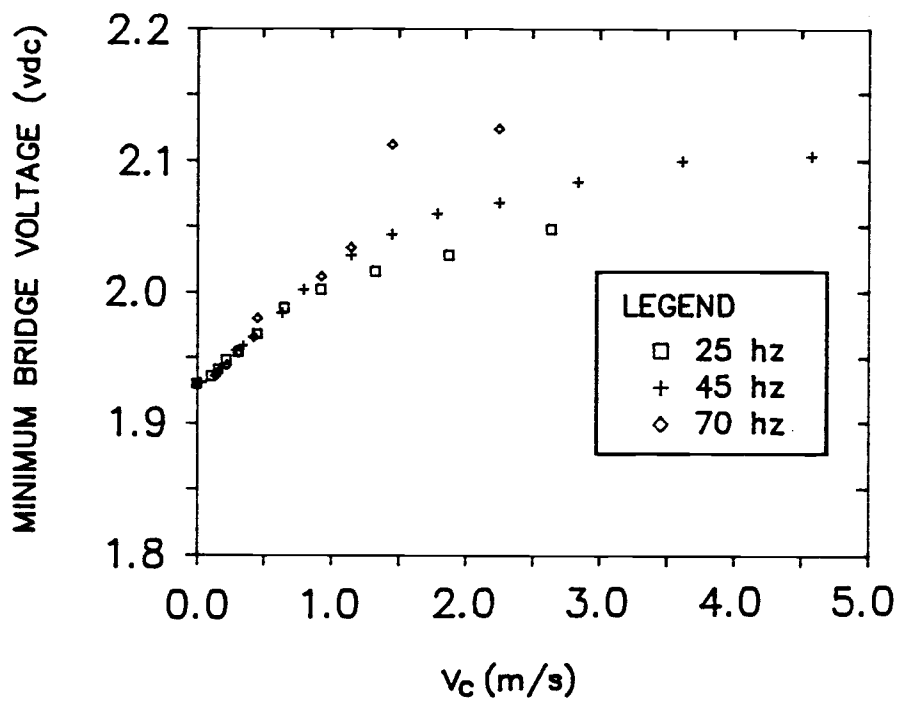


Fig. 3.9. Minimum bridge voltage as a function of v_c

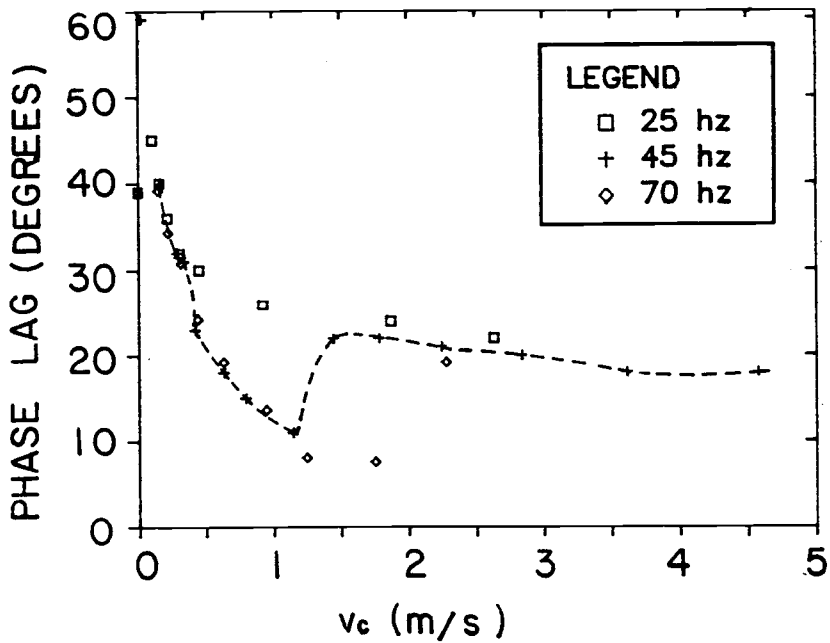
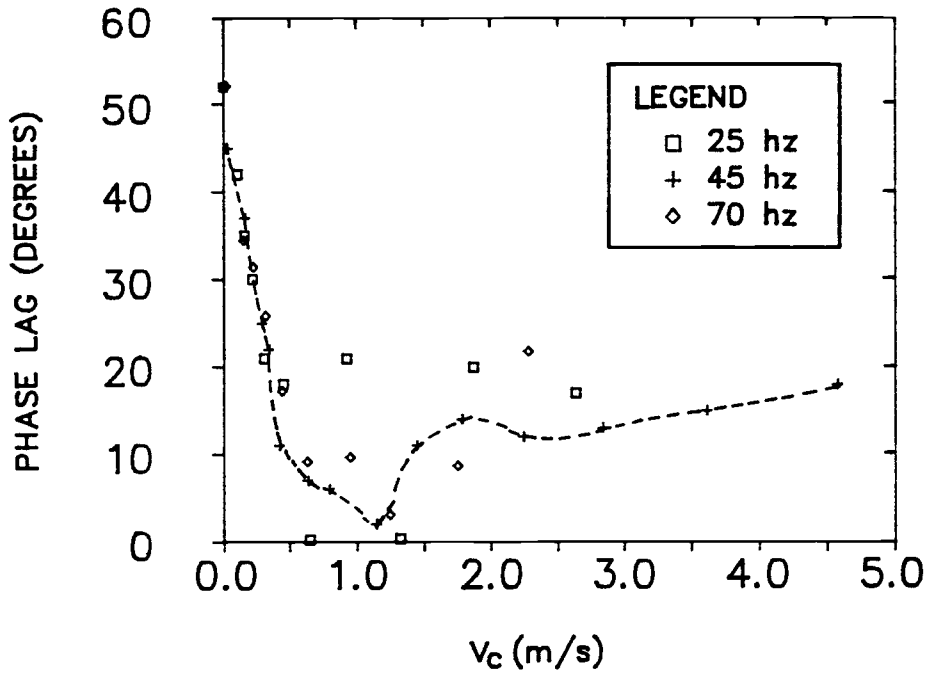


Fig. 3.10. Phase lag of bridge voltage behind flow velocity as a function of v_c

(a) Phase lag of maximum bridge voltage

(b) Phase lag of minimum bridge voltage

The phase lag is difficult to assess due to the nonlinear relationship between velocity and bridge voltage. Hence, while the trends in Fig. 3.10 are valid, predictions based on the curves will have a high degree of uncertainty; estimated to be $\pm 20\%$. The characteristic dip in the phase lag is somewhat puzzling and was not explained. At this point Reynold's number based on wire diameter and average velocity ≈ 0.2 .

Finally, two checks were made on the analysis. Using (18), the maximum errors introduced by neglecting compressibility are 0.55%, 1.6%, and 4.8% at 25, 45, and 70 hz, respectively. Velocity profiles across the orifice were measured using the hot wire anemometer and the profile was compared with the theoretical result from (13). The results, Fig. 3.11, show that the trends of (13) are reasonably matched. Because of the difficulty in getting close to the wall, data for $r/r_0 > 0.8$ were not obtained.

3.5 Discussion

To understand the dynamic calibration results several explanations were examined. First, the anemometer system response was examined to see if a frequency response problem would explain the observed behavior. The theory and analysis of anemometer system response for small oscillations about a mean value has been worked out in an excellent series of papers by Freymuth; see for example [30,31]. One could follow these methods and solve the problem for oscillations about a mean value of zero. However, observations of the bridge voltages while introducing a sine wave across the bridge to simulate an oscillating flow did not produce comparable results to the dynamic calibration. In addition, the sinusoidal shape of the bridge voltage would seem to be contradictory to a frequency response problem.

The second possible explanation is that differences between the heat transfer process in the static and dynamic cases are responsible for the observed behavior. There have been a number of heat transfer studies for a wire oscillating in a still fluid. It would be expected that the heat transfer in this case would be similar to that

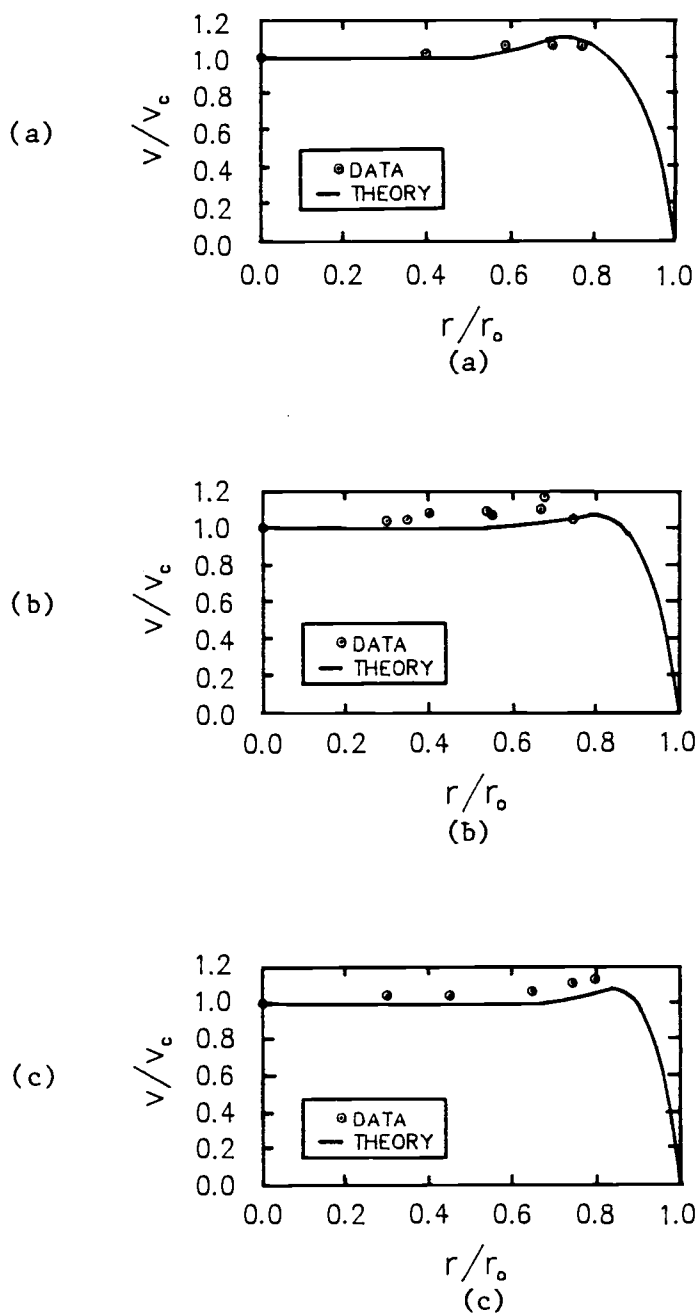


Fig. 3.11. Theoretical and measured radial velocity profiles across orifice

(a) $S_o = 12.5$, $f = 25$ hz

(b) $S_o = 16.75$, $f = 45$ hz

(c) $S_o = 20.87$, $f = 70$ hz

of sinusoidal flow past a still wire. Most of the results have been presented as a temporally averaged Nusselt number; see Mabuchi and Tanaka [32], for example. Curves for $Nu(t)$ are presented for several cases by Thrasher and Schaeltzle [33] and Carr and Black [34]. No correlations for $Nu(t)$ were found. Qualitatively the $Nu(t)$ curves agree with the dynamic calibration results in the following ways: (a) the minimum $Nu(t)$ is above that of the pure natural convection case, (b) the minimum and maximum $Nu(t)$ lags the minimum and maximum velocity and (c) $Nu(t)$ has a sinusoidal shape.

Thus, some physical interpretation of the dynamic calibration results may be made. During a static calibration the voltage corresponding to a zero value of fluid velocity is determined by a steady natural convection heat transfer phenomena. In the dynamic case, the corresponding zero velocity heat transfer is higher, indicating that there is less overall thermal resistance. This would be explained by a decreased boundary layer thickness in the dynamic case. In the dynamic case, the increase in heat transfer at the flow reversal point at velocity magnitude, v_c , increases would support the idea that oscillating flow tends to "sweep away" the boundary layer and hence lower the overall thermal resistance.

As fluid velocity over a hot wire probe is increased from zero, the heat transfer moves from a pure natural convection regime at zero velocity through a mixed natural/forced convection regime to a pure forced convection regime. Thus, the agreement of the static and dynamic calibration results at peak velocity amplitude would suggest a pure forced convection heat transfer phenomena. Furthermore, the agreement in heat transfer would indicate that the fluid dynamics in the wire near field for the static and dynamics cases are similar.

3.6 Conclusions

A method for designing a test section to produce a sinusoidal velocity field of known magnitude has been presented. A test section based on this analysis was fabricated and used for the dynamic calibration of a constant temperature hot wire anemometer probe. The calibration results indicate that static calibration results are

valid to relate the maximum bridge voltage to velocity. Dynamic calibration is necessary to (i) interpret the voltages around the point of flow reversal and (ii) establish the phase lag of the bridge voltage behind the velocity. The calibration results are in qualitative agreement with a conclusion that the effects observed are due to a different heat transfer phenomena in the dynamic case as compared to the static case.

CHAPTER 4
A STUDY OF OSCILLATING FLUID FLOW THROUGH
TWO ORIFICES IN SERIES

4.1 Introduction

Consider two round orifices in series, Fig. 4.1, subjected to an oscillating zero mean flow at the inlet of the first orifice. The objective of this study was to characterize the fluid dynamics of this problem. It was motivated by a need for design information for the nozzle area of a drop-on-demand ink-jet printhead. However, it should be mentioned that the approach and results were performed with general applications in mind.

The idea of using a two orifice nozzle for an ink-jet printhead was first proposed by Stemme and Larsson [35]. An example of an ink-jet printhead using this nozzle configuration is shown in Fig. 4.2. The fluid is a water based ink and the structure is steel. An input voltage, Fig. 4.3a applied to the PZT biomorph*, leads to the ejection of a single drop of ink out the plate 2 orifice. Ink refills from a reservoir which feeds ink between plates 1 and 2. A typical voltage signal to create three drops is shown in Fig. 4.3b. Because of the on/off nature of printing, the time between pulses is not uniform.

The relationship of the problem studied and the modeling of an ink-jet printhead is discussed in Chapter 2. The relevant conclusions are as follows. (1) The physics of the Fig. 4.1 problem, which does not have a drop development boundary condition (BC), are closely related to the physics important in the nozzle area of an ink-jet printhead. (2) With the exception of the nozzle area, the printhead fluid dynamics can be formulated using classical methods. The nozzle may be treated as a BC for the solution of the governing equations within the horn region of the ink-jet printhead. Determining values of this BC is the primary objective of this work. (3) Studying the

*The PZT biomorph is a piezoelectric crystal bonded to a steel plate.

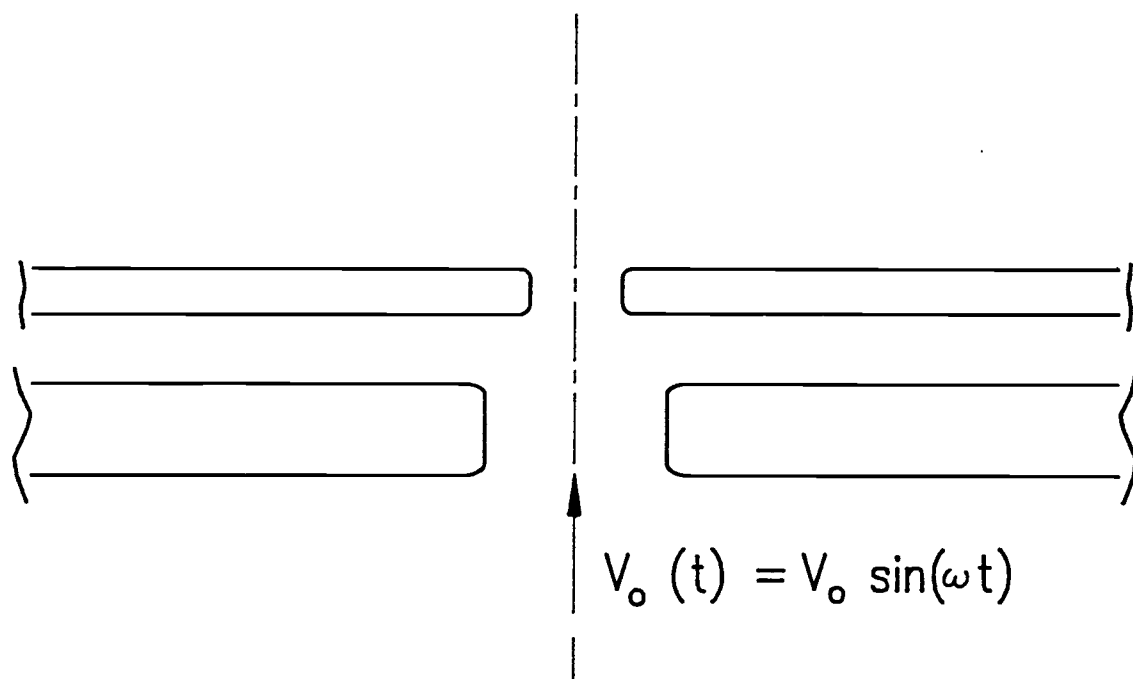


Fig. 4.1. Oscillation flow through two orifices in series

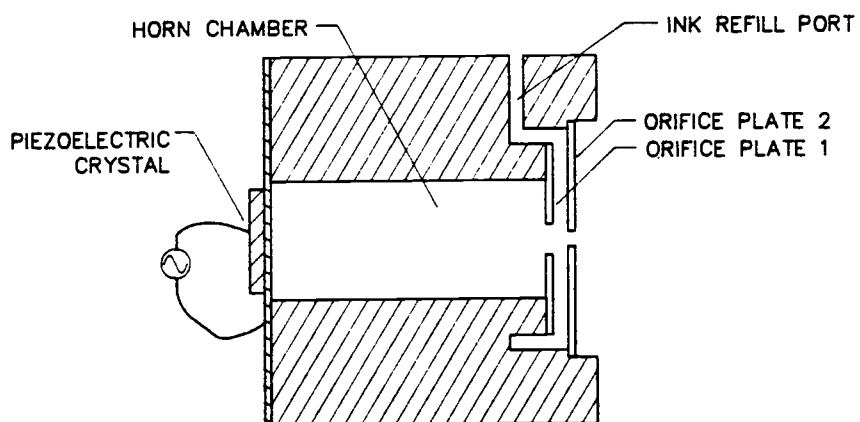


Fig. 4.2. A simplified ink-jet printhead

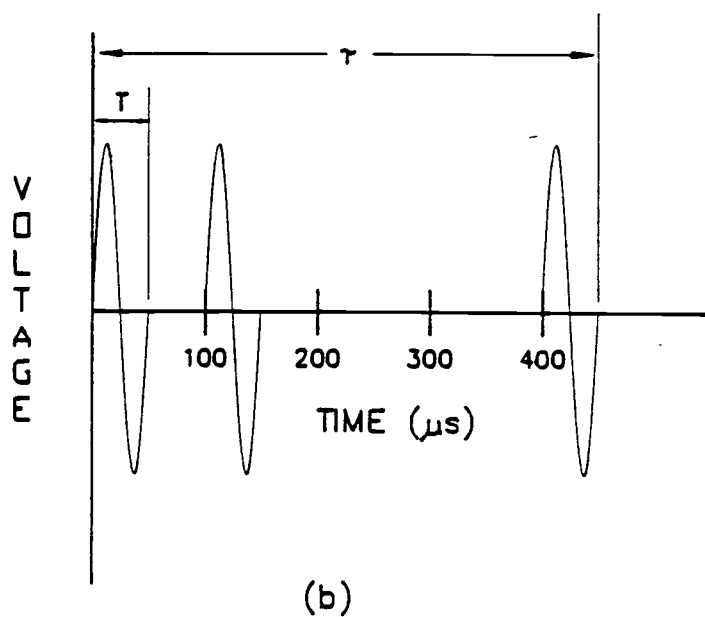
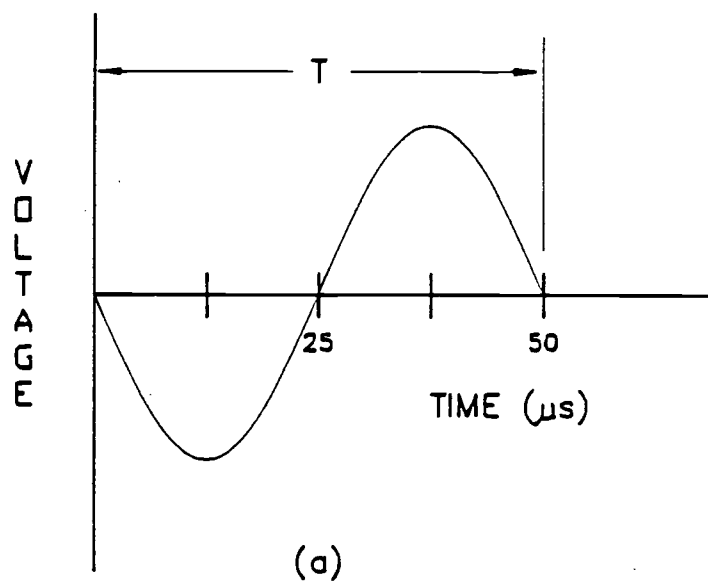


Fig. 4.3. Input voltage signal to produce
(a) one ink drop
(b) three ink drops

case of monochromatic input, as opposed to that shown in Fig. 4.2, will yield the most general information.

The specific objectives of this study were to: (i) determine a set of independent dimensionless groups governing the fluid dynamics of oscillating flow for the geometry shown in Fig. 4.1, (ii) to define a set of dependent parameters of interest and to develop methods for measuring these parameters, and (iii) to describe the fluid dynamics by correlating the experimental data.

While no literature was found about oscillating flow through two orifice, the problem of oscillating zero mean flow through a single orifice has been studied extensively [36-43]. The fluid dynamics for single orifice flow are characterized by an orifice impedance, z_o , defined as:

$$z_o = \frac{P_1'(t) - P_2'(t)}{A_o v_o(t)} \quad (1)$$

for the geometry shown in Fig. 4.4; where $P_1'(t)$ is monochromatic incident pressure written in complex form, $P_2'(t)$ is the monochromatic component of the transmitted pressure written in complex form and $v_o(t)$ is the monochromatic component of the fluid velocity at the orifice written in complex form. Impedance relates the pressure drop across the orifice to the volume flow rate through the orifice; with the physical variables written as complex quantities to carry phase information. Since, all the parameters in the definition are monochromatic at the same frequency, z_o does not depend on time. Values of z_o are typically presented as:

$$z_o = \frac{R - iX}{A_o} = \frac{1}{A_o} [R - i\rho\omega(t_o + \delta)] \quad (2)$$

where R is the resistance, X is the reactance and δ is an added mass term. The damping and mass characteristics of the fluid in the orifice are embodied in R and X , respectively.

While the form of (2) has a theoretical basis, empirical data for R and δ is required. A discussion of the physical interpretation

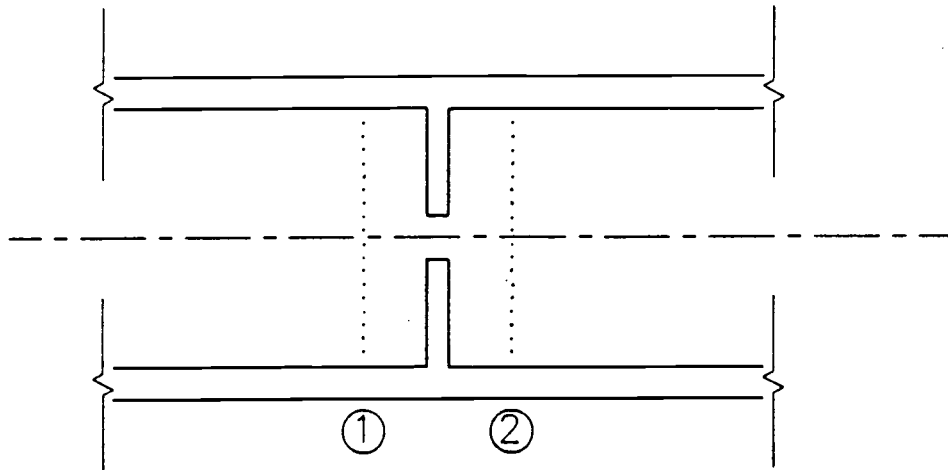


Fig. 4.4. Geometry for orifice impedance definition

of z_0 is presented in Chapter 2 and measurement methods will be reviewed here.

The first class of measurement methods involves direct measurement of $P'(t)$ and $v_0(t)$ and substitution into (1). Because $v_0(t)$ is quite difficult to measure, these methods have limited applicability. Thurston et al. [39,40] used water and silicone oil at low frequencies and small length scales in a piston driven test section. Thus, $v_0(t)$ was determined by measuring piston displacement and using continuity.

Ingard and Ising [38] used a constant temperature hot wire anemometer to measure $v_0(t)$. They reported that this method was limited to fairly large velocity amplitudes and that the determination of phase information was not particularly good. The suitability of the hot wire for measurement of reversing flows and the reasons why it was not accurate at low velocities were not addressed.

Consider a closed cavity excited by a vibrating boundary (ex. piston or loudspeaker) and having an orifice in the middle or at one end. Standing pressure waves will form in the cavity and the standing wave pattern will be influenced by the presence of the orifice. The second class of measurements methods involves measurements of the standing wave field within the closed cavity to calculate orifice parameters. While there is a lot of variation in how and where data is recorded, all of the methods are indirect in the sense of requiring analysis to relate the measured variables to $v_0(t)$ and z_0 .

The most common of the standing wave methods involves the use of the precision impedance tube [36,41,42], a long cylinder with the orifice at one end. A pressure field is set up within the tube and a microphone is traversed along the tube center line to record the standing wave field.

Measurements at the resonant frequency of a Helmholtz resonator have been used to measure z_0 for the orifice forming the neck of the resonator [38,43]. The value of the Helmholtz natural frequency is used to predict the imaginary part of z_0 and the width of the resonance peak is used to predict the real part of z_0 . This method is

best suited for measurements when z_0 is small (i.e. in or near the linear region).

A third standing wave method involves the placement of the orifice in the center of a tube [38,43]. Measurements of the pressure at fixed locations in the cavities on either side of the orifice are used to find z_0 .

Panton and Goldman [37] used a piston driven cylinder with the orifice opposite the piston end. Measurements of piston acceleration and pressure at a fixed point within the cylinder were used to find z_0 .

4.2 Dimensional Analysis

Dimensional analysis was used to reduce the number of independent variables and to scale the experiment to yield parameters which were both measurable and characteristic of ink-jet printheads.

Significant length scales are defined on Fig. 4.5. The remaining independent variables are fluid properties, ρ , μ , β ; time scale, ω , and pressure drop across the two orifices, P' . P' was selected instead of v_0 because it is much easier to control during experimental work.

Nine dimensionless groups were formed and they are presented in Table 4.1 along with typical values for an ink-jet printhead. With the exception of $P'/\rho\omega\nu$ and S_t , the groups are familiar. $P'/\rho\omega\nu$ is defined so that $(P'/\rho\omega\nu)/(\nu_0/\sqrt{\omega\nu})^2 = P'/\rho\nu_0^2$; where $\nu_0/\sqrt{\omega\nu}$ is the characteristic dimensionless velocity for single orifice flow [28]. S_t , the shear wave number, is proportional to the ratio of plate spacing to boundary layer thickness.

4.3 Problem Formulation

The number of dimensionless groups to be considered was reduced from 9 to 6 by fixing $t_1/d_1 = 0.5$, $t_2/d_2 = 0.5$ and $kD = 0.28$. t_1/d_1 and t_2/d_2 were fixed because it did not seem likely that values much different than 0.5 would be used in a printhead. kD was fixed because the test section characteristics did not allow this parameter to be varied during the experimental work. In addition, the dimen-

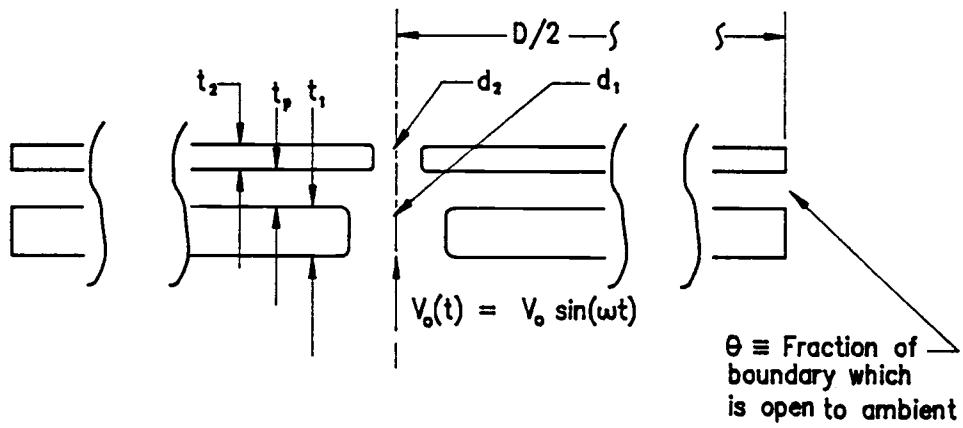


Fig. 4.5. Double orifice geometry showing important variables

Table 4.1. Dimensionless groups.

Group	Description	Typical Ink-Jet Printhead Value
t_p/d_1	-	2.6
d_1/d_2	-	0.6
D/d_1	-	38
t_1/d_1	-	0.5
t_2/d_2	-	0.8
θ	Fraction of boundary between two plates open to ambient	≈ 1
$p'/\rho\omega v$	-	800
$t_p\sqrt{\omega/\nu}$	S_t - shear wave number	70
kD	-	0.25

sionless groups S_t and D/d_1 were not controlled during the experiment. The reasons for this were that: (i) the effects of these variables was thought to be insignificant within the range of parameters considered and (ii) in the experiment it was only possible to control four independent dimensional variables and, thus four dimensionless groups could be fixed and the other two would float.

The dependent variables (variables to be measured) were chosen to be $R/\rho\sqrt{\omega\nu}$, $\delta/0.85d_1$, v_2/v_0 , and P'_2/P' . This choice was based on both the use of R and δ to characterize the single orifice problem and on the relative importance of R , δ , P'_2 , and v_2 to the printhead designer. The key parameter required to design and model the horn section of an ink-jet printhead is the nozzle impedance, z_0 , which is specified by the values of R and δ via (2). In the single orifice case, z_0 should also give enough information for the nozzle design. In the double orifice case, it will not provide the required information. Thus, the two additional dependent variables were specified. The problem to be studied was formulated as:

Determine the values of $R/\rho\sqrt{\omega\nu}$, $\delta/0.85d_1$, v_2/v_0 and $v_0/\sqrt{\omega\nu}$ as a function of the $P'/\rho\omega\nu$, t_p/d_1 , d_2/d_1 , and θ for the problem of zero mean sinusoidal oscillating flow through two orifices in series, Fig. 4.1.

The overall experiment design was developed around the use of a piston driven cylindrical test section to produce oscillating flow through two orifices in series. A standing wave method incorporating a pressure measurement and a piston displacement measurement was used for the determination of z_0 and $v_0(t)$. $v_2(t)$ was measured using a hot wire anemometer.

4.4 Experiment Apparatus

The test section, Fig. 4.6, consisted of a 50.8 cm long aluminum cylinder with a vibrating piston at one end and a double orifice arrangement at the other. The cylinder had a honed inside diameter of 19 cm and a wall thickness of 0.6 cm and was oriented vertically. The locations on the test section where data were recorded are indicated by letters on Fig. 4.6. Acoustic pressure was measured at

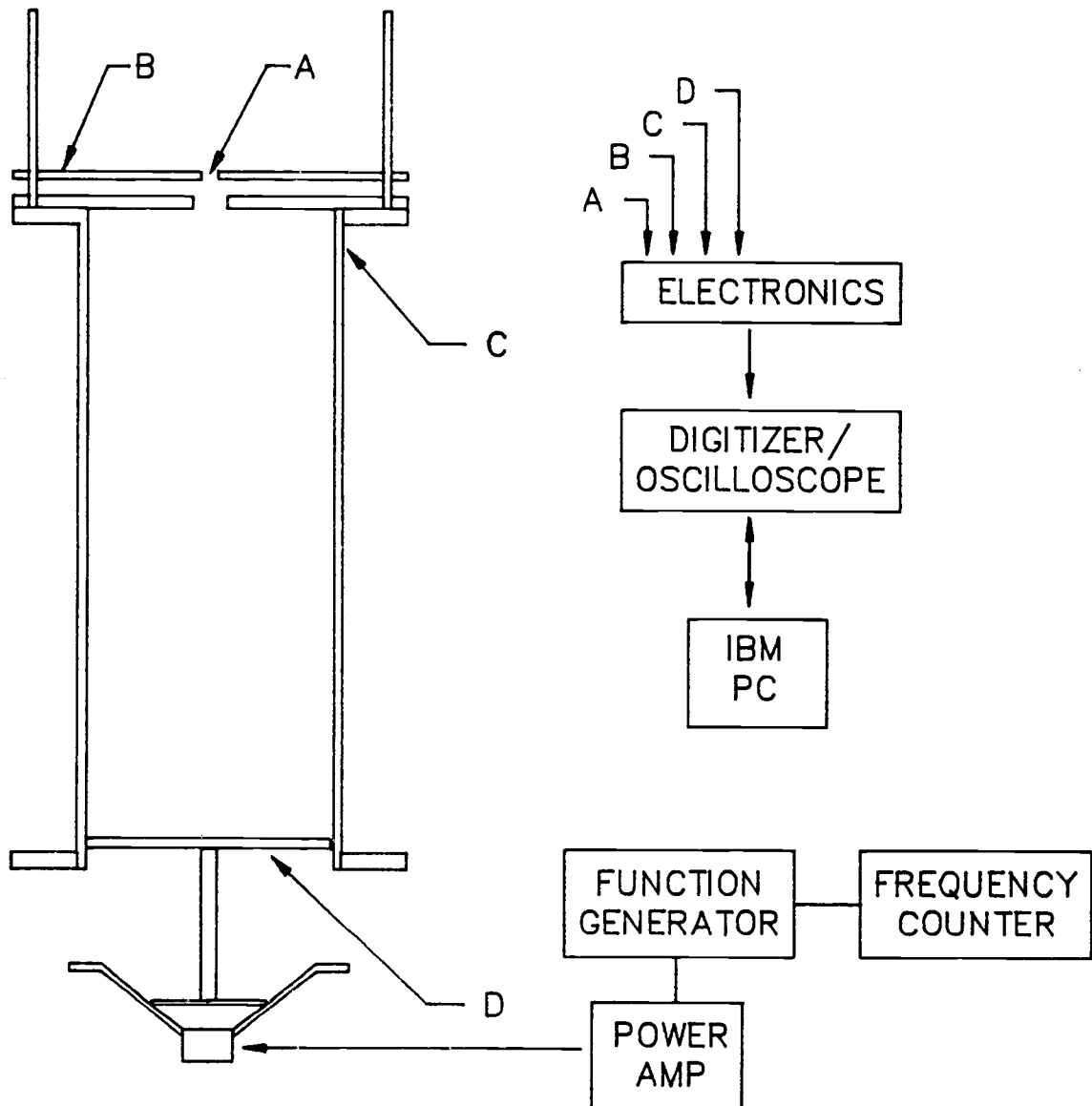
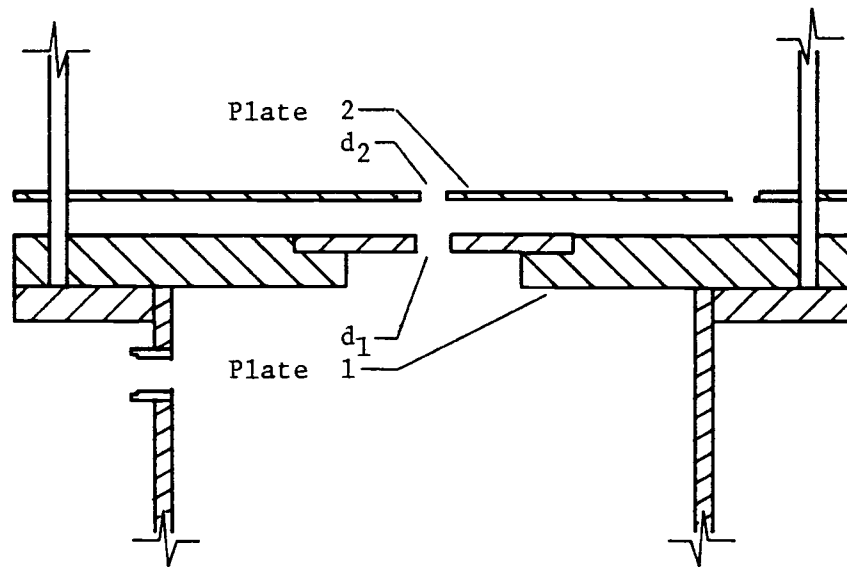
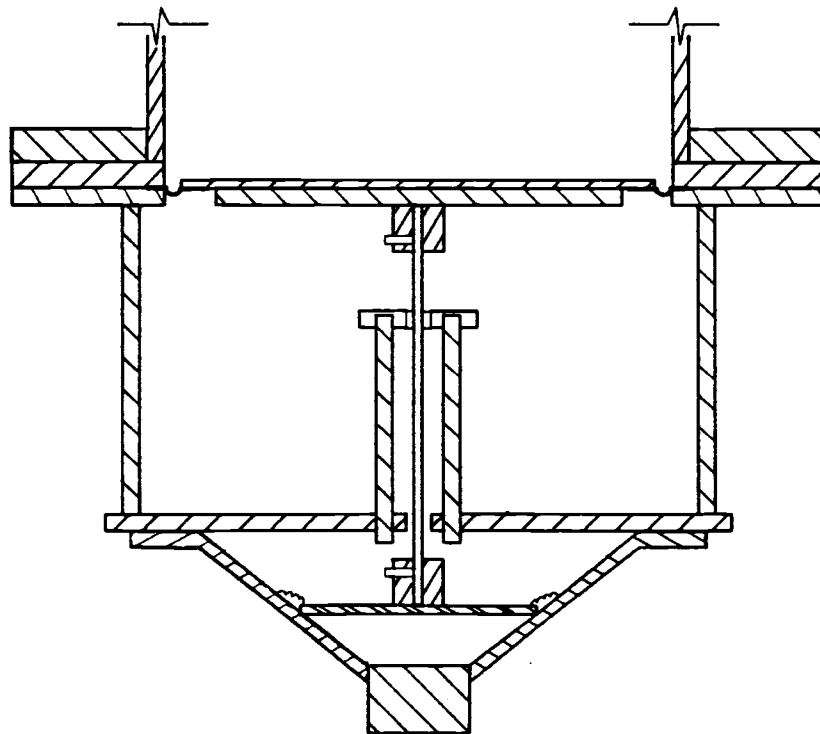


Fig. 4.6. Simplified cross sectional view of test section



(a)



(b)

Fig. 4.7. (a) Double orifice assembly in cross section
(b) piston/driver assembly in cross section

points B and C (the access ports are shown on Fig. 4.7a), piston position was measured at point D and fluid velocity was measured at point A.

The piston assembly, Fig. 4.7b, consisted of a 17.8 cm diameter by 0.16 cm thick aluminum plate bonded to a ring of 0.038 thick latex rubber and an 0.16 cm thick aluminum support rib. By sandwiching the latex between two aluminum rings, pressure seal was achieved with no friction between the piston plate and the cylinder walls. The support rib was used because the plate's natural frequency without the rib was ≈ 180 hz. A flat piston motion was important to relate a local measurement of piston displacement to average piston displacement.

A 0.32 cm diameter by 14 cm long, steel rod served as the piston rod. A sleeve bearing was used to minimize wobble and to align the piston perpendicular to the bore. Since piston displacements as small as 3 μm peak to peak were used, alignment of the piston rod in the bearing was critical to smooth piston operation. There were three tricks for obtaining the required alignment. First the piston assembly was designed such that it could be assembled as a unit, independent of the cylinder. Second, the membrane was assembled with slack in it. Finally, the assembly was done with the piston vibrating near its minimum value and any misalignment could be observed and corrected as soon as it occurred.

The piston was driven by mechanically coupling the piston rod to the paper cone of a 20 cm woofer type loudspeaker. A sine wave output from a Tektronix FG 501A function generator was amplified with a Dynaco mono amplifier to power the speaker. All data were taken at ≈ 52 hz.

The double orifice configuration, Fig. 4.7a, consisted of plate 1 with an insert containing the d_1 orifice and an acrylic plate 2 with the d_2 orifice. Plate 1 was fabricated from 1.8 cm thick aluminum plate and had a 6 cm diameter through hole with a 10 cm diameter recess. The d_1 insert was machined flush with the top surface of plate 1 and had a snug sliding fit into the recess to provide align-

ment. Plate 2 was positioned vertically using threaded rods for support and 3 smooth rods to provide alignment.

The boundary at the outer edges of plates 1 and 2 was open to ambient in some cases and closed in others. In the closed cases, 0.06 cm steel shim stock was wrapped around the edges of the plates and two hose clamps were used to compress a neoprene gasket between the plate edges and the steel wall.

To measure $v_2(t)$, pt. A, a constant temperature hot wire anemometer probe was used. In general, $v_2(t)$ was an oscillating reversing flow which is not easy to measure by any method. The development of the method for using the hot wire to make this measurement is presented in §4.5.3. The hot wire probe used, a TSI 1210-T1.5, was a 3.8 μm diameter platinum coated tungsten wire with an active sensing length of 1.27 mm and a wire length of 1.52 mm. The anemometer bridge circuit was a TSI 1050 and 2 VDC was subtracted from the signal with a TSI 1057 signal conditioner. No filtering was performed. The probe was operated at 250 °C and the system frequency response was estimated to be 102 khz.

A vertical (end on flow) hot wire probe orientation with the probe axially and radially centered in the orifice was used. Positioning of the probe was performed with a three axis Velmex unislide assembly, which has a stated accuracy of $\pm 125 \mu\text{m}/\text{m}$. The method used for referencing the hot wire was to "eyeball" the probe to the center of orifice, flush with the top surface. From this reference point the probe was moved to the vertical center of the orifice, where data was recorded.

Piston position was measured with a Bently Nevada 7200 series proximity transducer which has an operating range to 10 khz. Pressure was measured with a 1.3 cm GenRad measuring microphone. Frequency measurements were performed with a Tektronix DC 503A counter.

The data acquisition system consisted of a Tektronix 7D20 digitizer interfaced via a GPIB to an IBM PC. All voltage signals were averaged over ≈ 250 cycles to remove random noise in pressure, position and velocity and fluctuations (due to flow instabilities and turbulence) in the velocity channel. This averaging greatly improved

the repeatability of the data and also made it possible to record data at very low amplitudes. Observations of the unaveraged waveforms indicated that in some cases the averaging removed information about the unsteady nature of $v_2(t)$. Voltage and time measurements were recorded off the digitizer using cursors, with the PC functioning as a data storage and display system.

4.5 Experimental Methods

4.5.1 Calibration

From Fig. 4.7b, it is seen that the piston area was not equal to the area of the test section cylinder. The parameter of interest in determining z_0 was average piston displacement, $s(t)$. To relate $s(t)$ to the measured piston displacement a closed tube calibration procedure was employed. From Tempkins [44] the solution to the pressure field in a piston driven closed tube is:

$$P'(x,t) = \frac{i\rho c \omega s \cos kx}{\sin kL} e^{-i\omega t} \quad (3)$$

Thus by measuring $P'(x=0,t)$, it was possible to relate voltage signal from the position transducer to a known $s(t)$. However, it was discovered during the calibration procedure that at many frequencies $P'(x=0,t)$ and $s(t)$ were slightly out of phase, indicating the presence of unexplained damping. While the cause of this was not established, it was found that the problem was not present at 52 hz. Since the damping would have introduced bias errors into z_0 , all data were recorded at 52 hz.

4.5.2 Impedance Measurement

z_0 for the double orifice geometry is defined by (1) with $P'_1(t) = P'(t)$ taken to be the pressure within the tube and $P'_2(t)$ taken to be ambient pressure. As discussed in §4.1 most impedance measurements are based on some variation of a standing wave method. Unfortunately, the relationship between the measured variables and z_0 is different in almost every case. The basis for the z_0 calculation

for the work described here is the solution for the pressure field in a piston driven tube, Fig. 4.6, which was given in Chapter 2 as:

$$P'(x,t) = \frac{i\rho c\omega s (\sin(kx) - i z_o/Z \cos(kx))}{(\cos(kL) - i z_o/Z \sin(kL))} e^{-i\omega t} \quad (4)$$

where L = tube length, k = wave number, and Z = fluid characteristic impedance = $\rho c/A$. Inverting (3) yields an equation for z_o in terms of measurable variables:

$$\frac{z_o}{Z} = \frac{iF \cos(kL)}{1 - F \sin(kL)} \quad (5)$$

where F , the reflection coefficient, is given by:

$$F = \frac{P'(x=0,t)}{\rho c\omega s(t)} = \frac{P' e^{i\alpha}}{\rho c\omega s} \quad (6)$$

and $P'(x=0,t)$ is pressure measured at the orifice end of the tube (but at least 3 diameters away from the orifice), $s(t)$ is piston position and α is the phase angle in radians that $s(t)$ lags $P'(x=0,t)$.

A problem with any standing wave method is that if an "impedance mismatch" occurs, it is possible for small measurement errors to introduce large errors in z_o . For example, this impedance mismatch will occur when the orifice is so small that the pressure field in the tube is almost the same as a closed tube. In this case, changing z_o by a significant amount will produce only a slight change in the pressure field. Conversely, a small measurement bias error at these conditions will introduce a large change in calculated z_o .

To track when impedance mismatch problems could occur, an estimation of experimental uncertainty was made. A standard root mean squared uncertainty method was used to yield:

$$\frac{dz_o}{z_o} = \frac{\left(\left(\frac{\partial z_o}{\partial (P'/s)} \Delta \left(\frac{P'}{s} \right) \right)^2 + \left(\frac{\partial z_o}{\partial \alpha} \Delta \alpha \right)^2 \right)^{1/2}}{z_o} \quad (7)$$

where $|P'/s| = |P'(x=0,t)/s(t)|$, $\Delta|P'/s|$ is the uncertainty in $|P'/s|$ and $\Delta\alpha$ is the uncertainty in alpha. Substituting (5) and (6) into (7) yields:

$$\frac{dz_0}{z} = \frac{e^{i\alpha} [(\Delta \frac{P'}{s})^2 + (i \frac{P'}{s} \Delta \alpha)^2]^{1/2}}{F (1 - F \sin(kL))} \quad (8)$$

It should be mentioned the use of uncertainty analysis for impedance measurements was not found in the studies review in §4.1. Since the problem of impedance mismatch is fundamental, (8) was used for all impedance measurements reported here.

To verify (5) and the equipment used, a measurement of orifice impedance for a single orifice was made and the results compared with published data. A sharp edged orifice with a 0.953 cm diameter by 0.112 cm thickness was used. The driving frequency was 52 hz. Typical $P'(t)$ and $s(t)$ curves for a z_0 calculation are shown on Fig. 4.8.

A comparison of the measured impedance data with the compilation of data presented by Panton and Goldman [28] is shown on Fig. 4.9. Values from [28] are based on curve fits to figures presented there. The use of two curves on Fig. 4.9b bounds the scatter in the $\delta/0.85d$ data from [28]. Experimental uncertainty calculated from (8) is shown in Fig. 4.10.

4.5.3 Use of the Hot Wire Anemometer

Measurement of $v_2(t)$, which is not always monochromatic, required an instrument capable of measuring a dynamic reversing flow. The hot wire anemometer (HWA) was used, but the development of methods to interpret the output signal was not an easy task.

It was initially assumed that a steady flow (static) calibration would be adequate to interpret the HWA voltage signal, $U(t)$, but this was not the case. In particular, the voltages corresponding to flow reversal clearly were not predicted correctly by static calibration results. There were also a number of questions about the relationship of the shape of $U(t)$ to $v_0(t)$.

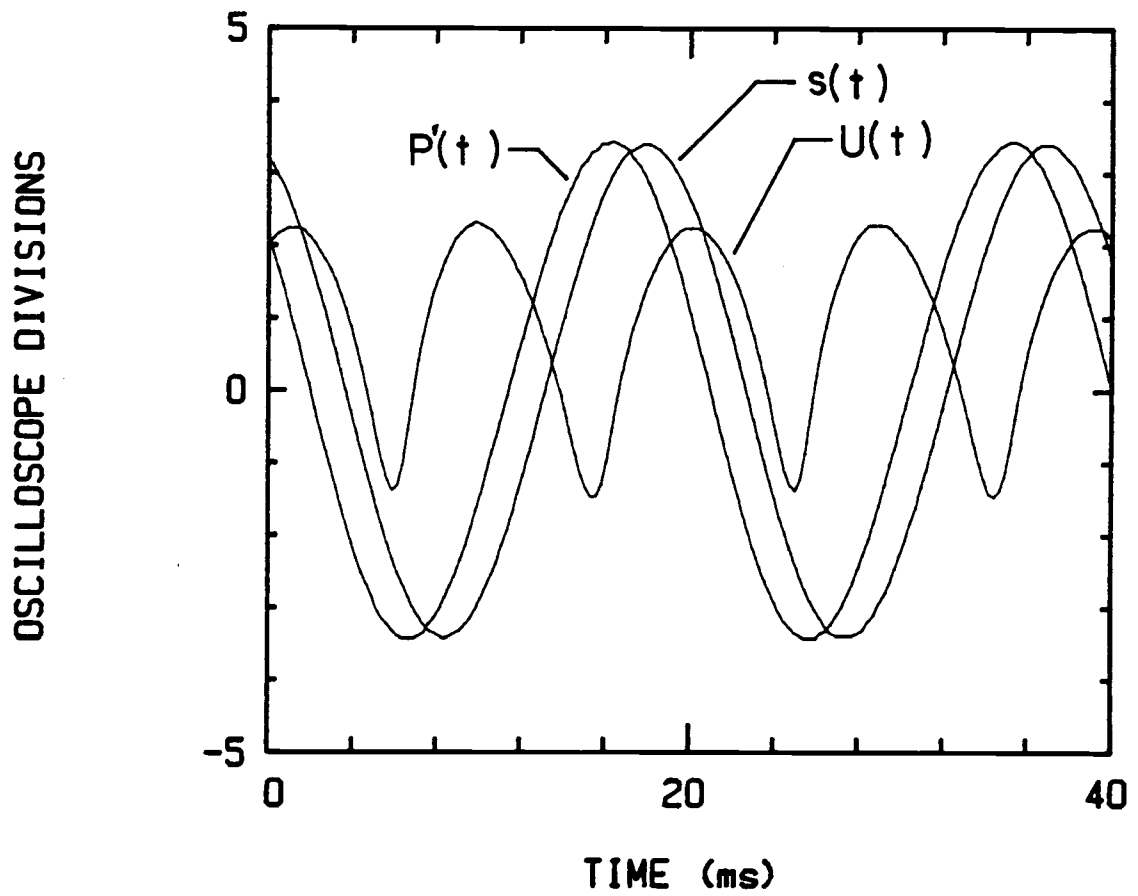


Fig. 4.8. Typical oscilloscope curves for $P'(t)$, $s(t)$, and $U(t)$ for the test section with a single orifice

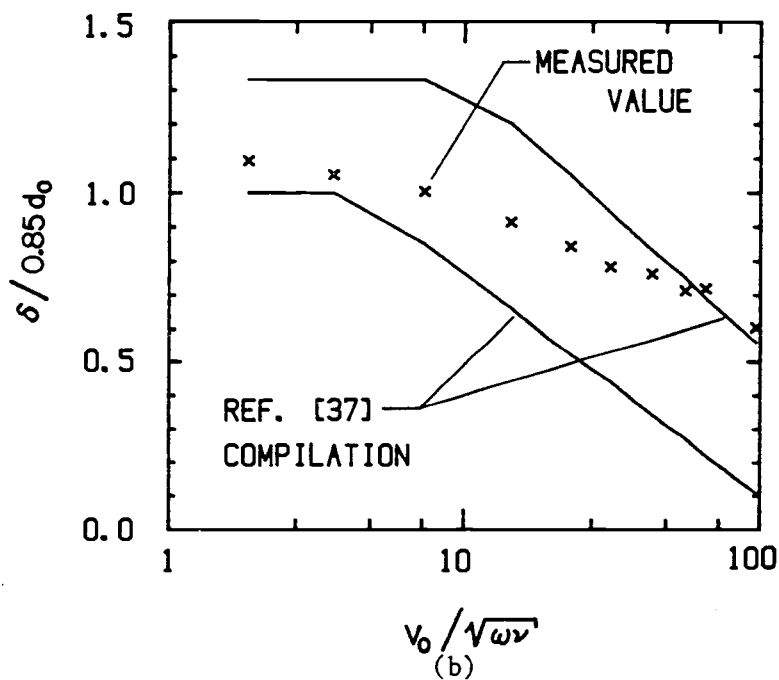
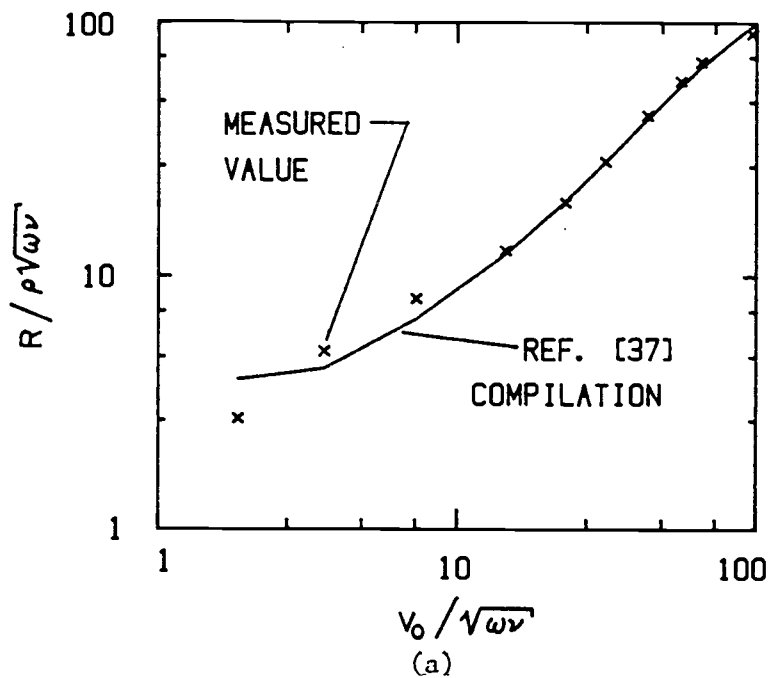


Fig. 4.9. Comparison of measured orifice parameters, R and δ , with the data compiled by Panton and Goldman [28]

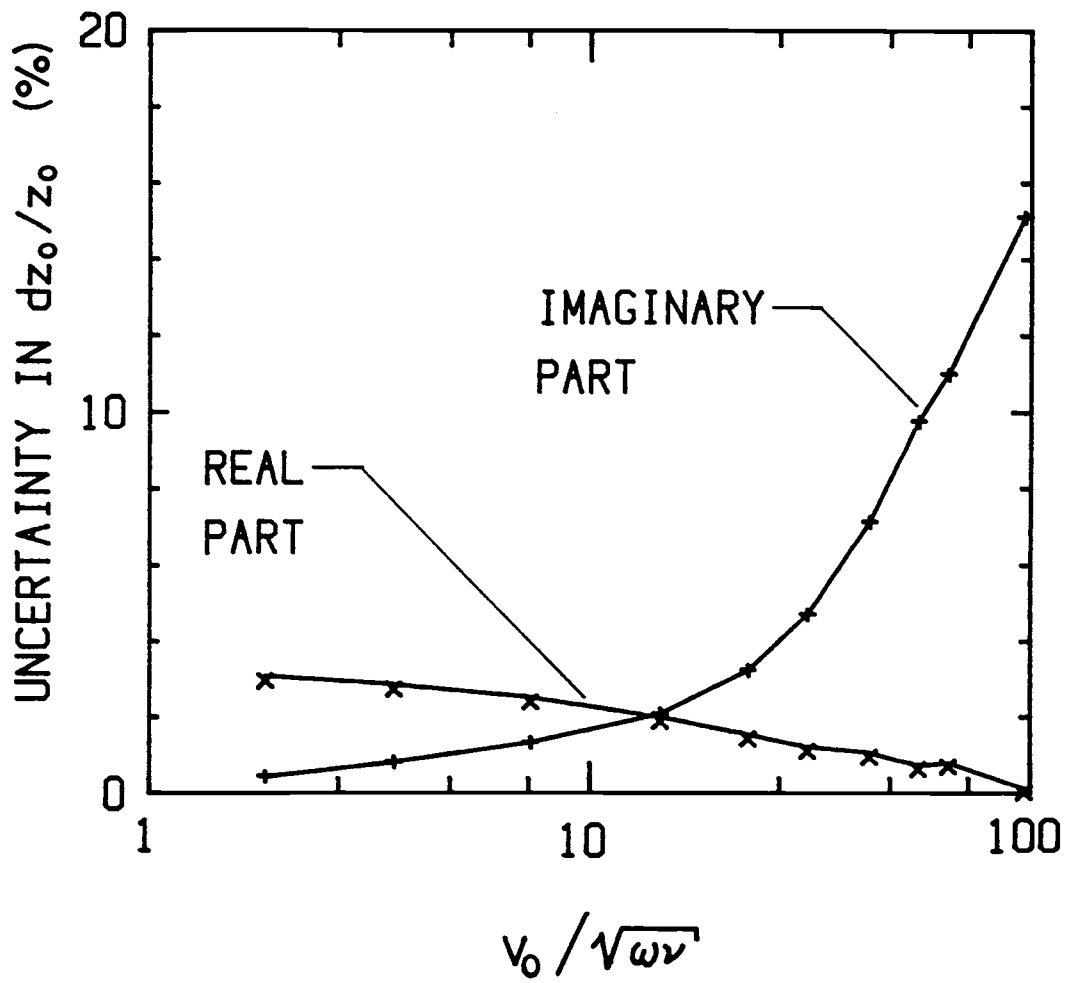


Fig. 4.10. Experimental uncertainty for the data presented in Fig. 4.9

As discussed in §4.1, the HWA was used by Ingard and Ising [38] to measure oscillating flow through a single orifice. They used a static calibration and positioned the HWA probe in the center of the orifice. Attempts to repeat their experiment were quite successful in terms of replicating their data. Unfortunately, it also appeared that this HWA data was in disagreement with the body of literature for values of $v_0/\sqrt{\omega\nu}$ (z_0 correlates quite strongly with $v_0/\sqrt{\omega\nu}$) less than ≈ 60 . Due to this factor and the lack of success in explaining the relationship of $U(t)$ to $v_0(t)$ it was felt that a need existed to understand this problem.

Thus, a dynamic calibration approach, using an apparatus to produce a sinusoidal flow field with known magnitude and phase, was developed [chapter 3]. By inserting the hot wire into this flow field a relationship between velocity and bridge voltage was found. The dynamic calibration results were not developed to the point of being able to relate instantaneous bridge voltage to instantaneous fluid velocity. Rather, the development was limited to correlating the maximum and minimum values of $U(t)$ to v_0 and the point of flow reversal, respectively. In addition qualitative observations about the shape of $U(t)$ for sinusoidal $v_0(t)$ were made.

The results of the dynamic calibration were: (i) the static calibration results were accurate for predicting the velocity amplitude for $v_0 < 1$ m/s and slightly overpredicted the velocity amplitude for 1 m/s $< v_0 < 5$ m/s (ii) the static calibration results were not accurate for determining the phase of the velocity or for interpreting the velocity around the points of flow reversal, and (iii) a sinusoidal oscillating fluid velocity produces a bridge voltage which is reasonably close to a rectified sine wave.

A second major problem was that fluid velocities in the orifice were found to vary significantly in magnitude and in phase for different spatial locations within the orifice. Standing wave methods, which produce an average value for velocity and phase, are not affected by this problem. The HWA, which measures velocity at a very small region in space, will give quite different readings for different axial and radial positions within the orifice.

The procedure followed in obtaining HWA data was to position the HWA in the axial center of the orifice and to perform measurements over the cross section. A numerical integration of the results provided an estimate of v_0 . A problem with this procedure was that it was not possible to approach much closer than 500 μm to the wall. Because most of the flow area is near the walls, this introduced uncertainty in the v_0 estimate.

To verify the procedures used, a comparison was made between the standing wave method and the HWA measurement methods for oscillating flow through a single orifice. Typical waveforms, Fig. 4.8, illustrate $U(t)$ as measured at the center of the orifice, $s(t)$ and $P'(t)$. Values of v_0 and the phase of $v_0(t)$ as determined by the two methods are compared on Fig. 4.11. The HWA measured v_0 magnitude was calculated from a radial average of v_0 over the orifice cross section and the phase of v_0 was calculated from the measurement at the center of the orifice.

As shown in Fig. 4.11, the predictions of the magnitude of v_0 by the HWA and the standing wave method are in very good agreement. Indeed, it is felt that the agreement is somewhat fortuitous, the accuracy shown on the figure could not be supported by a rigorous uncertainty analysis. On the other hand, the predictions of the HWA method for the phase of v_0 do not compare very favorably with those of the standing wave method. Part of the reason for this is that as the HWA probe was moved closer to the walls, the phase lag decreased. However, even when this effect was accounted for the two methods did not agree very well. Referring back to Chapter 3, Fig. 3.10, it is seen that assessing the phase lag of the HWA system from the dynamic calibration results is not particularly straightforward. The conclusion is that the HWA system when combined with a radial averaging and dynamic calibration provides a reasonable good estimate of the magnitude of v_0 but not a good estimate of the phase of v_0 . Consequently, the HWA was only used to measure magnitudes.

A final observation is that measuring $v_2(t)$ is much more complicated than measuring $v_0(t)$. The general conclusion was that a HWA can accurately be used for determining peak velocity magnitude.

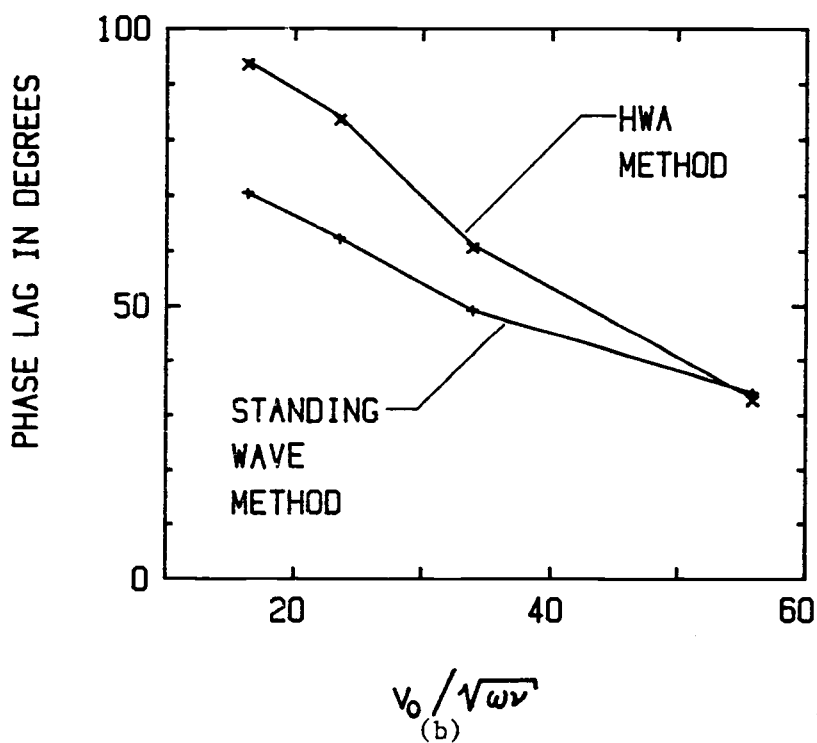
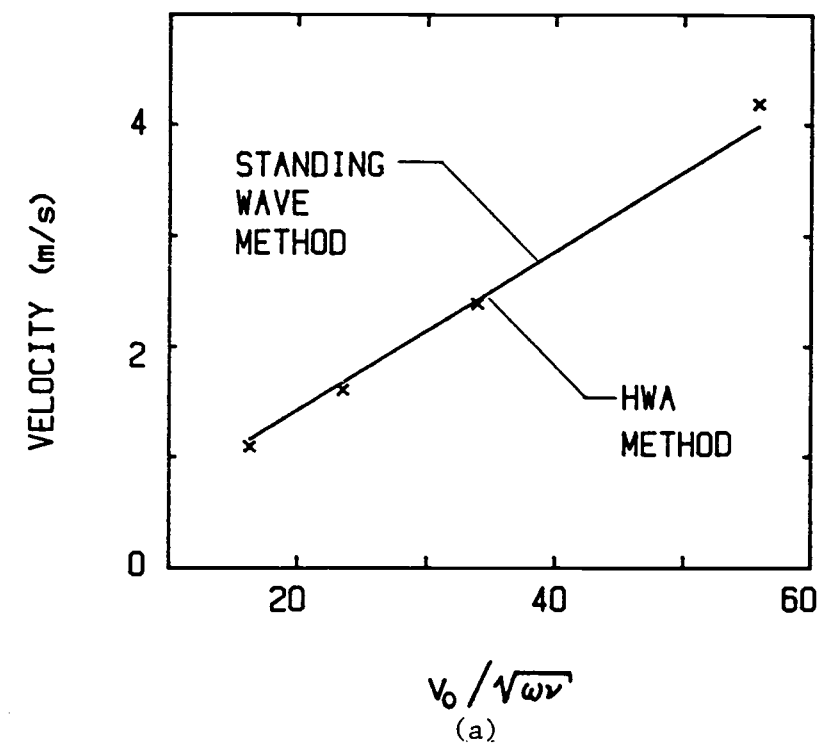


Fig. 4.11. Comparison of orifice velocity, $v_o(t)$, as measured by a hot wire anemometer and a standing wave method (a) $|v_o|$ and (b) phase lag of $v_o(t)$ behind $P'(t)$

Thus, the quantitative information about $v_2(t)$ presented in the next section is peak velocity magnitude.

4.6 Experimental Results and Discussion

Twenty four sets of data were recorded and these are summarized in Table 4.2. The approach taken was to focus the study on the effects of d_2/d_1 , t_p/d_1 and $P'/\rho\omega v$ for an open outer boundary; and then record data for a few cases with a closed outer boundary. Hence, the first twenty data sets in Table 4.2 are for the open outer boundary case and the last four are the closed outer boundary case.

Typical oscilloscope waveforms for three data sets are shown in Fig. 4.12. In all 24 data sets, $s(t)$ and $P'(t)$ were sinusoidal with no apparent nonlinearities. $P'_2(t)$ was typically monochromatic for low $P'/\rho\omega v$ values, Figs. 4.12 a&b. For high $P'/\rho\omega v$ values, $P'_2(t)$ showed the presence of harmonic distortion, Fig. 4.12c.

$U(t)$ which correlates with $v_2(t)$, was sometimes similar to that observed for a single orifice, Fig. 4.12a and Fig. 4.8, indicating the presence of an oscillating reversing flow through the second orifice. $U(t)$ for some cases had the appearance of a rectified flow, Fig. 4.12 b&c, indicating that the flow does not reverse directions in the second orifice.

In this paragraph the author's interpretation of $U(t)$ for the "rectified" cases will be presented. In some cases, ex. Fig. 4.12b, the flow is truly a rectified flow varying between zero velocity and a peak velocity. In other cases, the fluid velocity never reaches zero, Fig. 4.12c, but rather varies between a minimum positive velocity and a maximum positive velocity.

The $v_2(t)$ waveforms for the closed outer boundary cases would qualitatively be similar to Fig. 4.12a, in all cases.

In addition to the data in Table 4.4, a flow visualization study was conducted [48]. The objective was to gather quantitative and qualitative information about the flow in the regions between the two plates shown in Fig. 4.1. A summary of the methods and typical photographs are presented in Appendix A.

Table 4.2. Experimental data.

ID	$d_2/d_1^{(1)}$	ϵ_p/d_1	$P'/\rho\omega v$	θ	d_1 (cm)	$A_0 \tau_0$		$v_0/\sqrt{\omega v}$	$R/\rho\sqrt{\omega v}$	$\delta/0.85d_1$	$P_2'/P'^{(2)}$		$v_2/v_0^{(3)}$	
						mag ($\text{kg/m}^2 \cdot \text{s}$)	arg (degrees)				(mag)	phase lag (m/s)	(mag)	Shape
D1	0.790	0.85	1388	1	0.935	5.5	-78	21.2	14.0	1.16	0.029	0.30	0.43	a
D2	0.790	2.15	1380	1	0.935	5.0	-77	23.4	13.1	0.99	0.017	0.40	0.23	b
D3	0.790	2.15	3423	1	0.935	4.7	-44	60.9	40.6	0.48	0.018	1.34*	0.62	c
D4	0.370	2.15	3423	1	1.999	10.5	-82	27.6	18.1	0.98	0.023	0.18	0.21	a
D5	0.790	0.85	3390	1	0.935	5.2	-55	55.3	35.3	0.78	0.031	2.74**	0.60	b
D6	0.370	2.15	1405	1	1.999	10.5	-87	11.3	7.5	1.00	0.023	0.02	0.25	a-b
D7	0.370	0.85	3423	1	1.999	11.6	-82	24.9	18.2	1.15	0.038	0.15	0.74	a
D8	0.370	0.85	1337	1	1.999	11.6	-87	9.8	8.2	1.16	0.038	-0.07	0.69	a
D9	0.940	1.50	2402	1	0.790	4.1	-55	49.2	28.1	0.70	0.022	1.09*	0.48	-
D10	0.230	1.50	2385	1	3.272	16.7	-87	12.1	9.5	0.96	0.035	-0.05	0.47	a
D11	0.580	2.60	2418	1	1.273	6.5	-76	31.2	18.2	0.92	0.017	0.35	0.36	b
D12	0.580	0.40	2435	1	1.273	8.7	-79	23.6	20.3	1.45	0.042	0.06	1.03	a
D13	0.580	1.50	4122	1	1.273	6.5	-68	53.3	29.5	0.85	0.024	0.75	0.53	b
D14	0.580	1.50	662	1	1.273	7.2	-85	7.8	7.7	1.11	0.024	-0.04	0.29	a-b
D15	0.580	1.50	2402	1	1.273	6.9	-77	29.4	18.5	1.01	0.007	-0.69	0.51	b
D16	0.580	1.50	2418	1	1.273	7.0	-77	29.3	19.1	1.03	0.024	0.41	0.51	b
D17	0.580	1.50	2385	1	1.273	6.9	-77	29.2	18.2	1.01	0.024	0.40	0.51	b
D18	0.580	1.50	2402	1	1.273	6.9	-77	29.4	18.3	1.01	0.024	0.35	0.52	b
D19	0.580	1.50	2402	1	1.273	6.9	-77	29.1	18.5	1.01	0.024	0.41	0.50	b
D20	0.580	1.50	2402	1	1.273	7.0	-77	29.1	18.8	1.03	0.023	0.38	0.52	b
D21	0.633	0.75	2400	0	0.789	7.8	-61	30.00	45.0	2.01	0.66	-0.92**	2.30	a
D22	0.633	2.50	593	0	0.789	13.0	-61	3.86	75.1	3.73	0.72	-0.58	4.06	a
D23	0.394	2.50	2459	0	1.270	16.2	23	12.90	176.2	0.95	1.20	-0.84*	5.82	a
D24	0.394	0.75	578	0	1.270	24.9	-62	1.91	141.1	4.83	0.87	-0.39	9.71	a

¹ $d_2 = 0.74$ cm for runs D1-D20, $d_2 = 0.50$ cm for runs D21-D24; $f = 52$ Hz for runs D1-D24

² P_2'/P' is presented in two parts, the magnitude is equal to the ratio of the peak values; the time lag is equal to the time lag of $P'(t)$ behind $P_2'(t)$. The asterisks indicate that P_2' was nonlinear; two asterisks indicate more nonlinearities than one asterisk.

³ v_2/v_0 = the maximum positive velocity out the second orifice divided by the magnitude of v_0 . The shape is the shape of the $v_2(t)$ waveform. The letters correspond to the shapes shown in Figs. 4.12a-c, respectively. a-b indicates that the shape is somewhere between that of a and b.

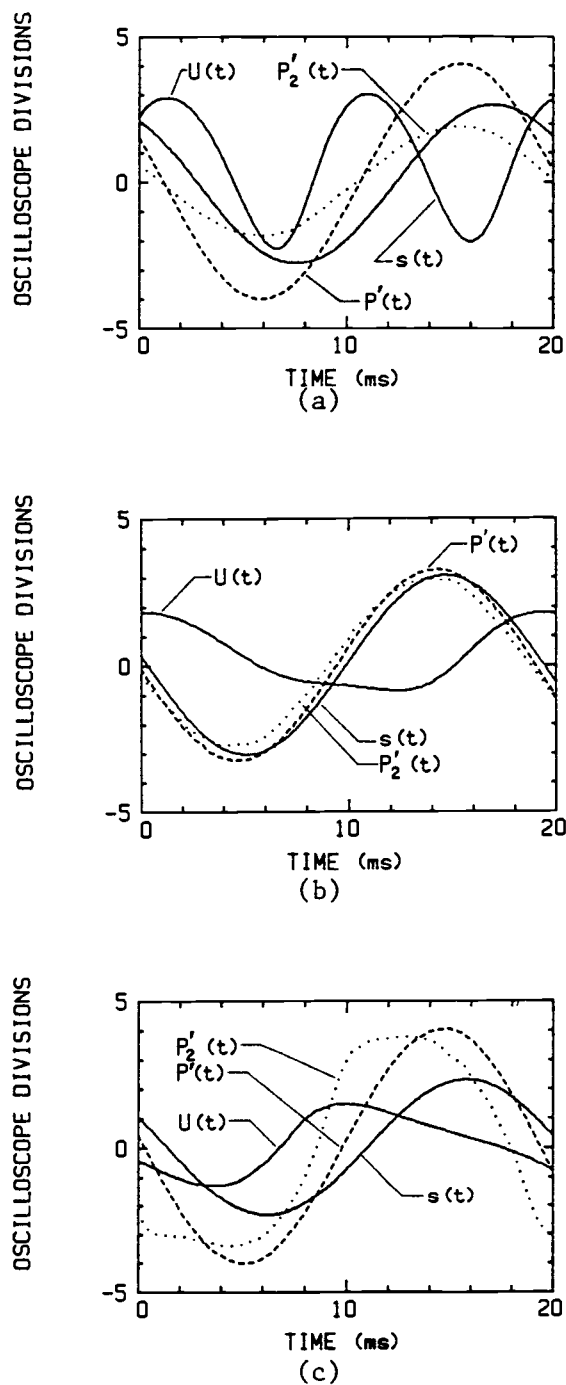


Fig. 4.12. Typical oscilloscope waveforms for $s(t)$, $P'(t)$, $P'_2(t)$, and $U(t)$ for the test section with a double orifice opening: (a) run D4, (b) run D2, and (c) run D3

In a simplified description of oscillating flow through a single orifice, the streamlines will appear as a jet on the outflow part of the cycle and as a potential flow into a sink on the inflow part of the cycle. The actual flow pattern can exhibit many more complexities, such as acoustic circulations, vortices, and shed vortex rings [41].

For the double orifice case, on the outflow part of the cycle the flow out the lower orifice appeared as a jet. This jet impinged on the smaller upper orifice creating a jet out the upper orifice and a vortex in the region between the two plates. On the inflow part of the cycle, the flow into both orifices appeared as a potential sink flow.

Typical photographs of the vortices formed between the two plates are presented in Fig. A.3. Two distinct types of vortices were observed. The first type, Fig. A.3a, consisted of a row of separated vortices radiating outward from the bottom surface of the upper orifice. Each flow cycle through the orifices produced a vortex at the lower perimeter of the top orifice. The next cycle forced this vortex outward, replacing it with a new vortex, and so forth. The second type, Fig. A.3b, consisted of vortices inside vortices. In this case a flow cycle produced a vortex at the lower edge of the top orifice. The next cycle formed a vortex within the original vortex causing it to expand outward and downward around the new vortex.

One of the types of measurements attempted in this research was the measurement of the fluid velocity between the two plates. However, the HWA signal was very unsteady and interpretation of the signal was not successful. The complex flow patterns shown by the flow visualization results provide some explanation for the very complicated HWA signal observed.

One of the original reasons for the double orifice nozzle in an ink-jet printhead was that it would provide a rectifying effect [35]. One the outflow portion of the cycle the fluid would jet out the two nozzles forming a drop. On the inflow portion of the cycle the refill would come from a potential sink flow originating between the two plates. Thus, the fluid in the upper orifice would not have a tendency to reverse directions. The data shown on Fig. 4.12b, Fig. 4.12c, and in Table 4.2 shows that for certain parameter conditions this does indeed occur.

The flow visualization results provide a physical explanation of how the double plates promote the rectifying nature of the geometry under study. The outflow phase of the cycle starts the fluid rotating in a direction tending to eject fluid out the upper orifice and refill it back into the lower orifice. On the inflow phase of the cycle when the fluid is reversing direction through the orifices, the spinning flow opposes flow down through the upper orifice and promotes a potential flow into the lower orifice.

However, it was not possible to determine the extent to which the observed rectifying effects were due to the mechanism described in the previous paragraph. If one takes velocity data moving upward along the center line of a single orifice, similar "rectified waveforms" to those in Fig. 4.12b will be observed. Since a systematic study of the single orifice has not been done, there was no basis for comparison. Thus, it is possible that the same rectified HWA waveform, Fig. 4.12b for example, would have been measured if the HWA probe was in the same location but the upper orifice plate was absent.

One might note that the independent variables in Table 4.2 have no easily recognizable pattern. This is because an experiment design approach described by Diamond [45] was used to set up the experiment (the particular method is called a uniform precision central composite rotatable experiment design). A number of observations may be made about these methods. They are really an "experiment optimiza-

tion" in the sense of providing the most results for a given number of data points. Because of the way the experiment design is structured, curve fits of the data are easy to obtain. Statistical interpretation of the data is part of the experiment design methodology.

The following comments may be made about the particular method used here. The first 14 runs in Table 4.2 provide a quadratic estimate including cross terms, of the the effects of the independent variables on the dependent variables. The next 6 runs provide a data base for estimating the variance of the dependent variables for statistical interpretation of the results.

There is more information in Table 4.2 than will be correlated here; only results for $R/\rho\sqrt{\omega\nu}$, $\delta/0.85d_1$, $v_o/\sqrt{\omega\nu}$, and v_1/v_o will be discussed. The interested reader is referred to [45] for the methods required to correlate other parameters.

Regression analysis of the Table 4.2 data produced curve fits of the form:

$$Q = b_o + \sum_i (b_{i1}\phi_i + b_{ii}\phi_i^2) + b_{12}\phi_1\phi_2 + b_{13}\phi_1\phi_3 + b_{23}\phi_2\phi_3 \quad (9)$$

where:

$$Q = R/\rho\sqrt{\omega\nu}, \delta/0.85d_1, v_o/\sqrt{\omega\nu}, \text{ or } v_2/v_o$$

$$\phi_1 = (d_2/d_1 - 0.581)/0.211$$

$$\phi_2 = (t_p/d_1 - 1.50)/0.654 \quad (10)$$

$$\phi_3 = (P'/\rho\omega\nu - 2400)/1030$$

The coefficients for (9) are given in Table 4.3. The coefficients which were not statistically significant were set equal to zero in Table 4.3. Plots of (9) are presented in Fig. 4.13.

$v_o/\sqrt{\omega\nu}$, Fig. 4.13c, was determined to depend on d_2/d_1 and $P'/\rho\omega\nu$ with essentially no dependence on $t_p/d_1(t)$. $v_o/\sqrt{\omega\nu}$ increases with

Table 4.3. Regression coefficients.

Parameter	Coefficients									
	b ₀	b ₁	b ₂	b ₃	b ₁₁	b ₂₂	b ₃₃	b ₁₂	b ₁₃	b ₂₃
$R/\rho\sqrt{\omega\nu}$	18.53	6.04	0.00	7.78	0.19	0.35	0.12	0.66	3.52	0.84
$\delta/0.85d_1$	1.017	-0.096	-0.123	-0.099	-0.073	0.052	-0.021	-0.018	-0.108	-0.017
$v_o/\sqrt{\omega\nu}$	29.29	10.96	1.81	13.15	0.42	-0.71	0.40	0.44	5.02	0.56
v_2/v_o	0.512	0.000	-0.165	0.072	-0.025	0.055	-0.047	0.100	0.068	0.017

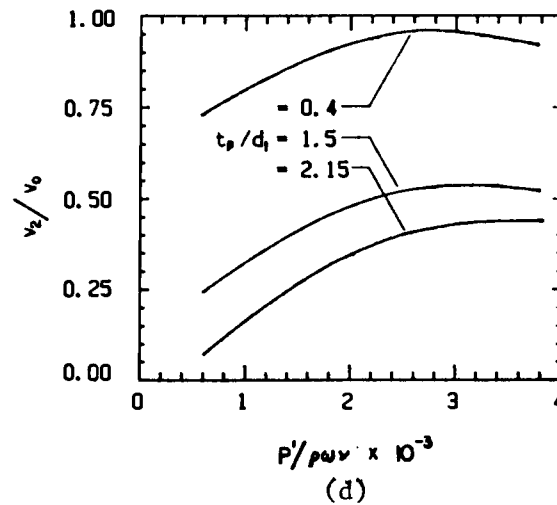
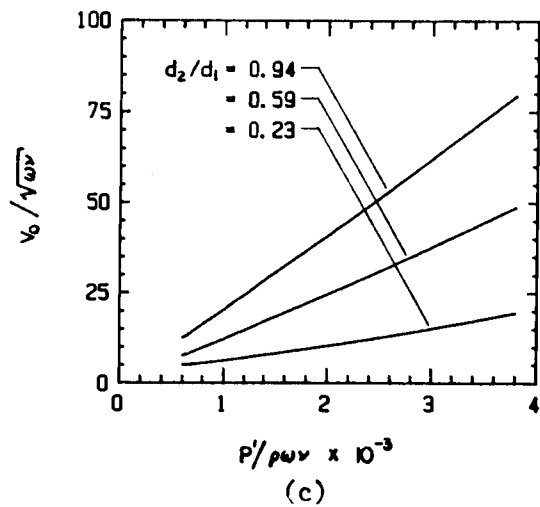
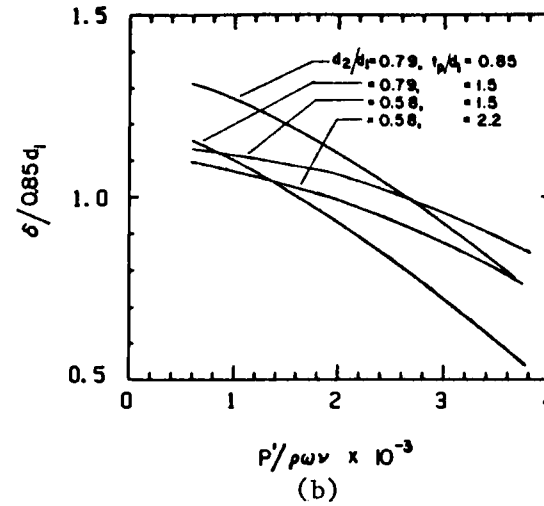
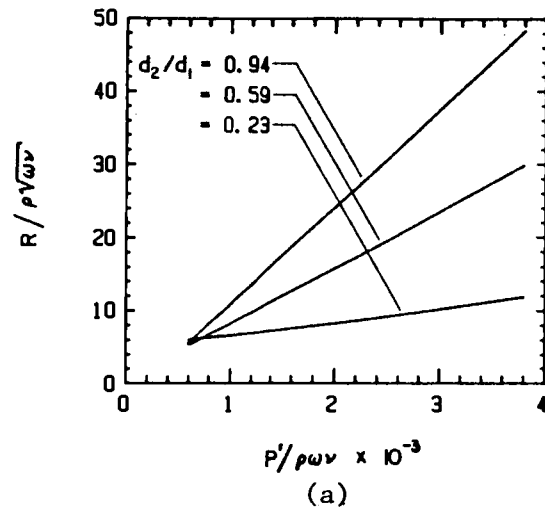


Fig. 4.13. Correlation equations for (a) $R/\rho\sqrt{\omega\nu}$, (b) d_2/d_1 , (c) $v_0/\sqrt{\omega\nu}$, and v_2/v_0

increasing d_2/d_1 as expected. The linearity of $v_0/\sqrt{\omega v}$ with $P'/\rho\omega v$ indicates that $P' \sim \rho v_0^2$, which is the result for steady flow.

$R/\rho\sqrt{\omega v}$, Fig. 4.13a, was determined to depend on d_2/d_1 and $P'/\rho\omega v$ with essentially no dependence on t_p/d_1 . The increase in $R/\rho\sqrt{\omega v}$ with d_2/d_1 is due to $v_0/\sqrt{\omega v}$ increasing with d_2/d_1 . The linearity of $R/\rho\sqrt{\omega v}$ with $P'/\rho\omega v$ indicates that the damping due to flow through the double orifice geometry is linear with v_0 (i.e., $R \approx \rho v_0$, where a is a constant). Thus, the damping takes on the same physical form as that governing both oscillating and steadyflow (at high v_0 values) through a single orifice.

$\delta/0.85d_1$, Fig. 4.13b, was determined to depend on $P'/\rho\omega v$, d_2/d_1 , and t_p/d_1 . It is seen that there are some interaction effects between d_2/d_1 and t_p/d_1 .

v_2/v_0 , Fig. 4.13d, was determined to depend on t_p/d_1 and $P'/\rho\omega v$ with essentially no dependence on d_2/d_1 . This is interesting because it indicates that v_2 can be viewed as having an origin as a jet expelled from the first orifice.

Finally, as a check for outliers and to assess the uncertainty of the calibration results, the experimental data was compared with values predicted from (9). The results are shown in Fig. 4.14 for the best and worst cases.

As previously discussed, four runs were conducted with a closed outer boundary, $\theta = 0$. The problem was not studied in a systematic way but it is possible to make several observations. As compared to the open cases runs, the closed case runs, D21-D24, showed the following characteristics. The damping term, $R/\rho\sqrt{\omega v}$, the added mass term, $\delta/0.85d_1$, and the velocity ratio, v_2/v_0 , were all significantly higher. These trends are as expected except for the damping term. Since this term is physically related to energy loss it is surprising that it is so much higher. No physical explanation of this behavior was developed. The high damping present in the closed case is of significant interest because of the possibilities of the use of this geometry for sound attenuation. In conclusion, the results are very different between the open and closed outer boundary cases and the latter will certainly provide an interesting area for future study.

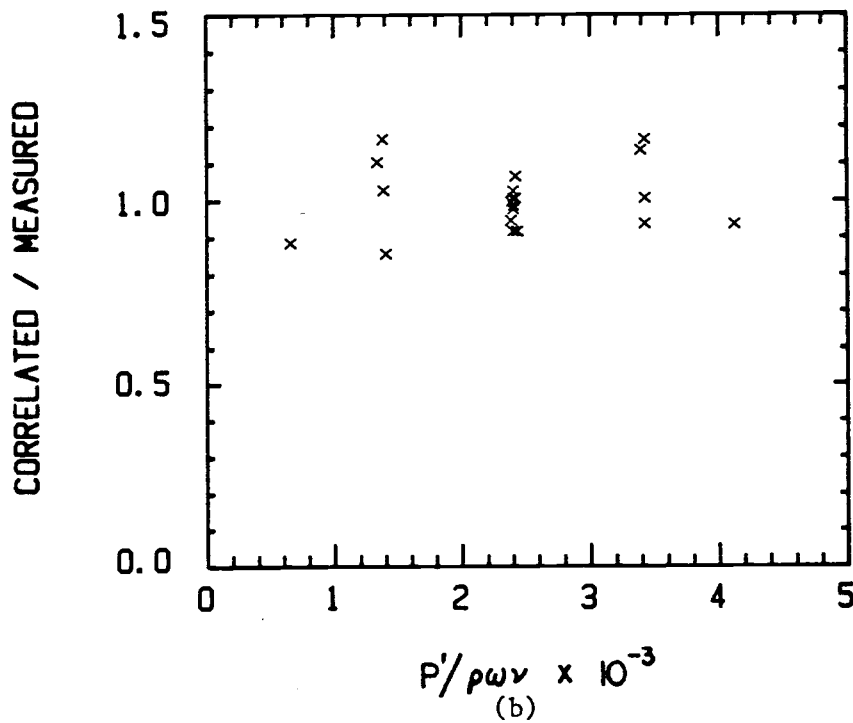
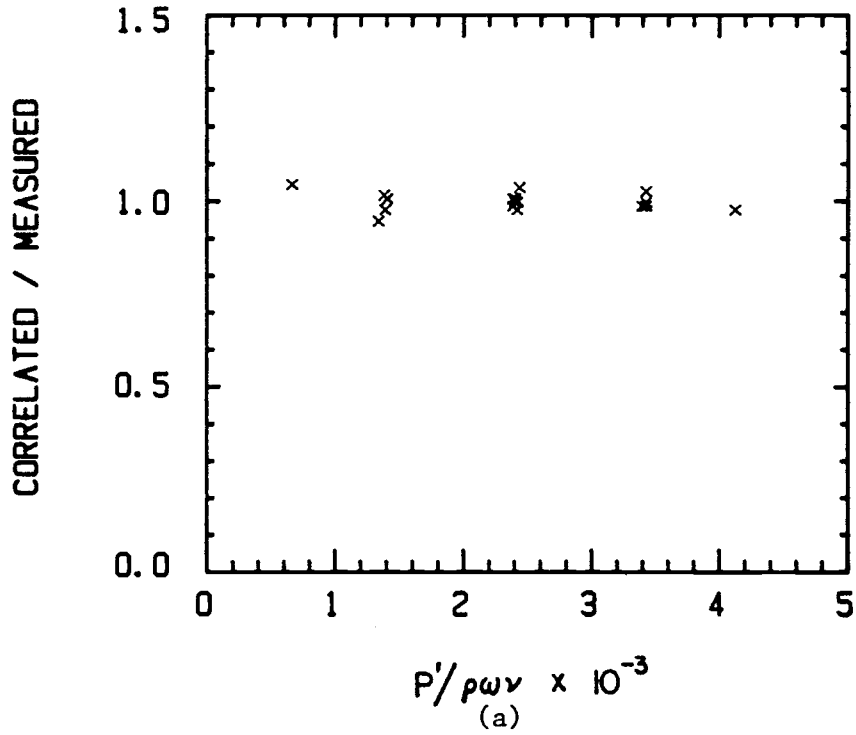


Fig. 4.14. Comparison of the measured data with the predictions of the correlation equations for (a) v_0/\sqrt{wv} and (b) v_2/v_0

4.7 Conclusions

The problem of zero mean oscillating flow through two orifices in series has been studied using dimensional analysis and experimentally. The motivation for this problem was to gather information useful for the design of the nozzle area of ink-jet printheads.

From dimensional analysis, it was determined that nine groups govern the problem fluid dynamics. By fixing the values of three groups and not considering the effects of two groups (their influence was assumed to be negligible) the number of groups was reduced to four; $P'/\rho\omega v$, d_2/d_1 , t_p/d_1 , and θ . The dependent variables characterizing oscillating fluid flow through two orifices were formulated as $R/\rho\sqrt{\omega v}$, $\delta/0.85d_1$, $v_o/\sqrt{\omega v}$, P'_2/P' , and v_2/v_o .

The problem of obtaining measurements for the problem of interest turned out to be quite formidable and required a considerable methods development effort. Of particular significance was the development of methods for using the hot anemometer for the measurement of oscillating reversing flows. The other primary measurement method was the use of a piston driven Helmholtz resonator to measure the impedance of the double orifice geometry. An experimental uncertainty equation was developed to predict when an impedance mismatch between the Helmholtz cavity and the orifice(s) could occur.

Twenty-four sets of data were recorded. Four of the sets were to provide an idea about the effect of θ . The twenty remaining sets were set up using a 3 level, 3 variable experiment design. This procedure optimized the amount of useful information about the effects of $P'/\rho\omega v$, d_2/d_1 , and t_p/d_1 on the dependent variables given above.

Results are presented as equations for $R/\rho\sqrt{\omega v}$, $\delta/0.85d_1$, $v_o/\sqrt{\omega v}$, and v_2/v_o ; as functions of $P'/\rho\omega v$, d_2/d_1 and t_p/d_1 for the following ranges of parameters: $0.23 < d_2/d_1 < 0.94$, $0.4 < t_p/d_1 < 2.6$, and $660 < P'/\rho\omega v < 4120$.

It should be stressed that the fluid dynamics of oscillating flow through two orifices was found to be an extremely complicated problem. Due to the difficult methods required to obtain data and the uncertainties introduced by the regression analysis, the overall

uncertainty of the results is estimated to be $\pm 20\%$. Furthermore, the results do not in any way provide all the details observable in the laboratory. The fluid in the region between the two orifices moves a very unsteady fashion. Often $v_2(t)$ was fluctuating in mean value and exhibited a high level of turbulence intensity. This paper should be considered as a starting point for the analysis of a complicated problem.

Several conclusions may be drawn with regards to the use of the double orifice nozzle for an ink-jet printhead. First, this nozzle design will sometimes provide a rectifying effects on the fluid flow in which case the flow out the second orifice varies between zero velocity and a positive velocity. In the author's opinion this effect could be enhanced by using orifices with different shapes than the straight ones used for this work. Predicting when the rectifying effect occurs is not straightforward. However, another major advantage of the double orifice geometry is that a large first orifice diameter increases the system Helmholtz natural frequency. This in turn will allow better drop control and/or faster allowable drop ejection rates.

CHAPTER 5

SUMMARY AND CONCLUSIONS

An experimental and analytical study of the internal fluid dynamics of a drop-on-demand (DOD) ink-jet printhead has been conducted.

The study was centered around the use of a 100x scale printhead model with air as the working fluid.

The results of the analytical study are: (i) a simple model of the ink-jet printhead including a mechanical analogy, (ii) an example of a printhead design using the model, and (iii) a discussion of the scaling of an ink-jet printhead for experimental study.

The physics of the printhead are very closely related to the physics of a Helmholtz resonator. Thus, the way sound is produced by blowing over a bottle and the way an ink-jet printhead operates have a great deal in common. In fact, both of these devices can be described by a spring/mass/damper mechanical analogy, Fig. 2.10. The design of an ink-jet printhead can be viewed as a selection of the mass, damping, and stiffness characteristics for a one degree of freedom mechanical system. In particular, ink-jet printhead operating characteristics are primarily a function of the damping introduced by the orifice and the ratio of the Helmholtz natural frequency to the printhead characteristic driving frequency.

The analysis also provided other useful information of a more detailed nature. The only mode of fluid/structure interaction in an ink-jet printhead likely to become important is that between the fluid and the horn chamber wall. For $e/D > 0.1$, this effect is not important; below this value it can be accounted for by modifying kL .

For the design of the driving element of an ink-jet printhead, the only variable influencing the internal fluid mechanics is volumetric displacement.

A dimensional analysis of a simplified ink-jet printhead was performed. The dimensionless groups were treated separately in different regions of the printhead to reflect the differences in the

physics. The analysis performed allowed the effects of the dimensionless groups to be determined. The fluid mechanics in the horn chamber are governed by kL and L/D . In addition, P'/β becomes important as it approaches a large value and S becomes important as it approaches a small value. The fluid mechanics in the orifice region are governed primarily by $v_o/\sqrt{\omega v}$ and t_o/d_o with a weak influence by S_o . The coupling between the fluid dynamics in the orifice region and the horn chamber is contained in a single group, the horn/orifice impedance ratio written as kLz_o/Z .

The final result of the analysis was that it illuminated the need for experimental information to characterize the orifice or nozzle area of the printhead. Thus, the experimental portion of this study concentrated on obtaining this data for a "Stemme" configuration nozzle. The "Stemme" nozzle consists of two concentric orifices separated by a small distance.

To obtain data for the "Stemme" nozzle, the general problem of zero mean oscillating flow through two orifices in series was studied.

From dimensional analysis, it was determined that nine groups govern the fluid dynamics problem. By fixing the values of three groups and not considering the effects of two groups (their influence was assumed to be negligible) the number of groups was reduced to four; $P'/\rho\omega v$, d_2/d_1 , t/d_1 , and θ . The dependent variables characterizing oscillating fluid flow through two orifices were found to be $R/\rho\sqrt{\omega v}$, $\delta/0.85d_1$, $v_o/\sqrt{\omega v}$, P_2/P' , and v_2/v_o .

The problem of obtaining measurements for the problem of interest turned out to be quite formidable and required a considerable methods development effort. Of particular significance was the development of methods for using the hot anemometer for the measurement of oscillating reversing flows. The other primary measurement method was the use of a piston driven Helmholtz resonator to measure the impedance of the double orifice geometry. An experimental uncertainty equation was developed to predict when an impedance mismatch between the Helmholtz cavity and the double orifices was occurring.

Twenty-four sets of data were recorded. Four of the sets were to provide an idea about the effect of θ . The twenty remaining sets were set up using a 3 level, 3 variable experiment design. This procedure optimized the amount of useful information about the effects of $P'/\rho\omega v$, d_2/d_1 , and t_p/d_1 on the dependent variables given above.

Results are presented as equations for $R/p\sqrt{\omega v}$, $\delta/0.85d_1$, $v_o/\sqrt{\omega v}$, P_2/P' , and v_2/v_o ; as functions of $P'/\rho\omega v$, d_2/d_1 , and t_p/d_1 .

Several conclusions may be drawn with regards to the use of the double orifice nozzle for an ink-jet printhead. First, this nozzle design will sometimes provide a rectifying effect on the fluid flow in which case the flow out the second orifice varies between zero velocity and a positive velocity. In the author's opinion, this effect could be enhanced by using orifices different than the straight ones used for this work. Predicting when the rectifying effect occurs is not straightforward. However, another major advantage of the double orifice geometry is that a larger first orifice increases the system Helmholtz natural frequency. This, in turn, will allow better drop control and/or faster allowable drop ejection rates.

One of the major problems during the research was the broad scope of the study. However, this wide focus did allow the identification of many interesting fundamental problems. In addition, several problems of interest to the ink-jet community were identified.

The experimentally measured values of resistance and reactance for an orifice with a surface tension boundary condition would be a valuable contribution. Another topic of interest is a piston driven Helmholtz resonator with a side branch. Such a fundamental study could provide information very useful for the design of an ink-jet printhead refill system. Another interesting project would be to build and test ink-jet printheads designed using the Chapter 2 information and compare measured performance with the analytical estimates. An experimental verification of Eq. (54) of Chapter 2 for the piston driven Helmholtz resonator subjected to a nonmonochromatic input signal would make an interesting study.

There are several studies related to oscillating flow through a single orifice which would be of interest. An experimental and analytical study of the fluid dynamics in the orifice near field would be interesting. A systematic study (i.e., using experimental design techniques of [45]) of resistance and reactance would make a good contribution to the literature.

The hot wire anemometer calibration study provided many ideas for future projects. A more detailed study of the calibration is certainly in order. A fundamental study to determine a time dependent Nusselt number for oscillating flow over a heated wire would be of interest.

The double orifice study also provided ideas for additional research. First on the list is a systematic study of the double orifice geometry with a closed outer boundary. Another idea is a study of the influence of the orifice shape on the rectifying effect of the double orifice nozzle.

Bibliography

1. Heintz1, J., and Hertz, C.H., "Ink-Jet Printing," Advances in Electronics and Electron Physics, 65, ed. P.W. Hawkes, Academic Press, New York, 1985, 91-171.
2. Larsson, S., and Lundqvist, "Studies of the Piezoelectric Capillary Injection," Research Report #10, Division of Computer Research, Chalmers University of Technology, Goteborg, Sweden, 1973.
3. Beasley, J.D., "Model for Fluid Ejection and Refill in an Impulse Drive Jet," Photogr. Sci. Engr., 21, 1977, 78-82.
4. Kyser, E.L., Collings, L.F., and Herbert N., "Design of an Impulse Ink-Jet," J. Appl. Photogr. Eng., 7, 1981, 73-79.
5. Bogy, D.B., and Talke, F.E., "Experimental and Theoretical Study of Wave Propagation Phenomena in Drop-on- Demand Ink Jet Devices," IBM J. Res. Dev., 28 (3), 1984, 314-321.
6. Mizuno, T., Satoh, T., and Tadahi, M., "Analysis of a Drop-On-Demand Ink-Jet," Soc. Inf. Disp. 1982 Digest, 1982, 150-151.
7. Roy, J., Adams, R.L., and Anderson, J., "Pressure Generation in Drop-on-Demand Ink Jets," Soc. Inf. Disp. 1985 Digest, 1985, 314-317.
8. Adams, R.L., and Roy, J., "A One-Dimensional Numerical Model of a Drop-On-Demand Ink Jet," J. App. Mechs., 53 (1), 1986, 193-197.
9. Fromm, J.E., "Numerical Calculation of the Fluid Dynamics of Drop-On-Demand Jets," IBM J. Res. Dev., 28, 1984, 322-333.
10. Panton, R.L., and Goldman, A.L., "Correlation of Nonlinear Orifice Impedance," J. Acoust. Soc. Am., 60 (6), 1976, 1390-1396.
11. Tempkins, S., Elements of Acoustics, Wiley, New York, 1981.
12. Morse, P.M., and Ingard, K.U., Theoretical Acoustics, McGraw Hill, New York, 1968.
13. Ross, D.R., Mechanics of Underwater Noise, Pergamon Press, New York, 1976.
14. Wylie, E.B., and Streeter, V.L., Fluid Transients, McGraw Hill, New York, 1978.
15. Stinson, M.R., and Shaw, E.A.G., "Acoustic Impedance of Small Circular Orifices in Thin Plates," J. Acoust. Soc. Am., 77 (6), 1985, 2039-2042.

16. Ingard U., and Ising H., "Acoustic Nonlinearity of an Orifice," J. Acoust. Soc. Am., 42 (1), 1967, 6-17.
17. Hersh A.S., and Rogers, T., "Fluid Mechanical Model of the Acoustic Impedance of Small Orifices," NASA-CR-2682, May, 1976.
18. Thurston, G.B., Hargrove, L.E., and Cook, B.D., "Nonlinear Properties of Circular Orifices," J. Acoust. Soc. Am., 29 (9), 1957, 992-1001.
19. Crandall, I.B., Theory of Vibrating Systems and Sound, Van Nostrand, New York, 1926.
20. Lord Rayleigh, The Theory of Sound, Vol. II, Dover, New York, 1945.
21. Thurston, G.B., and Martin, J.K., "End Corrections for a Concentric Circular Orifice in a Circular Tube," J. Acoust. Soc. Am., 25 (5), 1953, 861-863.
22. Tijdeman, H., "On the Propagation of Sound Waves in Cylindrical Tubes," J. Sound Vib., 39 (1), 1975, 1-33.
23. Craig, R.R., Structural Dynamics, Wiley, New York, 1981.
24. Perry, A.E., and Morrison, G.L., "Static and Dynamic Calibrations of Constant Temperature Hot-Wire Systems," J. Fluid Mech., 47 (4), 1971, 765-777.
25. Kirchoff, R.H., and Safarik, R.R., "Turbulence Calibration of a Hot Wire Anemometer," AIAA J., 12 (5), 1974, 710-711.
26. Bremhorst, K., and Gilmore, D.B., "Comparison of Dynamic and Static Hot Wire Anemometer Calibrations for Velocity Perturbation Measurements," J. Phys E: Sci. Instrum., 9, 1976, 1097-1100.
27. Bruun, H.H., "A Note on Static and Dynamic Calibration of Constant-Temperature Hot-Wire Probes," J. Fluid Mech., 76 (1), 1976, 145-155.
28. Panton, R.L., and Goldman, A.L., "Correlation of Nonlinear Orifice Impedance," J. Acoust. Soc. Am., 60 (6), 1976, 1390-1396.
29. Tijdeman, H., "On the Propagation of Sound Waves in Cylindrical Tubes," J. Sound Vib., 39 (1), 1975, 1-33.
30. Freymuth, P., "Feedback Control Theory for Constant-Temperature Hot-Wire Anemometers," Rev. Sci. Instrum., 38 (5), 1967, 677-681.

31. Freymuth, P., "Nonlinear Control Theory for Constant-Temperature Hot-Wire Anemometers," Rev. Sci. Instrum., 40 (2), 1969, 258-262.
32. Mabuchi, I., and Tanaka, T., "Experimental Study on Effect of Vibration on Natural Convection Heat Transfer From a Horizontal Fine Wire," Bull. Jap. Soc. Mech. Engr., X (41), 1967, 808-816.
33. Thrasher, B.H., and Schaetzle, W.J., "Instantaneous Measurement of Heat Transfer From an Oscillating Wire in Free Convection," J. Ht. Trans.: ASME Series C, 92, 1970, 439-446.
34. Carr, W.W., and Black, W.Z., "Interferometric Measurement of Instantaneous Local Heat Transfer From a Horizontally Vibrating Isothermal Cylinder," Int. J. Heat Mass Transfer, 17, 1974, 633-642.
35. Stemme, E., and Larsson, S.G., "The Piezoelectric Capillary Injector-A New Hydrodynamic Method for Dot Pattern Generation," I.E.E.E Trans. Electron Devices, ED-20, (1), 1973.
36. Stinson, M.R., and Shaw, E.A.G., "Acoustic Impedance of Small Circular Orifices in Thin Plates," J. Acoust. Soc. Am., 77 (6), 1985, 2039-2042.
37. Panton, R.L., and Goldman, A.L., "Measurement of the Acoustic Impedance of an Orifice under a Turbulent Boundary Layer," J. Acoust. Soc. Am., 60 (6), 1976, 1397-1404.
38. Ingard U., and Ising H., "Acoustic Nonlinearity of an Orifice," J. Acoust. Soc. Am., 42 (1), 1967, 6-17.
39. Thurston, G.B., "Apparatus for Absolute Measurement of Analogous Impedance of Acoustic Elements," J. Acoust. Soc. Am., 24 (6), 1952, 649-652.
40. Thurston, G.B., Hargrove, L.E., and Cook, B.D., "Nonlinear Properties of Circular Orifices," J. Acoust. Soc. Am., 29 (9), 1957, 992-1001.
41. Ingard, U., and Labate, S., "Acoustic Circulation Effects and the Nonlinear Impedance of Orifices," J. Acoust. Soc. Am., 22 (2), 1950, 211-218.
42. Bolt, R.H., Labate, S., and Ingard, U., "The Acoustic Reactance of Small Circular Orifices," J. Acoust. Soc. Am., 21 (2), 1949, 94-97.
43. Sivian, L.J., "Acoustic Impedances of Small Orifices," J. Acoust. Soc. Am., 7, 1935, 94-101.
44. Tempkins, S., Elements of Acoustics, Wiley, New York, 1981.

45. Diamond, W.J., Practical Experiment Designs, Lifetime Learning Publications, Belmont, California, 1981.
46. Stemme, N.G.E., "Arrangement of Writing Mechanism for Writing on Paper With a Colored Liquid," U.S. Patent 3,747,120, 1973.
47. Miura, M., Yamamori, K., and Mizoguchi, A., "Apparatus for Applying Liquid Droplets to a Surface by Using High Speed Air to Accelerate the Same," U.S. Patent 4,106,032, 1978.
48. Bischel, D., Gilbert, J., and Lilly, J., "Flow Visualization in an Ink-Jet Printhead," Oregon State University Senior Project Report, March 1986.

APPENDIX

APPENDIX A. FLOW VISUALIZATION STUDY

A summary of the flow visualization study conducted as a senior project by Bischel, Gilbert, and Lilly [48] is presented in this appendix. Their objective was to obtain photographs of the streamlines formed between the two plates shown in Fig. A.1 as fluid oscillated through the two orifices. Smoke marked streamlines were produced by vaporizing mineral oil on a heated wire which was passed through the center of the orifice.

Dimensional analysis of the problem showed that the fluid mechanics are governed by four dimensionless parameters and photographs were taken to span the following ranges: $0.23 < v_o/\omega t_p < 1.00$, $1 < t_p/d_1 < 2$, $0.39 < d_2/d_1 < 0.63$ and $100 < v_o t_p/\nu < 200$; where length scales are defined on Fig. A.1, v_o is the magnitude of the oscillating velocity incident on the first orifice, ω is frequency in rad/s, and ν is kinematic viscosity.

Using a wire as a source of smoke will only allow visualization of the streamlines perpendicular to the wire. Thus, it was only possible to see the streamlines moving radially from the center line of the orifices. A typical streamline pattern is sketched in Fig. A.2 and two typical photographs are shown in Fig. A.3. In the photographs, the wire appears as a bright vertical light streak and the two light streaks in Fig. A.4a mark the edges of the lower orifice.

Eight photographs were taken to span the range of independent variables. An experiment design following Diamond [45] was used to set up the experiment in order to maximize the amount of useful information from the data. In all cases, vortices formed and their dimensions were correlated with the independent variables. These quantitative results will not be reviewed here except to mention that the vortex characteristic dimensions did not depend on the Reynold's number, $Re = v_o t_p/\nu$. This result is useful in supporting the experiment design presented in Chapter 4 in which the influence of Re was assumed to be negligible.

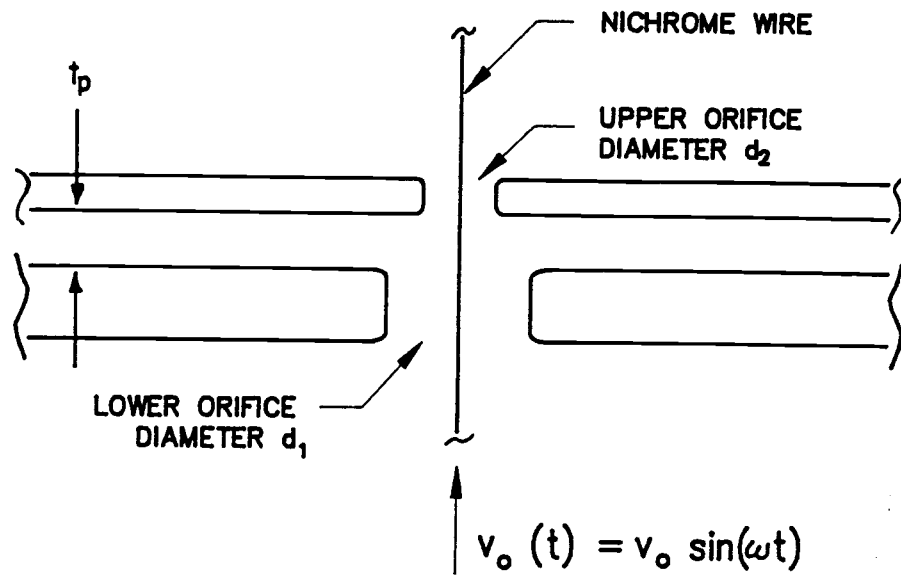


Fig. A.1. Flow visualization geometry

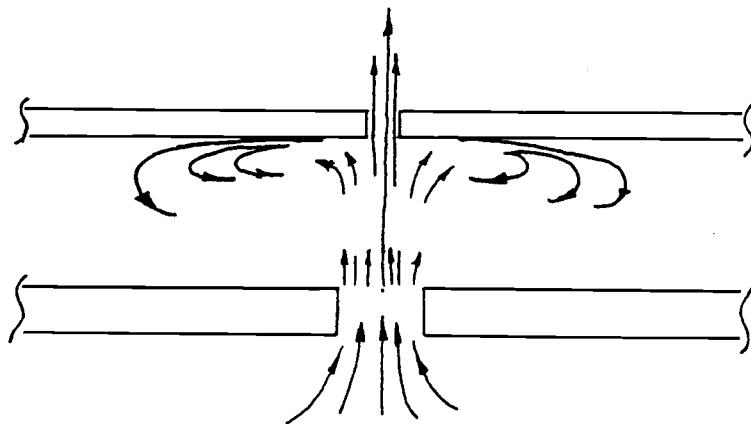
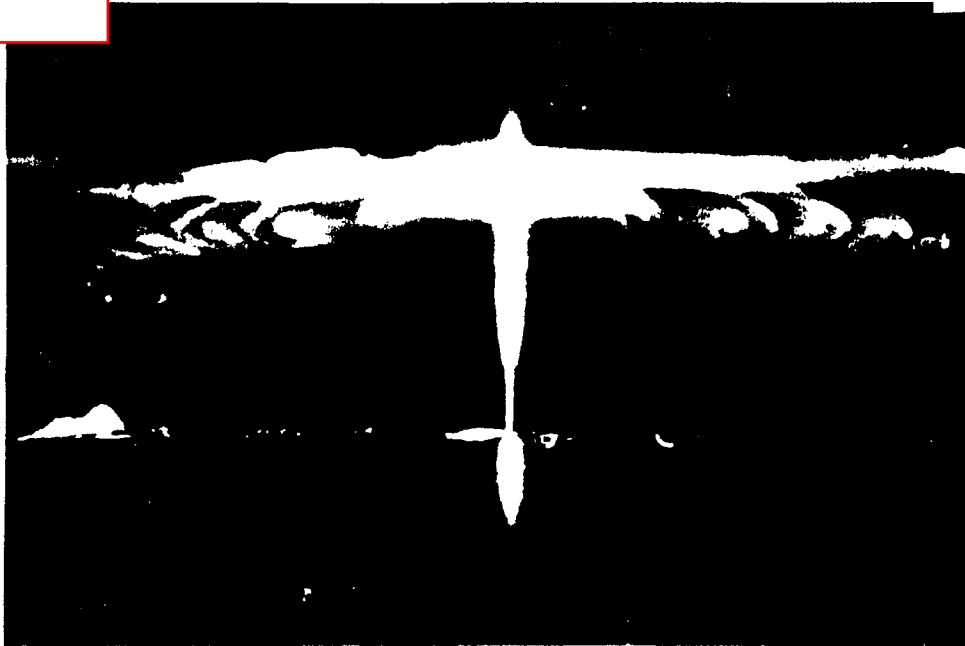


Fig. A.2. Sketch of typical streamlines during fluid outflow portion of cycle

Best scan available. Original is black and white photocopy.

(a)



(b)

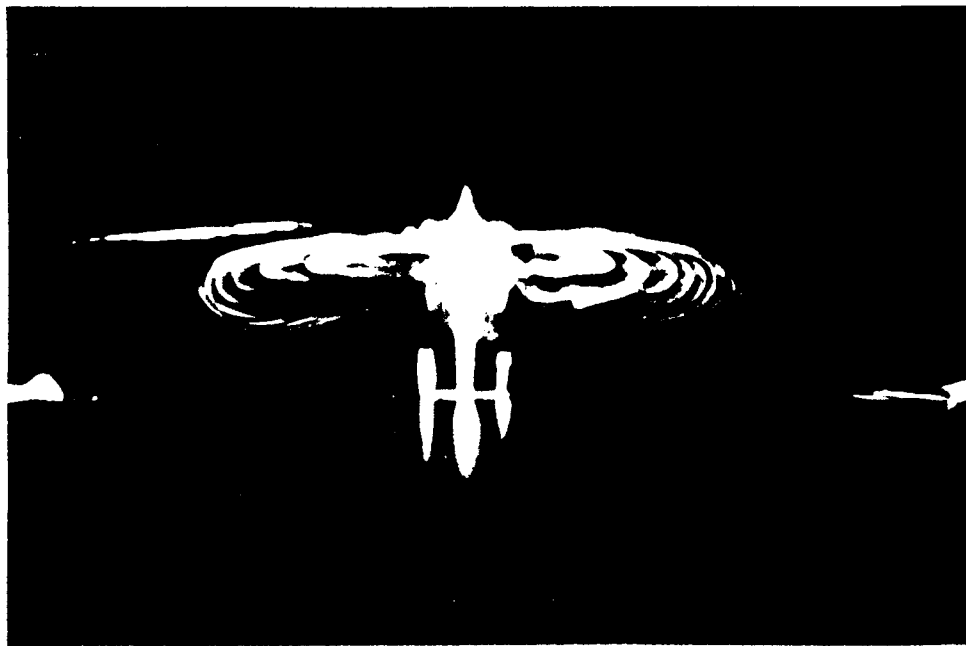


Fig. A.3. Typical streamline photographs

(a) $v_o/\omega t_p = 0.23$, $t_p/d_1 = 2$, $d_2/d_1 = 0.39$, $v_o t_p/\nu = 200$

(b) $v_o/\omega t_p = 0.23$, $t_p/d_1 = 2$, $d_2/d_1 = 0.63$, $v_o t_p/\nu = 100$